Hyaluronic Acid-Based Materials for Biomedical Applications

ZIYU GAO

Submitted in accordance with the requirements for the degree of

Doctor of Philosophy

The University of Leeds

School of Chemistry

School of Dentistry

September, 2020

The candidate confirms that the work submitted is her own and that appropriate credit has been given where reference has been made to the work of others.

Acknowledgements

This project was original studied by Ziyu Gao, however, with great assistance from many other researchers.

Firstly, I want to express my appreciation to my supervisor Dr Paul Thornton, whose knowledge, kindness and patience have been accompanying me throughout this project no matter in work or life. His professional suggestions in chemistry strongly supported me in this research and his great help in improving my English language were appreciated.

I am grateful for the special help from Dr Giuseppe Tronci, who joined my PhD as co-supervisor lately and provided enormous help in translating this project from chemistry into tissue engineering. His knowledge in biomaterials science and tissue engineering extended the potential of this research and also extended my research interests.

As a team, Paul and Giuseppe helped me build up a systematic route from mechanism study to clinical application, many thanks for their supervision that made this multidisciplinary project a success.

Thanks to Dr Xuebin Yang, who provided professional suggestions in cell experiments and biomedical discussion.

Thanks to Dr Patrick McGowan for his critical review of the inorganic chemistry featured, and to Dr Christopher Pask and Dr Pablo Carames-mendez for their effort in inorganic analysis.

Thanks to Dong Xia, Layla Hassouneh, Benjamin Golland and Xiaolong Ma for their kind help in material measurement and discussion.

Thanks to Dr Paul A. Bingham and Dr Alex Scrimshire for enabling access to Mössbauer spectroscopy analysis and the detailed discussion concerning the possible inorganic structures produced.

Thanks to Dr Elena Jones for collecting and providing clinical patients samples. Thanks to Sarah Myers for her great assistance in laboratory training and her caring help in both work and life.

Thanks to Dr Juan Pang and Dr Xiaohong Hu for their assistance in computational modelling and polymer material discussion.

Finally, in life, thanks my parents and my special friend Qiao Sen, who strongly supported me spiritually and financially during my PhD study. Thanks all my friends for sharing my anger and pleasure, my tears and smiles, my failure and success, witnessing my growth.

Thanks for all your company.

Abstract

The vital biological functions of hyaluronic acid *in vivo* has resulted in extensive investigation into its biomedical application. This thesis reports the biomedical applications of a range of innovative hyaluronic acid-based hydrogels, from material design and creation optimisation to relevant application. A comprehensive review of recent and ongoing research concerning hyaluronic acid-based hydrogels and their deployment within biomaterial research is presented. The research conducted features four subjects; (1) the synthesis, characterisation, and application of a redox-responsive hyaluronic acid-based hydrogel for chronic wound management, (2) hydrogen phosphate-mediated acellular biomineralisation within a dual crosslinked hyaluronic acid hydrogel,. (3) the facile and additive-free synthesis of a cell-friendly Iron(III)-Glutathione Complex that enhanced L929 cell growth after 7 days and reduced matrix metalloproteinase-13 activity, demonstrating promising application in osteoarthritis treatment, (4) An injectable, self-healing and MMP-inhibiting hyaluronic acid gel formed via crosslinking with the aforementioned iron-glutathione complex. The original materials reported provide the basis for the development of numerous HA-based hydrogels that have potential significance in a range of biomedical fields including the assessment of glutathione levels in chronic wounds and cancer tissue, scaffolds for tissue regeneration, and therapy for osteoarthritis treatment.

Table of Contents

List of Tables

List of Figure

Abbreviations

AAc	Acrylic acid
AFM	Atomic force microscopy
AMPA	p-aminophenyl mercuric acetate
ATR-FTIR	Attenuated total reflectance fourier transform infrared spectroscopy
ALP	Alkaline phosphate
C2-20	Hyaluronic acid hydrogel crosslinked by 20 mol.% of cystamine (added in)
C2-40	Hyaluronic acid hydrogel crosslinked by 40 mol.% of cystamine (added in)
c-SBF	Conventional simulated body fluid
Cys	Cysteine
CD	Circular dichroism spectroscopy
DMTMM	4-(4,6-dimethoxy-1,3,5-triazin-2-yl)-4-methyl-morpholinium chloride
DMEM	Dulbecco’s modified Eagle’s medium
DFT	Density functional theory
DSC	Differential scanning calorimetry
DLS	Dynamic light scattering
E2-40	Hyaluronic acid hydrogel crosslinked by 40 mol.% of ethylenediamine (added in)

ECM	Extracellular matrix
ESI-MS	Electrospray ionisation mass spectrometry
FBS	Fetal bovine serum
FS	UV-Vis fluorescence spectroscopy
Fe^{3+}-GSH	Iron(III)-Glutathione complex
FWHM	Full width at half maximum
GSH	Glutathione reduced
GSSG	Glutathione oxidised
HA	Hyaluronic acid
HAp	Hydroxyapatite
^{1}H NMR	Proton nuclear magnetic resonance spectroscopy
µCT	X-ray computed microtomography
MES	2-(N-morpholino) ethanesulfonic acid
MMP	Matrix metalloproteinase
MSC	Mesenchymal stem cell
NTCPs	Non-treated tissue culture plates
OA	Osteoarthritis
PBS	Phosphate buffer saline
RT-PCR	Real-time polymerase chain reaction
PAAc	Poly(acrylic acid)
PDGF	Platelet-derived growth factor

PDI	Square of light scattering polydispersity
PEG	Poly(ethylene glycol)
PNIPAm	poly(N-isopropylacrylamide)
Poly(VPI^{+}PTZ-$(CH_2)_3SO^{3-}$)	Poly(1-vinyl-3-propionate imidazole phenothiazine sulfonic acid)
PS	Penicillin–streptomycin
RGD	Arginylglycylaspartic acid
RITC-dextran	Rhodamine B isothiocyanate-dextran
SAXS	Small-angle X-ray scattering
SR	Swelling ratio
SEM	Scanning electron microscopy
SBF	Simulated body fluid
SF	Synovial fluid
SWF	Simulated wound fluid
TCPs	Tissue culture plates
TGA	Thermogravimetric analysis
3D	3-dimensional
TNBS	2,4,6-trinitrobenzenesulfonic acid
VAS	Visual Analog Scale
VEGF	Vascular endothelial growth factor
VSM	Vibrating-sample magnetometer

WOMAC	Western Ontario and McMaster Universities Osteoarthritis Index
XRD	X-Ray powder diffraction
XPS	X-ray photoelectron spectroscopy

Chapter 1

Review on recent study of hydrogels for biomaterials

1.1 Introduction to hydrogels

1.1.1 Polymer-based hydrogels

Hydrogels may be described as constant water-swollen three-dimensional networks formed from the crosslinking of (macro)molecules. They were first synthesised as “hydrophilic gels” based on glycolmethacrylate in 1960. Co-polymers of glycolmonomothacrylate with several tenths of glycoldimethacrylate were found to be the most suitable material in their work for permanent contact with living tissues as the adjustable mechanical properties, water content and transparency.(1) The crosslinks may be formed by physical or chemical interactions between hydrophilic polymers to form a structure that displays properties characteristic of both solids and liquids.(1-2) Like solids, hydrogels deform with stress and are able to recover their initial shape within a certain stress range. Like liquids, hydrogels can support fluid convection and diffusion of solutes that are smaller than the mesh size of the network**.** For example, hyaluronic acid (HA) hydrogels (Figure 1.1) that contained over 95 wt.% water formed a stable structure, which will be discussed later. Commonly, hydrogels are prepared using hydrophilic polymers that form a crosslinked network. The significant absorption of a large amount of water enables the hydrogel formed to maintain its shape and mechanical properties, enabling hydrogels to be employed within a wide range of applications including biomedicine,(3–7) cleaning materials(8-11) and antimicrobial materials(12) in living environments, and water restoration materials in agriculture.(13-14) There are two categories of hydrogels based on the crosslinking methods; chemical and physical hydrogels.

Figure 1.1 Example of a cystamine crosslinked HA hydrogel, presented after rhodamine staining.

1.1.1.1 Chemical hydrogels

Chemical hydrogels contain polymer chains that are connected through simple covalent crosslinking that allows hydrogels to hold a particular shape.(15-16) There are three kinds of basic reactions to construct the scaffolds used to form chemical hydrogels, polymerisation, polymer crosslinking and the modification of macromolecules by conducting polymerisations from pendant functional groups to yield graft copolymers.

1.1.1.1.1 Polymerisation

Chemical hydrogels may be produced from polymers created from unsaturated monomers by free radical homopolymerisation or copolymerisation. Examples of monomers that have been used to create chemical hydrogels include but not limited to 2-hydroxyethyl methacrylate (HEMA)(17-18), acrylamide (AM)(17), methacrylic acid (MAA)(18). An example of a relevant polymerisation is provided in Figure 1.2. The hydrogel properties can be adjusted easily through changing monomer ratios, for instance increasing the amount of AM relative to HEMA enables the formation of a material with higher swelling ratio and better stretchability.(17) Not limited to this, changing the initiator, or including chelation agents and/or chain transfer agents during the polymerisation may be conducted

to control the polymerisation kinetics, and alter the properties of the subsequent hydrogel, which provides potential for material design and is worth further study.

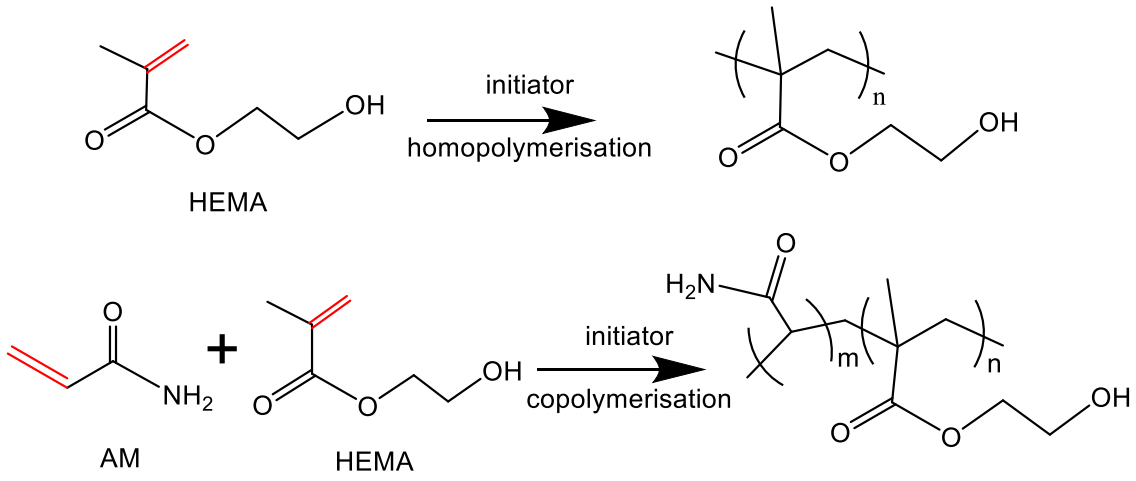

Figure 1.2 Schematic of homopolymerisation (top) and copolymerisation (below).

(17)

1.1.1.1.2 Polymer crosslinking

Chemical hydrogels have been synthesised from crosslinked macromolecules, including natural-based (chitosan CS,(19-20) alginate,(20) hyaluronic acid,(21) gelatin(22)) and synthetic macromolecules, for example, poly(ethylene glycol) (PEG) (23). To form chemical hydrogels, the polymers must possess activating groups that can undergo crosslinking to yield a stable network (Figure 1.3). Often reported as being appropriate biomaterials, the active groups (such as carboxylate groups, amine groups, and thiol groups) in these polymers can be functionalised with bioactive substances such as albumin,(24) neurotrophic factors(25) and aptamer (single-stranded oligonucleotides selected from synthetic RNA/DNA libraries)(26) that render them suitable for implant materials

that can induce Schwann cell proliferation and migration, and peripheral nerve regeneration, controllably release angiogenic growth factors .(24-26)

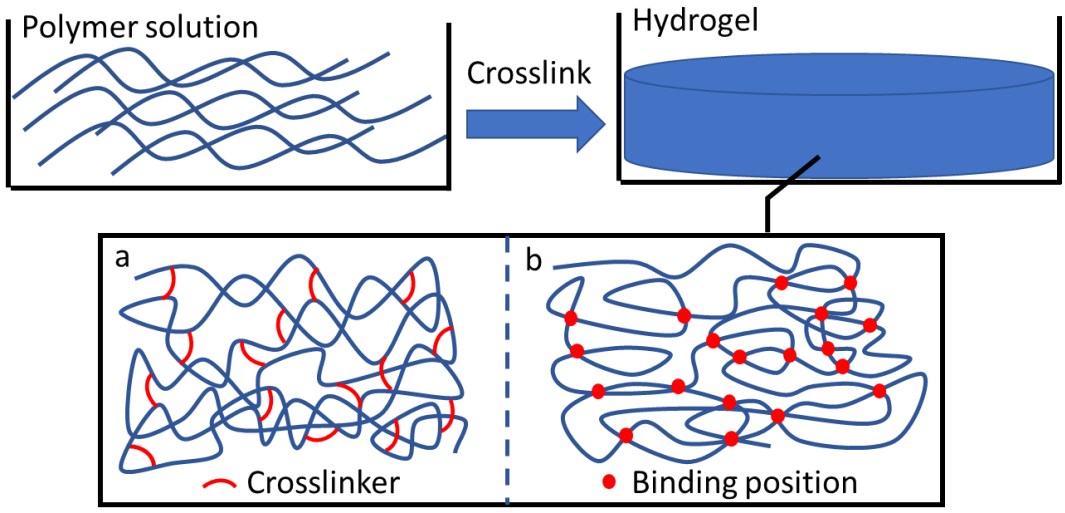

Figure 1.3 Polymer crosslinking progress. Hydrogel formation through crosslinkers (a) and polymer self-crosslinking at native binding positions (b).

1.1.1.1.3 Polymerisation from modified macromolecules

A synthetic strategy is to use unsaturated bonds on the side or main chain of the macromolecule matrix in polymerisation. These modified macromolecules can be polymerised through covalent bonds with controllable hydrogel elasticity, water absorption, pH response, degradability and thermal sensitivity.(27-28) For example, acrylamide (AA) was modified onto starch melt molecule chain via extrusion method and obtained starch-AA copolymer gel with a significant enhancement in storage modulus after polymerisation under the initiation of ammonium sulfate in nitrogen environment.(29) Zhang *et al.* reported a novel zwitterionic hydrogel through adding a mixture of vinylsulfonic acid (VSA, as the negatively charged monomer) and [2-(methacryloyloxy)ethyl]trimethylammonium chloride (METMAC, as the positively charged monomer) onto the surface of polyethersulfone membrane. VSA and METMAC were crosslinked by N,N'-methylenebisacrylamide under UV irradiation to obtain the polyampholyte

hydrogel surface.(30) This zwitterionic hydrogel presented interesting anti-fouling properties in bovine serum albumin, humic acid, and sodium alginate models under static adsorption.

1.1.1.2 Physical hydrogels

Physical hydrogels are created by non-covalent interactions between polymer chains. Such interactions include ionic interactions, hydrogen bonds and hydrophobic interactions, and provide a way to obtain stable hydrogels without any potentially toxic additions, or post-polymerisation modification to form covalent crosslinks.(31-35)

1.1.1.2.1 Ionic interactions

Physical hydrogels may be formed by electrostatic interactions between opposite charges, such as strong ionic coordination bonds between Fe^{3+} and COO^{-} groups present on a polymer. Such interactions enhanced the mechanical properties of polyacrylamide/cellulose nanofibers (CNF, contain COO^{-} groups) composite hydrogels that were obtained through dual crosslinking that included Fe^{3+} and COO^{-} physical coordination and hydrogen bonds between polyacrylamide and cellulose with excellent strength and stretchability (Figure 1.4) in 2018.(31)

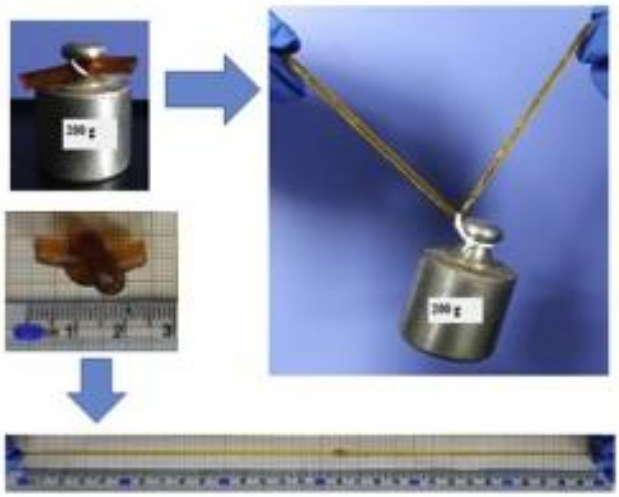

Figure 1.4 A visual image of CNF2.0-Fe^{3+}1.5 hydrogel (2 wt.% of CNF refers to the polyacrylamide content and immersed in Fe^{3+} solution with a concentration of 1.5 M) exhibiting excellent strength and stretchability.(31)

Yuan *et al*. obtained chitosan-based hydrogels based on negatively charged poly(acrylic acid) (PAAc) and positively charged 2-hydroxypropyltrimethyl ammonium chloride chitosan (HACC) in the presence of NaCl (Figure 1.5). Due to ionic interactions, the hydrogel (PAAc/HACC) presented a high tensile fracture stress (3.31 MPa) and Young's modulus (2.53 MPa),(32)

Figure 1.5 Schematic representation of the preparation method and network structure of the PAAc/HACC hydrogel.(32)

1.1.1.2.2 Hydrogen bond interactions

In polymer-aqueous solutions, intra- or inter-molecular hydrogen bonds between polymer chains can provide physical binding sites for polymer crosslinking. Acceptor atoms possess pronounced electronegativity and form hydrogen bonds with hydrogen atoms on adjacent polymer chains. For example, macromolecules that contain an ether bond (C-O-C) and hydroxyl groups (-OH) may form crosslinks with other water-soluble polymers that possess carboxyl (-COOH) and hydroxyl (-OH) groups due to the hydrogen bonds formed between oxygen and hydrogen.

A facile ion-exchange reaction was reported to fabricate poly(ionic liquid) (poly(1-vinyl-3-propionate imidazole phenothiazine sulfonic acid, abbreviated as poly($VPI^{+}PTZ$-$(CH_2)_3SO_3^{-}$). It was then successfully introduced in hydrogel preparation with chitosan molecules through hydrogen bonds interaction between carboxyl groups in poly($VPI^{+}PTZ$-$(CH_2)_3SO_3^{-}$) and protonated amino groups in chitosan.(33) The gelation time was within 5 minutes and a material for maintaining and stabilising enzyme activity was obtained after electrochemical testing.

Ye *et al.* reported several novel self-healing, pH-sensitive, and biodegradable hydrogels based on cytosine and guanosine-modified HA via hydrogen bond formation between guanosine and cytosine (Figure 1.6) in 2017.(34) A high strength (up to 3.71 MPa) hydrogel containing poly(vinyl alcohol) (PVA) and hydroxyapatite, formed through inter- and intra-molecular hydrogen bonds (hydroxyl groups of PVA and hydroxyl groups on hydroxyapatite) and annealing treatment was prepared by Chen *et al*. This material displayed low friction with a friction coefficient from 0.06-0.18 under 10-20 N load, which provided potential application in soft tissue and cartilage replacement.(35)

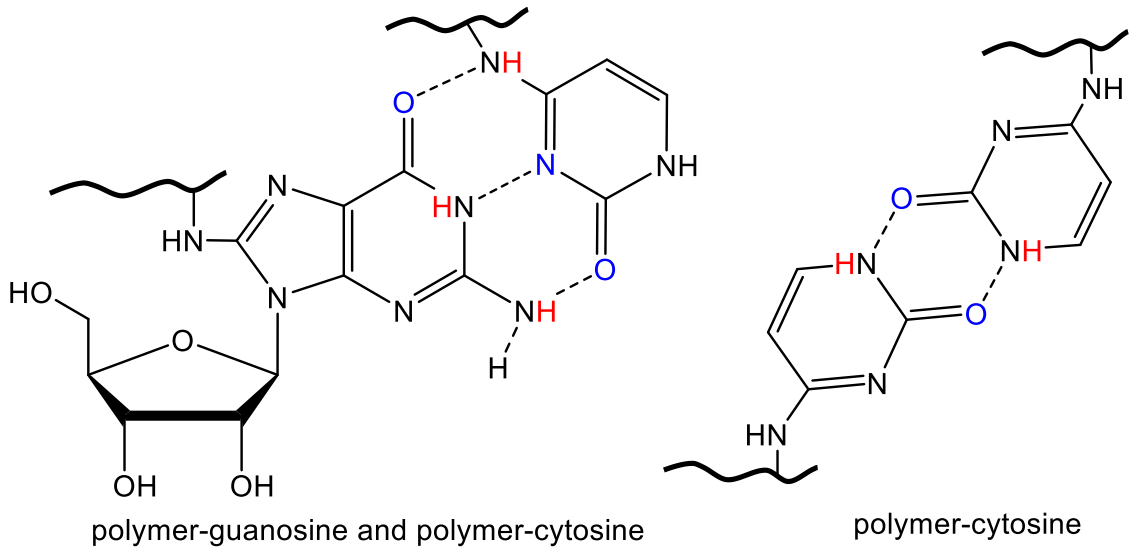

Figure 1.6 Illustration of hydrogen bond interactions between polymer-guanosine and polymer-cytosine.(34)

1.1.1.2.3 Hydrophobic Interactions

Hydrophobic monomers can be modified by surfactant molecules through chemical binding. During the polymerisation of hydrophilic monomers, surfactant-modified hydrophobic monomers can aid micelle formation, even at low concentrations in the reaction system when copolymerised with a hydrophilic majority. The micelles then twine with the hydrophilic polymer chains and form into hydrogel. In 2018, Owusu-Nkwantabisah prepared a thermal stiffening hydrogel through hydrophobic association based on a copolymer of benzyl methacrylate (diluent), stearyl methacrylate (hydrophobic), and methacrylic acid (hydrophilic), and obtained a 100-fold increase in modulus with an increase of 25 °C in temperature. The thermal stiffening mechanism of this hydrogel was proposed as the polymer chain conformational changes with increasing temperature facilitated the inter-chain associations.(36) By incorporating hydrophobic interactions, Deng *et al.* presented a new method to fabricate a mechanically-reinforced hydrogel based on PEG of various molecular weights that was present in the ring-opening polymerisation of ε-caprolactone. The

resulting hydrogels possessed self-healable and conductive properties upon inclusion of Fe^{3+}.(37) Very recent research has reported a dual-crosslinked self-healing hydrogel system formed by polyacrylamide/lauryl methacrylate hydrophobic interactions as the first network and Fe^{3+}/poly(acrylic acid) ion association structure as the second network.(38) The dual-network design provided this physical crosslinked hydrogel adjustable mechanical properties in tension, compression, bending and torsion with retained self-healing property.(38)

1.1.2 Functional Hydrogels

Stimuli-responsive hydrogels may undergo volume changes, gel-sol transitions, and changes in mechanical behaviour in response to the presence of environmental stimuli. These “smart” hydrogels with controllable/reversible properties can be applied as drug delivery systems, artificial tissue scaffolds, biosensing devices and for cell manipulation.(39) In recent years, reversible covalent bonds have been reported to promote hydrogel assembly/disassembly based on cycloadditions(40-41), electrostatic interactions(42-43), redox reactions(44-46), and acylhydrazone bond formation/cleavage(47-48). These dynamic bonds allow the hydrogel to turn into a weaker, or stronger, network structure in the presence of the target stimulus.

1.1.2.1 pH-Sensitive Hydrogels

For biomaterials, hydrogels are expected to be applied in a highly complex environment *in vivo*. Many diseases may cause a local environmental pH change, including within a cell’s inner microenvironment. Gao *et al.* realised pH-controllable drug release from xylan-based hydrogels to significantly different extents dependent on environmental pH which were simulated to between pH 1.5

and pH 7.4. Accumulative drug release (%) was observed to be 26% and 90%, respectively, after 8 hours continuous release.(49) A 19–40% reduction in chitosan-based hydrogels' volume occurred when maintained in solution of pH 3 compared to when maintained in solution of pH 9, as reported by Zhu *et al*. The amino groups (pKa 6.5) of chitosan are protonated at low solution pH, and so their interaction with water molecules increases when the hydrogel is stored in low pH solution.(50) Not limited to physical change, this kind of pH-responsive behaviour can be further optimised through combining two different pH-sensitive polymers, such as N,O-carboxymethyl chitosan and alginate, to realise pH-sensitive swelling ratios via adjusting the component ratio and to be used as a controllable drug delivery system.(51)

Environmental pH may also be used to stabilise hydrogels' physical appearance and can be exploited to optimise their size, shape, mechanical properties and degradability as a final step in material processing. For example, creating 3D printing hydrogel materials to smaller volumes, which was successfully demonstrated in a system of hyaluronic acid combined with either alginate, gelatin or chitosan in solutions of pH =1 or pH=4.7.(52) However, the generation of a highly sensitive hydrogels that can respond to small changes in solution pH remains a key biomedical challenge, since only a very weak solution pH change may be brought by abnormalities in pathology.

1.1.2.2 Temperature-Sensitive Hydrogels

Temperature-sensitive hydrogels can form upon a heat-induced reversible sol-to-gel transition. For biomedical applications, the transition temperature is usually low to normal body temperature, from 33 °C (skin) to normal physiological temperature 37.5 °C.(53) High sensitivity is required since the presence of disease may result in a slight increase or decrease in body temperature, even in

thermal therapy, as the body becomes damaged at temperatures above 44 °C.(54)

Chen *et al*. disclosed a hydrogel that underwent temperature-driven sol-to-gel transition at mild temperatures (from 27.8 to 30.3 °C, depending on the components) composed of chitosan, HA and Poly(N-isopropylacrylamide).(55) In 2015, Montero-Rama *et al.* prepared hydrogels via the copolymerisation of 2-(2-methoxyethoxy)ethyl methacrylate (MEO_2MA) and 2-(acetylthio)ethyl methacrylate (AcSEMA) and N,N,N'',N''-tetramethylethylenediamine (TEMED), using ammonium persulfate (APS) as the initiator, and observed a decreased equilibrium swelling that correlated with an enhanced temperature (an approximate range from 0 °C to 35 °C at pH 7, depending on the monomer ratio) at neutral condition were reported.(56) This phenomenon was attributed to the introduction of hydrophobic monomer (AcSEMA), which brought a new hydrophobic/hydrophilic balance and also changed the hydrogel cloud point as a function of temperature.

1.1.2.3 Light-Sensitive Hydrogels

Light is an attractive stimulus to manipulate hydrogel properties due to its facile, and controllable, operation.(57-58) Photo-switchers that are reversible under a certain wavelength of light change from *trans* to *cis*, or vice versa, and have been applied in hydrogels. For example, azobenzene is known as a common photo-switcher, whose configuration can be changed through light irradiation under different wavelength; it has a *trans* configuration under visible light and *cis* configuration under UV light. Based on this isomerisation, azobenzene was grafted onto hyaluronic acid chains, combining with host-guest supramolecular chemistry as presented in Figure 1.7, to yield a photo-reversible HA hydrogel. The storage modulus of this hydrogel can be altered reversibly from

approximately 950 Pa (420 nm) to 650 Pa (365 nm) upon azobenzene configuration change.(57)

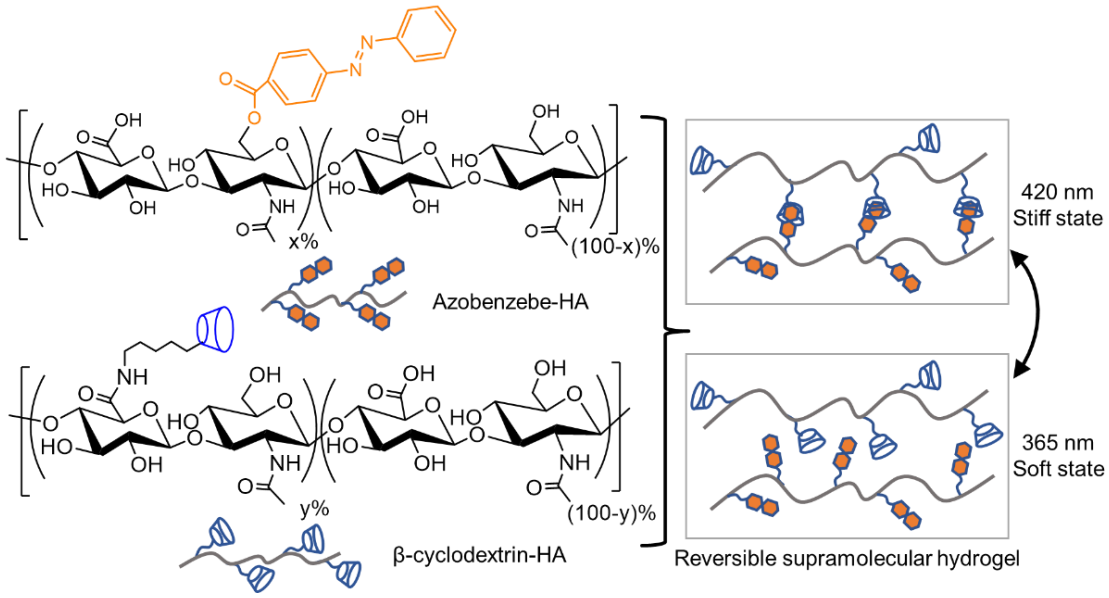

Figure 1.7 Graphic illustration of photo-reversible HA hydrogel based on azobenzene and β-cyclodextrin supramolecular interaction.(57)

1.1.2.4 Self-healing hydrogels

Self-healing hydrogels are a new class of hydrogels that are able to intrinsically and automatically heal physical damage without external stimuli. This fascinating capability promoted their value as biomaterials to mimic the automatic repairing and healing process after damage in living creatures, thus, restoring certain destroyed functions. Deng *et al*. prepared reversible self-healing hydrogels through acylhydrazone and disulfide bonds (as shown in Figure 1.8).(59) Acylhydrazone promotes self-healing in acidic or neutral conditions and disulfide bonds promote self-healing under basic conditions. However, catalytic aniline was needed to accelerate the acylhydrazone exchange reaction to achieve self-healing at neutral conditions, which may limit its further bio-application. Wang *et al*. prepared a self-healing, dual-responsive hydrogel based on alginate by Schiff base reaction with PEG. The results of strain sweep measurements after three

cycles illustrated the 100% and repeatable self-healing functionality of the material. In addition, a 12-hour self-healing time was recorded by putting two individual halves of hydrogel together and observing hydrogel repair.(60)

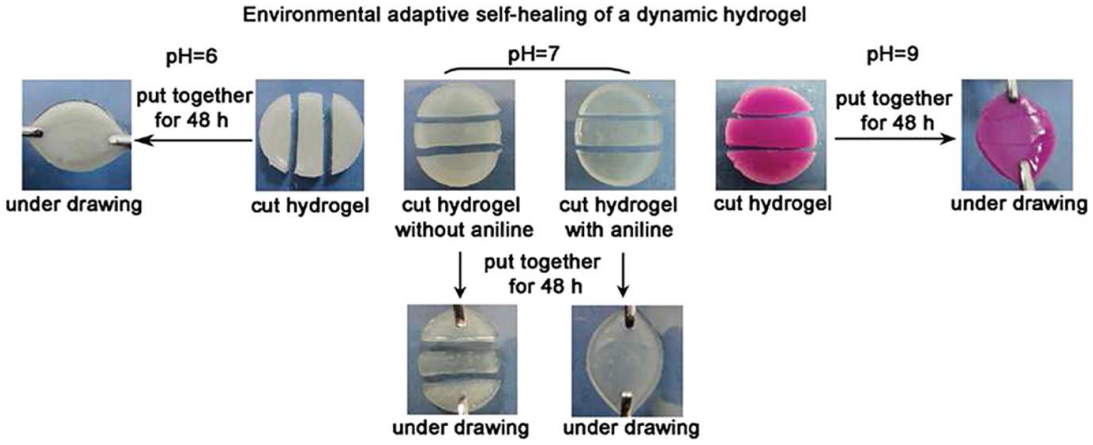

Figure 1.8 Environmental adaptive self-healing of dynamic hydrogel.(59)

1.1.2.5 Injectable hydrogels

Injectable hydrogels are suitable biomaterials, especially for tissue engineering scaffolds (61), and the healing of chronic wounds (62–64). The injectable property enables material administration and rapid hydrogel formation *in situ*, which has promising application in clinical medicine. Liu *et al.* reviewed the development of different biomaterials and the different approaches to creating injectable hydrogels for cartilage and bone tissue engineering (Figure 1.9).(65) Hyperbranched multi-acrylate PEG macromer (HP-PEGs) was reported that can form a novel injectable hydrogel *in situ* by thiol-ene click reaction for a stem cells delivery and retention platform.(66) Gel formation occurred in 96 s (2.5% w/v, HP-PEGs) and 57 s (10% w/v, HP-PEGs) *in vivo* with accelerated wound healing in rat models.

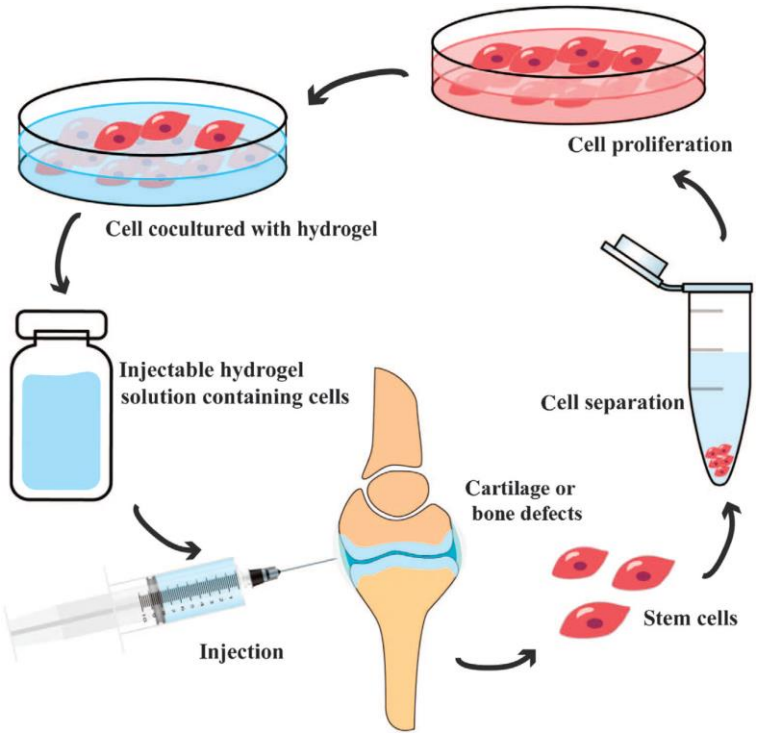

Figure 1.9 Schematic illustration of injectable hydrogel formation for cartilage- and bone tissue-engineering applications.(65)

1.1.3 Development of Hydrogels as Biomaterials

1.1.3.1 Hydrogels as Biosensors

Hydrogels can be applied as immobilising scaffolds to act as a detection/therapy template.(67-69) In 2013, Khimji *et al.* concluded the recent development of visual biosensors for DNA immobilisation based on polyacrylamide hydrogels which possess an obvious gel-sol transition at a mild temperature.(67) DNA can be included within the hydrogel through copolymerisation, as a crosslinker or physical mixing. Changes in the DNA sequence can enable the hydrogels to detect various target analytes including Hg^{2+} and viruses due to the selectivity of specific DNA binding. Particles, for instance monolayer-polystyrene particles (diameter ~600 nm), can be inserted into urease-modified 2D colloidal crystal hydrogels to obtain a label-free urease coupled biosensor for the analysis of urea and urease inhibitor.(69) An increasing urea concentration from 0-120 mM can

be observed by the naked eye with colour change from red to blue-purple. Decreased particle spacing was observed and explained as a consequence of urease-urea catalytic reaction, which produced NH_4^+ and HCO_3^-, and resulted in the hydrogel volume shrinkage.

Another popular application is developing hydrogels as bioelectronic devices. (70-71) In recent research, a new type of soft ionic-type asymmetric ionic sensing hydrogel (AISH) tactile sensors based on PAAc/Ag^0 hydrogels was developed by Liu and Zhang's groups.(71) A low external working voltage (20 mV) with ultrahigh sensitivity (171.4 kPa^{-1} at 75–1500 Pa and 57.5 kPa^{-1} at <75 Pa) and ultralow detection force (0.075 Pa) were reported, enabling ultra-sensitivity for bio-microenvironments such as vibration of the vocal cord, and use as wearable bioelectronic devices.(71)

1.1.3.2 Hydrogels for drug delivery

The 3D network structure of hydrogels can withhold small molecular drugs, as demonstrated by chitosan(72) and carrageenan(73) hydrogels, and biomacromolecules themselves can be made into therapeutic nanohydrogels to be delivered, such as collagen and hyaluronic acid, which are known as "anti-aging agents"(74).

Karimi *et al.* obtained a pH- and thermo-responsive hydrogel based on the synthesis of tris(2-(2-formylphenoxy)ethyl)amine as a novel crosslinker, and realised the controllable release of metronidazole in 2018.(75) Salicylaldehyde was chosen to modify tris(2-chloroethyl)amine, the aldehyde groups remained and then reacted with the amine groups on the chitosan backbone through Schiff-base reaction to build the hydrogel networks without the addition of reducing agents. This material allowed rapid release of metronidazole to acidic solution (pH=4), since a low pH causes the $-NH_2$ groups to become protonated,

accompanied with increased hydrogel swelling ratio. While in basic conditions, a lower release rate was observed since both protonated and deprotonated -NH_2 groups are present and the repulsion forces decreased. Drugs can also be encapsulated into hydrogel beads and be released following hydrogel bead degradation or hydrolysis. Spherical alginate micro-hydrogel beads were reported to form via Ca^{2+}/alginate coordination with encapsulated ibuprofen.(76) Four times higher swelling ratio of hydrogel beads was presented in phosphate buffered saline PBS (pH 7.4), compared with H_2O (pH 6.5-7.0) and simulated gastric acid (pH 1.2), demonstrating responsive ibuprofen release in PBS. Ibuprofen release occurred because the -COOH of alginate hydrogel beads became ionised to COO^- and Ca^{2+} began to exchange with Na^+ in PBS, resulting in the alginate hydrogel beads disassemble.(76)

1.1.3.3 Hydrogels for tissue engineering

1.1.3.3.1 Tissue replacement

Hydrogels maintain their shape in water for prolonged periods, which enables their potential use as scaffolds for tissue engineering. However, high strength and adjustable degradability are often required for such materials. A double-network (DN) structure in which polymers were crosslinked by two different crosslinking/binding sites was developed that can meet multiple mechanical requirements of scaffold materials.(77) It has been a general method of obtaining very strong hydrogels by including various hydrophilic polymers, such as collagen, agarose, PHEMA as the first network, and poly(N,N'-dimethyl acrylamide) (PDMAAm) as the second network. The strength of hydrogels can be easily adjusted via changing the polymer matrixes and polymer ratios to make the scaffolds stiff or brittle.

Another challenge is mimicking the microstructures of native tissues to improve the biocompatibility of scaffolds, for example, muscles that have fibrillar structures due to the existence of fibre-like collagen. Combined with electrospinning technology, Ding *et al.* reported a photo-click PEG fibrous hydrogel as presented in Figure 1.10 and studied human pulmonary artery smooth muscle cells attachment to the material.(78) Compared with the flat photo-click PEG hydrogel (non-fibre like), significantly deeper muscle cell penetration was found in fibre hydrogels (~18 μm) versus the flat hydrogels (~7 μm) within 1 day. Although limited infiltration depth could be reached, this study proved that creating a material with a biomimetic microenvironment can facilitate material biocompatibility.

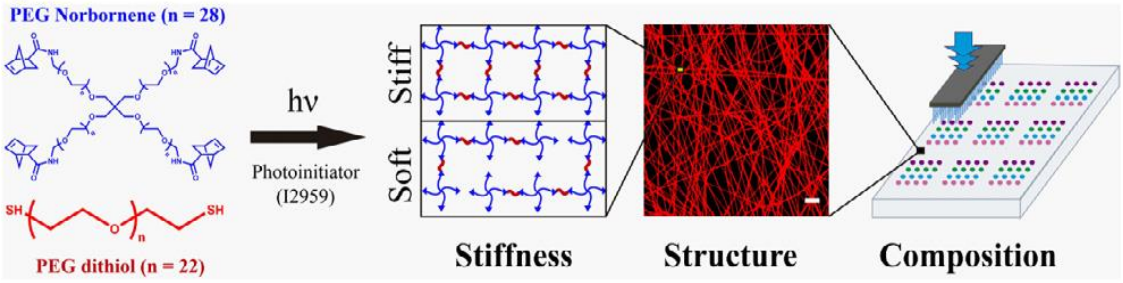

Figure 1.10 Schematic illustration of a fibrous hydrogel platform with tuneable stiffness, structure, and composition by integration of thiol-ene photo-click crosslinking chemistry, electrospinning, and combinatory protein array technology.(78)

Besides the mechanical strength and biocompatibility, more details should be considered when hydrogels are designed for particular tissue replacement, such as the moisture effect when hydrogels are applied for skin material,(79) and the influence of friction when hydrogels are used for artificial joint prosthesis,(80).

1.1.3.3.2 Tissue regeneration

Tissue regeneration requires hydrogels that not only have appropriate mechanical strength and biocompatibility, but also can promote cell proliferation/differentiation to help native tissue growth with appropriate gene expression. Natural biomacromolecules that are non-toxic and contain bioactive binding sites for cell attachment, including HA, collagen, and alginate, are ideally suited for this role.(81-83)

In collagen/alginate/fibrin tri-component hydrogels, it was reported that the stability and mechanical properties of the hydrogels could be increased by increasing the collagen content.(82) Significant proliferation of human-TERT mesenchymal stem cells (Y201 hMSCs) was found on the 0.5% and 1.0% w/v collagen tri-component hydrogels after 3 days culture. No significant cell proliferation occurred on the 2.5% w/v collagen hydrogel, whereas a significant increase of alkaline phosphate activity (ALP) of Y201 cells was detected in these hydrogels after 3 days culture. This interesting discovery of inhibited cellular proliferation with increased ALP activity implied osteoblastic differentiation and suggested osteogenic potential for bone regeneration.

Further research on using hydrogels for regenerative medicine that involved studying drug encapsulation and release has been performed. Yang *et al.* conjugated icarrin, a flavonoid constituent, onto HA and formed composite hydrogels with collagen to facilitate the reconstruction of the osteochondral interface.(83) Continuous and steady release of icarrin was recorded with 40% cumulative release within 144 hours, promising a biosafe and sustainable method for therapeutic delivery. The efficacy in osteochondral repair was proved through histology staining of *in vivo* rabbit experiments with obvious regeneration of upper hyaline cartilage and enhanced formation of new subchondral bone after three months.

1.1.4 Conclusion and expectation

The 3D network structure, high water-content, readily adjustable mechanical properties, and inherent biocompatibility ensure that hydrogels possess high suitability as biomaterials. Although much research concerning hydrogels being used as biomaterials has been reported, how to realise controllable material properties in a straightforward and cost-effective manner remains a challenge. Issues including controllable mechanical properties, controllable polymer degradability and gelation time must be addressed and optimised to target particular applications. Exploiting new modes of polymer crosslinking or further optimising existing crosslinking procedures is necessary to solve these issues.

For tissue engineering, creating a suitable matrix that forms a hydrogel of appropriate mechanical strength, degradability and biocompatibility and induces cell proliferation and differentiation is extremely important. However, as introduced above, creating a universal material that can fit all applications is likely to be unfeasible due to the complexities and variety associated with the various parts of the body. Consequently, biomaterial design must be highly tailored for the specific application.

In this project, hyaluronic acid-based hydrogels will be investigated as cell-friendly materials that have potential biomedical applications, including entities forwound healing management and osteoarthritis therapy.

1.2 HA hydrogels

1.2.1 Introduction to HA

HA is a natural linear polysaccharide, made up of repeating disaccharide units (β-1,4-D-glucuronic acid and β-1,3-N-acetyl-D-glucosamine) as presented in Figure 1.11. As a major constituent of the extracellular matrix, it is found

throughout the body from eyes to cartilages and has drawn considerable attention as a biomaterial. Its non-sulfated glycosaminoglycan structure and highly hydrated polyanionic status *in vivo* provided its unique biological functions in cellular blocking and signalling, biocompatibility, anti-adhesion, hydrophilicity, biodegradability, and non-immunogenicity.(81)

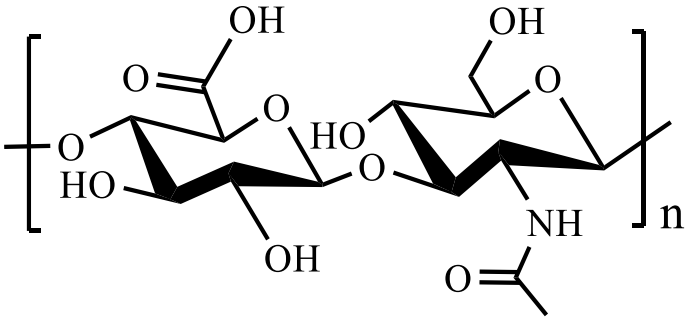

Figure 1.11 Repeat unit of Hyaluronic acid molecule.

1.2.2 HA-based hydrogels as Biomaterials

1.2.2.1 HA in maintaining bioactivity

Maintaining the bioactivity of native substances that exist in the extracellular matrix (ECM), including growth factors (84), peptides (85) and enzymes (86), that are necessary in regulating the metabolism of microorganisms and offering nutrition is a key aim of tissue regeneration. Silva *et al.* prepared a cellulose nanocrystals (CNCs) reinforced injectable HA hydrogel through hydrazone reaction between hydrazide-HA and aldehyde-HA/aldehyde-CNCs. This reaction also promoted an adjustable gelation time from 2.7±0.6 s to 127±31.3 s at room temperature depending on the component ratios. Through increasing the CNC content from 0% to 0.5 wt.%, significant prolonged release of vascular endothelial growth factor (VEGF) and platelet-derived growth factor (PDGF) were both realised from 2 days (0% CNCs) to 12 days (0.375 wt.% and 0.5 wt.% CNCs). The GFs stability within the hydrogels was also similar during 21-day cultivation

in basal medium, evaluated through the western blotting method.(84) However, a slight decrease appeared with the incorporation of aldehyde-CNCs.

Arginylglycylaspartic acid (RGD), a cell-binding peptide, was also introduced into HA hydrogel scaffolds and reported to improve cell attachment.(85) For example, oligopeptide $(Glycine)_4$-Arginine-Glycine-Aspartic acid-serine (G_4RGDS) was grafted onto pectin molecules and made into composite hydrogels with hyaluronic acid by Chen *et al.*(85) Primary porcine auricular chondrocytes were chosen for *in vitro* experiments and rat models were carried out for *in vivo* tests to investigate chondrocyte proliferation, differentiation (collagen type I) and chondrogenic marker gene expression (collagen type II and aggrecan). Significant improvements in collagen type II and aggrecan expression were observed in RGD-containing hydrogels after 21 days *in vitro* evaluation, compared with pure hyaluronic acid/pectin hydrogels in their optimised groups (5/5 weight ratio of hyaluronic acid/pectin), which proved the effectiveness and maintained activity of RGD in this hyaluronic acid matrix hydrogel.

1.2.2.2 HA as a soft tissue anti-adhesive

The polymeric network of HA hydrogels can enhance the free post-surgical movement of some soft tissues without impeding the diffusion of drugs, nutrients and metabolic bio-waste *in vivo*.(87-89) To eliminate postoperative peritoneal adhesion and subsequent complications, research into an injectable thermo-responsive hydrogel based on HA or similar carbohydrate-structure matrix, which presented great anti-adhesion property in animal experiments, has been conducted.(87-88) Through introducing poly(N-isopropylacrylamide) (PNIPAm, a thermal sensitive polymer) into the hydrogel system, a thermal gelled copolymer of HA/chitosan/PNIPAm (HA-CS-PNIPAm) was obtained during a heating process from 20 °C to 50 °C. A dramatic increase in storage modulus was

recorded from 0 (<30 °C) up to ~320 Pa (~42 °C) in HA-CS-PNIPAm hydrogel with a 3.1 times higher storage modulus value than the pure PNIPAm control hydrogel at 37 °C.(87) Injectable gelation *in vivo* was then successfully achieved based on this excellent thermo-responsive property and hydrogel membranes formed upon HA-CS-PNIPAm copolymer solution (10%, w/v) injection into sidewall defect-cecum abrasion rat models. An obvious reduction in peritoneal-intestinal adhesion was observed after 2-week tracing, compared with pure PNIPAm and the untreated control. This material has great potential for clinical therapy in either intraabdominal or gynecologic surgery.

1.2.2.3 HA as a 3D cell culture scaffold

Growing cells in a 3D environment to mimic native tissues in the living body is valuable to research for biomedical engineering, and a lot of hyaluronic acid-based hydrogels have been studied with the aim of creating a 3D microenvironment.(90-93)

Poly(N_{ε}-acryloyl-L-lysine)/hyaluronic acid (pLysAAm/HA) hydrogels were successfully prepared through photo-polymerisation and revealed increased MCF-7 breast cancer cell adhesion from ~50% (2D cell culture on tissue culture plates) to ~70% (3D culture in pLysAAm/HA hydrogels) after 4 hours.(90) Overexpression of proangiogenic growth factors, improved cell migration and penetrating abilities were observed *in vitro* after 7 days when cells were cultured in pLysAAm/HA hydrogels, and a significantly expanded volume of implant tumour in mice after 30 days was observed. This material provided a mimetic microenvironment for breast cancer research, however, further studies concerning the extent that the material affects gene secretion of other cell types and the related diseases would also be of value.

Stem cell growth has also been studied in 3D culture. Through radical polymerisation of methacrylated hyaluronic acid (HA-MA) under the existence of thiolated heparin (Hep-SH), which behaved as chain transfer agent, Gwon *et al.* formed Hep-HA hydrogels and investigated the spreading, proliferation, and migration of adipose-derived mesenchymal stem cells (ADSCs) in 3D cultivation.(91) They found that soft Hep-HA hydrogels (2 wt.% polymer) were more effective than stiff Hep-HA hydrogels (5 wt.% polymer) for ADSCs proliferation and migration, and provided the most suitable environment of all test groups, including tissue culture plates. The ability to maintain the function of ADSCs was proved by slightly increased or continuous mRNA expression of the pluripotency markers (Oct4, Sox2, and SSEA4) of ADSCs in soft Hep-HA hydrogels during 1 week, compared with decreased expression in other groups. The selectivity of this hydrogel for ADSCs was also confirmed by comparing with human osteoblast cell line (MG63) that MG63 in Hep-HA hydrogels maintained spherical morphology and some death of MG63 cells were observed, indicating that Hep-HA hydrogels cannot support MG63 proliferation and further suggesting that individual material design is required for different cell types.

1.2.2.4 HA as a joint tissue lubricant

Composed of glucuronic acid and glucosamine units, HA presents mild degradability without releasing any harmful substance during hydrolysis. The wide existence of HA is not limited to the ECM, it is also the main component of synovial fluid, which offers HA promise as a lubricant to reduce cartilage and bone abrasion for osteoarthritis (OA) treatment. Feng *et al.* found that HA hydrogels can reduce OA symptoms of rats after 28 days *in vivo* compared with PBS solution.(93) They also found that negatively charged sulfate-modified HA hydrogels have improved therapeutic effectiveness compared to pure HA

hydrogels, with a smoother articular surface and closer thickness compared to healthy cartilage as observed through histology staining. A higher sulfated content of 2.86% (elemental percentage of sulfur) to each HA molecule provided a better condition for chondrogenesis promotion and hypertrophy suppression of encapsulated human mesenchymal stem cells, compared with low-sulfated content of 1.61% (elemental percentage of sulfur) *in vitro*, and also prolonged degradation of HA hydrogels.

1.2.3 Structure-property of HA-based hydrogels in therapeutic use

HA batches of various molecular weights and concentrations are applied to different applications areas due to differences in the polymer properties. A broad range of molecular weights from 100 KDa to 8,000 KDa are found throughout human body. However, it is difficult to determine the particular variant of HA for a specific application due to such variations.(94-95) General commercial categories of HA in terms of molecular weight and dosage, and the consequent application are presented in

Table 1.1 and Table 1.2. This information is provided by Bloomage Bio Technology Corporation Limited (Freda@) who conduct extensive research to create hyaluronic acid-based products for skin care applications such as moisturisers, anti-aging and skin regeneration treatments, and injectable hyaluronic acid gels. Professional and systematic work is presented on the official website of Freda@.(94-95)

Table 1.1 Functions of hyaluronic acid with different molecular weight.

Molecular weight (kDa)	HA hydrogel applications
≤10	Trans-dermal absorption, deep hydrating, anti-ageing, repairing skin damage
10~1,000	Nourishing the skin, long-lasting moisturizing
≥1,000	Lubricating and film-forming, moisturizing, preventing skin damage, thickening and keeping emulsion stable

Table 1.2 Functions of hyaluronic acid in different dosage.

Dosage	HA hydrogel applications
0.1% ~ 0.5% for HA powder	cream, emulsion, essence, lotion, gel, facial mask, etc.
10% ~ 50% for HA solution	lipstick, eye shadow, foundation, etc.
1%~5% for Hyacross	facial cleaner, body wash, etc.
0.5%~1% cation HA	shampoo, hair conditioner, styling gel, hair restorer, etc.

This project uses a 1,200 kDa Hyaluronic acid powder product as a matrix for the formation of hydrogels containing different HA concentrations., Hydrogel

mechanical properties and microstructure are evaluated to ensure suitable porosity for cell growth and bioactive substance transfer, which are essential if the material is to be used for the growth and proliferation of cells.

The choice of crosslinker is another crucial factor in hydrogel preparation. Many naturally-occurring macromolecules such as DNA,(67) peptides(85) and enzymes(86) have been studied as biosensors, or to maintain cell bioactivity. However, the high cost of these naturally-occurring products renders relatively low-cost PEG a popular chemical crosslinker to form HA hydrogels with promising biomedical potentials that can achieve adjustable swelling ratio, rheological properties and degradation time.(96) Unsaturated carbon-carbon double bonds were introduced into the backbone of hyaluronic acid and mixed with thiol-terminated PEG to prepare chemical hydrogels through photo-polymerisation, using Darocur 2959 (D-2959, 2-hydroxy-1-[4-(hydroxyethoxy) phenyl]-2-methyl-1-propanone) as the initiator. The results revealed that increased molar ratio of thiol/acrylate increases the swelling ratios of the hydrogels and increases the degradation time from 2 days to 7 days.(96) Furthermore, a secondary network can also be designed and achieved in a pre-PEG-HA hydrogel. For example, in a tannic acid/PEG crosslinked HA hydrogel system, increased storage modulus, cell attachment and proliferation of L929 mouse fibroblast cell line, anti-oxidant capacity were observed when immersing the PEG crosslinked hydrogels in variable concentrations of tannic acid for 2 days (from 0 to 0.15% (w/v).(97) The exploitation of low-cost, and multifunctional crosslinkers that enable HA-based hydrogels to be created with stimuli-responsive behaviours is a key concept to this project.

1.2.4 Summary

Biopolymer-based hydrogels have been widely used as effective biomaterials in recent years. Many bioactive substances that mimic the extracellular microenvironment, and different cross-linkers, have been studied to realise hydrogels that possess appropriate requirements for particular biomedical applications. In particular, HA demonstrates great potential as a cell-friendly macromolecule that may be exploited as a scaffold for cell growth and proliferation. However, consideration for material design to match the specific application is imperative because (1) Some HA hydrogels demonstrate less than optimal cell attachment, (2) Some HA hydrogels cannot support ADSCs attachment despite HA having a CD44+ receptor, and (3) the mechanical properties of the hydrogel may not suitable for cell adhesion.(91) Consequently, it is important that new HA-based hydrogels are devised and generated for particular biomedical applications.

This project will focus on creating hyaluronic acid hydrogels for biomedical applications based on the three basic requirements which were brought up by Wichterle and Lím when they applied hydrogels to biological use, (i) a structure containing the desired water content; (ii) inertness to normal biological processes (i.e. resistance to unfavourable reactions in the organism); (iii) permeability for metabolites.(1)

HA-based hydrogels that possess stimuli-responsiveness for chronic wound management and diagnosis are reported in Chapter 2. The design of this material was focused on the redox reaction between disulfide bridges present in the crosslinker, and thiol groups present in the target molecule glutathione (GSH). Changes in the hydrogel mechanical properties, network stability and morphology were assessed, before an investigation into how mechanical properties of these

hydrogels could be reinforced to mimic biomineralisation for bone repair (Chapter 3).

Injectable hydrogels were created for potential use in the repair of joint tissue. In material design, physical crosslinking was introduced into the reaction system to build up metal-polymer networks, notably an iron(III)-HA network. To reduce the cytotoxicity of Fe^{3+} and stabilise thiol groups in bioactive molecules, a cell friendly Iron(III)-glutathione complex was prepared in an additive-free way and characterised (Chapter 4). This complex successfully acted as a physical crosslinker that connected hyaluronic acid macromolecules, forming networks with increased viscosity and storage modulus. The injectable physical hydrogel reported has great potential for the facilitation of tissue regeneration (Chapter 5).

Both chemical and physical HA-based hydrogels were studied in this work and further details of these promising biomaterials are discussed in the following chapters.

Chapter 2

A glutathione-responsive hyaluronic acid-based hydrogel for chronic wound management

- This chapter has been published. Reference [Gao, Z., Golland, B., Tronci, G. and Thornton, P.D. 2019. A redox-responsive hyaluronic acid-based hydrogel for chronic wound management. *Journal of Materials Chemistry B*. **7**(47), pp.7494–7501.]

Polymer-based hydrogels have been widely applied for chronic wound therapeutics, due to their well-acclaimed wound exudate management capability. At the same time, there is still an unmet clinical need for simple wound diagnostic tools to assist clinical decision-making at the point of care and deliver on the vision of patient-personalised wound management. To explore this challenge, a one-step synthetic strategy to realise a redox-responsive, hyaluronic acid-based hydrogel that is sensitive to wound environment-related variations in glutathione (GSH) concentration is presented. By selecting aminoethyl disulfide (cystamine) as a GSH-sensitive crosslinker and considering GSH concentration variations in active and non-self-healing wounds, the impact of GSH induced cystamine cleavage on hydrogel dimensions was investigated with the aim to build GSH-hydrogel dimension relationships for potential point-of-care wound diagnosis. The hydrogel obtained was also found to be non-cytotoxic and aided L929 fibroblast growth and proliferation over seven days *in vitro* cell culture study. Such a material offers a very low-cost tool for the visual detection of a target analyte that varies dependent on the status of the cells and tissues (wound detection), and may be further exploited as an implant for fibroblast growth and tissue regeneration (wound repair). An overall illustration of this hydrogel for wound management process is presented in Figure 2.1.

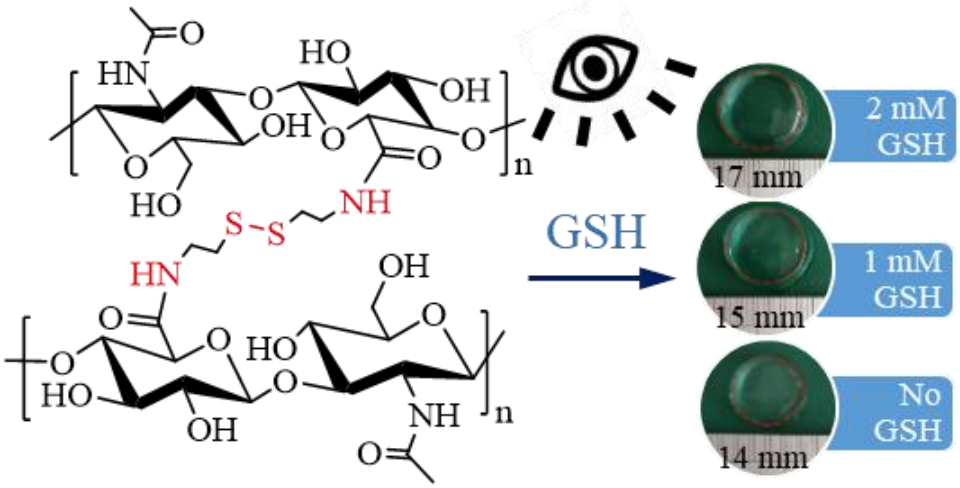

Figure 2.1 Illustration of GSH-responsive HA hydrogel for wound management. The hydrogel diameter change as increasing GSH concentrations can be observed by naked eyes.

2.1 Introduction

Polymeric hydrogels have emerged as highly promising materials for a range of biomedical applications, including carriers for controlled drug delivery,(98-100) protein adsorption,(101) the creation of contact lenses,(102-103) and as injectable implants.(104-105) The water-dominated composition of hydrogels renders them suitable for deployment *in vivo*, ensuring that such non-cytotoxic materials are also excellent candidates for use as scaffolds that facilitate tissue regeneration.(106-109) In addition, hydrogels that undergo an actuated change in dimensions in response to a target analyte may act as biosensors. Such materials have been deployed for the detection of bacterial enzymes,(110) toxins,(111) disease specific genes,(112) and pathogenic proteins that are associated with particular disease states.(113) Polymer hydrogels therefore hold great promise as materials for chronic wound management, both for the detection of chronic wound-associated markers as a mode of diagnosis, and by providing a scaffold for fibroblast growth, and subsequent new tissue generation, as part of wound healing.

Chronic states, such as those associated with non-self-healing ulcers, exhibit excessive oxidant stress, leading to upregulated reactive oxygen species (ROSs), inhibited cell migration and proliferation, and growth factor deficiency.(114) Whilst antioxidants regulate endogenous oxidant production in active wounds so that repair occurs via an orderly process, non-self-healing ulcers are in a persistent inflammation state, whereby prolonged infiltration of polymorphonuclear leukocytes and mononuclear cells results in reduced concentration of antioxidants, for instance GSH, and incorrect redox potential in the cells.(115) Tracking biochemical shifts, such as antioxidant concentration, could therefore be useful to diagnose changes in wound chronicity and assist with

clinical decision making. Given that wound diagnosis relies on clinical assessment,(116) hydrogels with inherent oxidation responsivity could play a significant role as a cost-effective point-of-care diagnostic system. Following hydrogel contact with the wound, oxidation-induced changes in hydrogel size could be exploited to describe defined chronic wound states and inform clinical therapies.

Hyaluronic acid (HA), a natural polysaccharide that is a major constituent of the ECM, offers biocompatibility, anti-adhesion, biodegradability, and non-immunogenicity.(117) HA content within the human body is approximately 15 g (for a 70 kg human), and largely resides in the skin and musculoskeletal tissue.(118) The hydrophilicity of HA ensures that it is an excellent candidate for use as a gelator within both physical(119) and chemical hydrogels.(120) HA-containing hydrogels have been reported as effective scaffolds for the regeneration of bone,(121) cartilage,(122) neural tissue,(123) and myocardial tissue.(124) In direct relation to wound healing, recent examples of HA-based chemical hydrogels include an anti-oxidative and anti-inflammatory drug release system for early tendinopathy intervention,(125) an *in situ*-forming biomimetic dressing for soluble factor-free wound healing,(126) a UV-cured drug-encapsulated antibacterial hemostat,(127) and injectable hydrogels for the management of osteoarthritic synovial fluids.(128) However, despite substantial efforts being afforded to the employment of HA as a component of a therapeutic system, limited reports have proposed the application of HA for chronic wound diagnostics, whereby expensive and sophisticated imaging apparatus are required.(129)

GSH, a natural tripeptide that consists of gamma linked glutamate, cysteine and glycine as shown in Figure 2.2, is abundant in the majority of animal cells. GSH

plays a key role in biological processes including biocatalysis, metabolism, signal transduction, gene expression, apoptosis and anti-oxidation.(130) GSH is present in both its reduced (GSH) and oxidized state (GSSG), and the ratio of the two variants dictate many pharmacological processes within the cell. The thiol that the cysteine unit presents ensures that GSH is a reducing agent and offers a signal for GSH detection.(131) The intracellular concentration of GSH is typically 0.5 mM for normal cells, compared to 10 mM for cancerous cells.(132) On the other hand, averaged GSH levels were found to be lower in diabetic foot ulcers, in line with the excessive oxidant stress in the former case.(133) Consequently, materials that are able to respond to GSH concentrations within this range hold great promise for the detection of pathological GSH concentrations that may be linked to either the onset of cancer or wound chronicity.

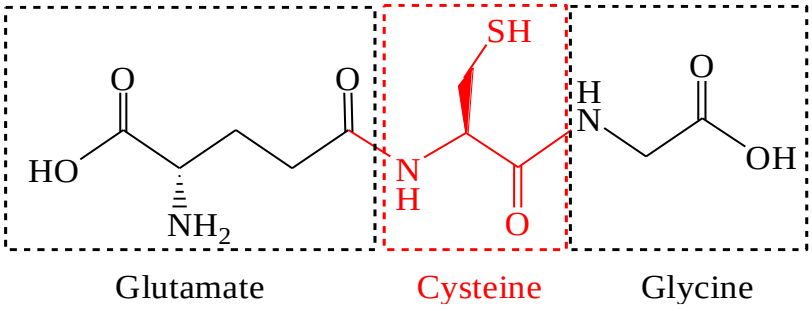

Figure 2.2 Molecular structure of glutathione reduced.

This chapter described the facile, one-step synthesis of a HA-based chemical hydrogel that is spatially responsive to the presence of GSH. Aminoethyl disulfide (cystamine) is employed as a dynamic covalent crosslinker that is sensitive to the presence of GSH; cystamine-GSH conjugation results in crosslinker cleavage, increased hydrogel swelling and a clearly visible change in hydrogel dimensions. The hydrogel was found to be non-cytotoxic and aided fibroblast growth and proliferation over seven days. Such a material offers a very low cost method for

the visual detection of a target analyte that varies dependent on the status of the cells and tissues (wound detection), and may be further exploited as a scaffold for fibroblast growth and tissue regeneration (wound repair).

2.2 Materials and methods

2.2.1 Materials

HA sodium salt (molecular weight: 1,200 kDa, cosmetic grade) was purchased from Hollyberry Cosmetic, 4-(4,6-dimethoxy-1,3,5-triazin-2-yl)-4-methyl-morpholinium chloride (DMTMM) and 2-(N-morpholino) ethanesulfonic acid (MES) were purchased from Fluorochem. cystamine, rhodamine B isothiocyanate-dextran (RITC-dextran) and ninhydrin reagent were purchased from Alfa Aesar. alamarBlue™ assay kit was purchased from ThermoFisher Scientific. All other reagents were purchased from Sigma-Aldrich.

2.2.2 Preparation of hyaluronic acid hydrogels

HA powder was dissolved in deionised water to prepare a 2 wt.% HA solution. MES buffer (0.1 M) was added at room temperature under stirring to provide a weak acid environment (pH 5.5). DMTMM (2 equivalents per HA repeat unit) was then added at 37 °C to activate the carboxyl groups of HA. The temperature was maintained at 37 °C for 1 hour, and a molar ratio of either 0.2 or 0.4 moles of cystamine relative to the moles of each HA repeat unit was added to the solution (Table 2.1). The stirring speed was increased to 1,000 $r \cdot min^{-1}$ for 5 minutes and either 0.6 g or 0.8 g of the reacting solution was cast into either 12- or 24-well plates, respectively. HA hydrogels were obtained after 2-hour incubation at 37 °C.

Table 2.1 The quantities of reagents used to make two covalent hydrogels.

Sample ID	HA (wt.%)	Cystamine (mol.% of HA)
C2-20	2.0	20.0
C2-40	2.0	40.0

2.2.3 Analysis of HA crosslinking

Attenuated total reflectance fourier transform infrared (ATR-FTIR) spectroscopy was used to characterise the crosslinked structure of HA hydrogels. IR spectra were obtained from freeze-dried networks and recorded between 4000 cm^{-1} and 500 cm^{-1} using a Bruker spectrophotometer at room temperature.

The thermal properties of both HA and the freeze-dried networks produced were evaluated by differential scanning calorimetry (DSC) using a DSC Q20 unit (TA instruments) calibrated with indium. DSC thermograms were recorded under nitrogen atmosphere with a heating rate of 10 °C·min^{-1} from 30 °C to 200 °C.

The progress of the crosslinking reaction was investigated by 2,4,6-trinitrobenzenesulfonic acid (TNBS) and ninhydrin assays.(134-135) TNBS was used to quantify any unreacted cystamine entrapped in the crosslinked network. 0.8 g of newly-synthesised hydrogel was freeze-dried and immersed in 2 mL $NaHCO_3$ (4 wt.%) at 40 °C for 30 minutes to wash away any unreacted cystamine; 1.0 mL of the supernatant was collected and investigated by TNBS assay. 1.0 mL TNBS solution (0.5 wt.%) was added to the supernatant in the dark and incubated at 40 °C for 3 hours with a rotation speed of 120 r·min^{-1}. 3 mL HCl (6 N) was added to the incubated solution and the temperature raised to 60 °C for 1 hour to terminate the reaction. After solution equilibration to room temperature,

the sample solutions were diluted with 5 mL H_2O. The unreacted TNBS was washed out by extraction with 20 mL diethyl ether, three times. 5 mL of the retrieved sample solution was immersed in hot water (~60 °C) in a fumehood to evaporate any diethyl ether, and diluted with 15 mL H_2O. Finally, 2 mL of solution was analysed by UV-Vis spectroscopy at 346 nm. Quantification of any cystamine residue was carried out by comparison with an cystamine calibration curve (calibration equation: y=0.0666x-0.0184, R^2=0.9933, y=absorbance, x= cystamine concentration, mM).

The presence of any terminal free amino group deriving from the grafting, rather than the complete crosslinking, of HA with cystamine was quantified by ninhydrin assay. 10 mg of washed, freeze-dried polymer was immersed in 1 mL water. 1 mL ninhydrin solution (8 wt.%) was then added in the dark, and the solution quickly immersed in a water bath at 95 °C for 15 minutes. 1 mL ethanol was added to stop the reaction after equilibration at room temperature. A calibration curve was obtained by measuring UV-Vis absorbance at 348 nm using various amounts of glycine.

2.2.4 Hydrogel swelling and degradation studies

Newly-synthesised hydrogels were weighed (m_w) and then immersed in deionised water. As control samples, another series of hydrogels was soaked in H_2O with 5 mM GSH to determine any hydrogel response. The mass of the samples (m_t) was recorded at selected time points (1, 2, 3, 4, 7, 14, 21, 28 days) following light sample blotting with tissue paper. The swelling ratio (SR) of each hydrogel was calculated using the following Equation 2.1:

$$\boldsymbol{SR = \frac{m_t}{m_w} \times 100} \qquad \text{Equation 2.1}$$

Hydrogel degradability was evaluated via gravimetric analysis of the covalent networks following incubation in aqueous solutions and drying. The initial network mass of hydrogel C2-20 was recorded as m0. 0.8 g of hydrogel C2-20 was immersed in PBS solution either with GSH (5 mM) or without GSH. Samples were collected following 1, 2, 3, 4, 7, 14, 21 and 28 days, washed with deionised water, freeze-dried and weighed (m_d). The percentage of the crosslinked network remaining (μ_{rel}) was calculated via the following equation:

$$\boldsymbol{\mu_{rel} = \frac{m_d}{m_0} \times 100} \qquad \text{Equation 2.2}$$

2.2.5 Mechanical tests

Hydrogels were tested using a rheometer (Anton Paar, MCR 302) with a 25 mm parallel plate. Frequency sweeps were recorded at 100-1 rad·s^{-1} with a constant amplitude (1%) at room temperature, using a 0.8 g hydrogel and a 2 mm gap. Time sweep measurements were carried out to quantify hydrogel gelation kinetics following the reaction of HA with cystamine. 0.6 mL of solution was injected homogenously on the sample holder and tested with a 25 mm parallel plate. The measurement was carried out at 37 °C over 150 minutes with constant amplitude (1%) and frequency (5 Hz).

Compression measurements were conducted using Bose ELF 3200 apparatus. All the hydrogel samples (Ø: 3 mm; h: 3 mm) were tested with a compression speed of 0.02 mm·s^{-1}.

2.2.6 Scanning electron microscopy (SEM)

The network microstructure of newly-synthesised and partially-degraded networks was inspected by SEM using a JEOL JSM6610LV microscope under 5

kV voltage following gold coating. Freeze dried samples were collected following either synthesis or 2-day immersion in 20 mL solution of either PBS or GSH (5 mM)-supplemented PBS. Pores (n=20-60) were visualised and their diameter measured through Image J software.

2.2.7 Macromolecule uptake studies

Hydrogels were loaded with RITC-dextran (Mn: 70,000 $g \cdot mol^{-1}$, Alfa Aesar), as a model macromolecule. 0.6 g hydrogel was immersed in 2 mL RITC-dextran-containing (0.5 $mg \cdot mL^{-1}$) PBS solution at 37 °C for 24 hours. Samples were washed with PBS solution to remove any surface-coated RITC-dextran before being transferred into 3 mL PBS solution that contained various GSH concentrations (0-20 mM). RITC-dextran uptake was calculated through the difference in supernatant absorbance before and after RITC-dextran loading (calibration equation: $y=0.0011x-0.004$, $R^2=0.9995$, y=absorbance, x= RITC-dextran concentration ($\mu g \cdot ml^{-1}$)).

The change of hydrogel network structure, and the distribution of RITC-dextran loaded in the hydrogel, was investigated by analysis of the lyophilised networks of hydrogels that had undergone incubation in PBS solution that contained or lacked SH at 37 °C, by laser scanning confocal microscopy (LEICA TCS SP8, excitation wavelength 552 nm).

2.2.8 Hydrogel response to simulated wound fluid

Simulated wound fluid (SWF) was prepared as reported.(136) Briefly, 5.844 g sodium chloride (NaCl), 3.360 g sodium hydrogen carbonate ($NaHCO_3$), 0.298 g potassium chloride (KCl), 0.278 g calcium chloride ($CaCl_2$) and 33.00 g bovine serum albumin (BSA) were dissolved into 1 L of deionized water. 0.6 g of hydrogel was immersed in 20 mL SWF loaded with varied GSH content (0-20 mM) to mimic

multiple wound chronic states. All the samples were incubated at 37 °C, stirred at 100 $r \cdot min^{-1}$ and any change in hydrogel size recorded by eyes and optical images following 24-hour incubation.

2.2.9 Cytotoxicity evaluation

Hydrogel (8 mm^3) was incubated in 70 wt.% ethanol (×3), and then washed in PBS buffer (×3), and ultimately in cell culture medium (×3). L929 murine fibroblasts were cultured (37 °C, 5% CO_2) in Dulbecco's modified eagle medium (DMEM) supplemented with 10 vol.% fetal bovine serum (FBS) and 0.5 vol.% penicillin–streptomycin. The cell suspension (1×10^4 $cells \cdot mL^{-1}$) was transferred to a 96-well-plate (200 $\mu L \cdot well^{-1}$), followed by application of individual hydrogel samples to each well. Cell viability was quantified by alamarBlue™ Assay after 1-7-day culture following the product protocol from ThermoFisher. Cells cultured on either tissue culture plates (TCPs, positive control) or non-treated tissue culture plates (NTCPs, negative control) were set as a positive control and a negative control, respectively.

2.2.10 Statistical analysis

For statistical analysis, all the cytotoxicity results were analysed at least three times. The significant difference was calculated through One ANOVA analysis with a p level at 0.05. The results are presented as *$p \leq 0.05$, **$p \leq 0.01$, ***$p \leq 0.001$, ****$p \leq 0.0001$.

2.3 Results and discussion

Chemical hydrogels were successfully generated from a 2 wt.% HA aqueous solution by crosslinking HA with either 20 mol.% (C2-20) or 40 mol.% (C2-40) cystamine, with respect to HA carboxylic acid groups (Figure 2.3).

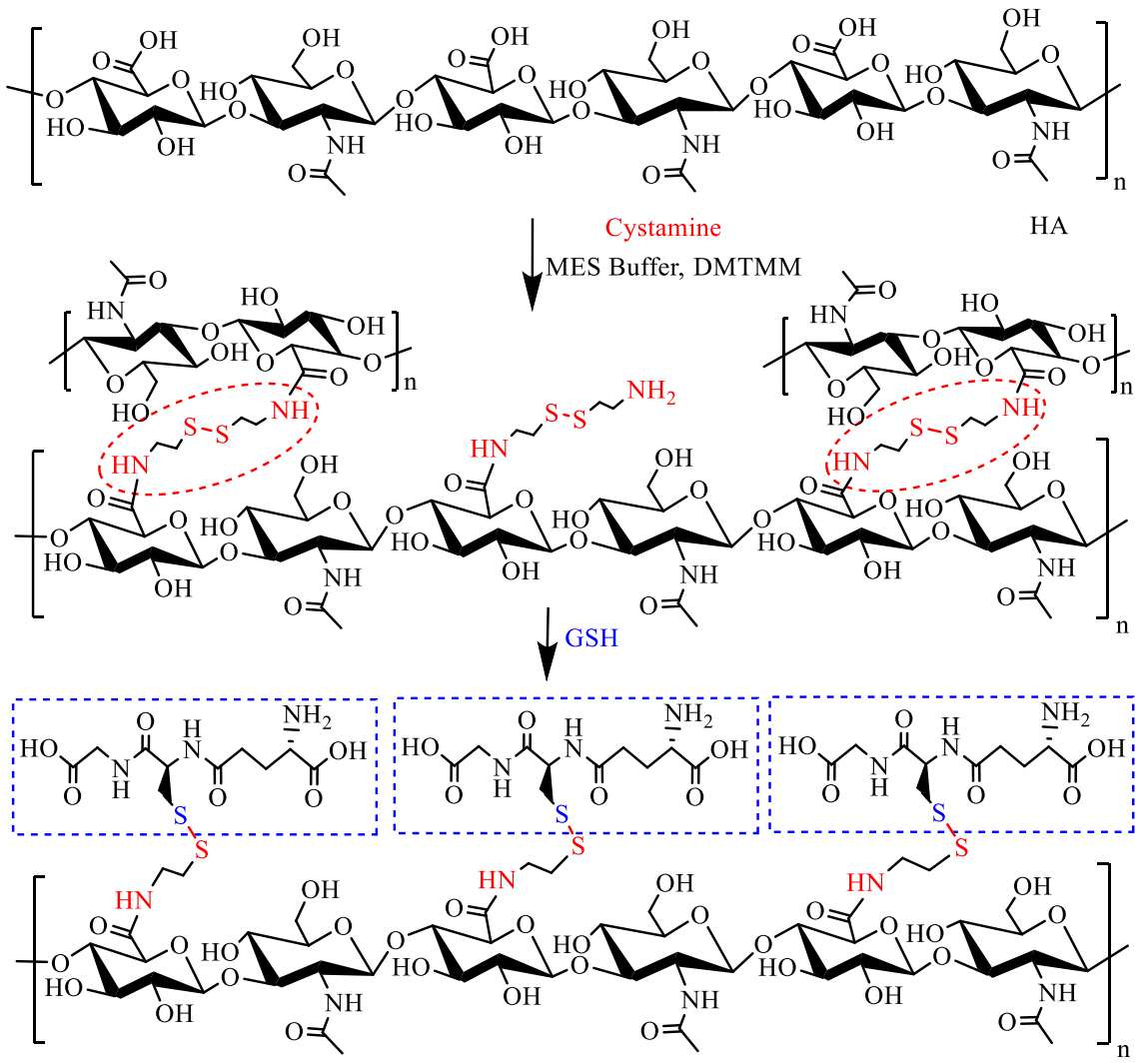

Figure 2.3 Schematic illustration of hydrogel formation and redox-reaction. The reaction between cystamine and HA chains yields a crosslinked polymer that forms a chemical hydrogel when maintained in aqueous solution. GSH-induced cystamine disulfide reduction disrupts the crosslinked network, resulting in changes to the hydrogel dimensions and mechanical properties.

Qualitative confirmation of HA crosslinking was achieved by FTIR spectroscopy (Figure 2.4); the spectrum of the crosslinked networks revealed a peak at 1700 cm^{-1}, which corresponds to the amide bonds formed between HA and cystamine. In addition, the peak present at 538 cm^{-1} in the crosslinked samples is attributed to the presence of disulfide bonds that are present within cystamine molecules. For C2-20, TNBS and ninhydrin assays revealed that 82 mol.% of cystamine

amine groups had reacted to form a complete covalent crosslink, rather than forming cystamine -grafted residues. In the case of C2-40, 61 mol.% of amine groups presented by cystamine had reacted.

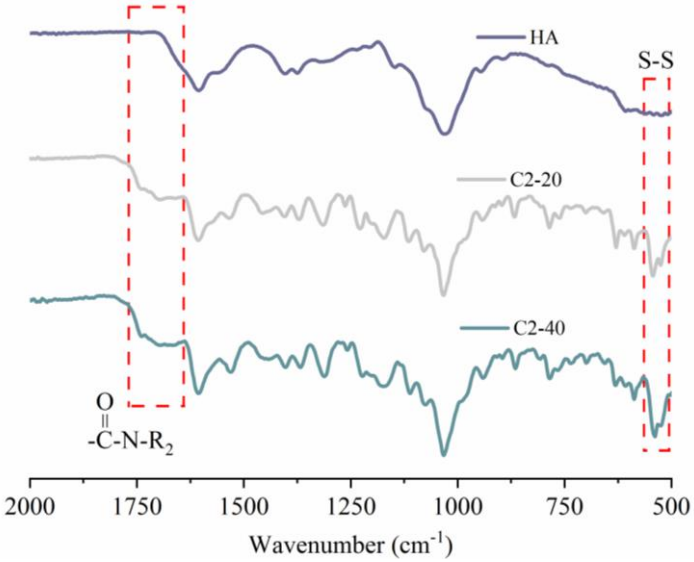

Figure 2.4 FTIR spectrum of HA (top), hydrogel C2-20 (middle) and C2-40 (bottom). Red squared the peaks that confirm successful HA functionalisation.

DSC analysis revealed broad endothermic peaks from 63.6 °C -80.9 °C that were attributed to water evaporation. The exothermic peak at 138.9 °C (C2-20) and 143.0 °C (C2-40) in the thermograms of the crosslinked polymers that were absent from the thermogram corresponding to HA (Figure 2.5). These additional peaks may be ascribed to the thermal decomposition of the cystamine crosslinks.

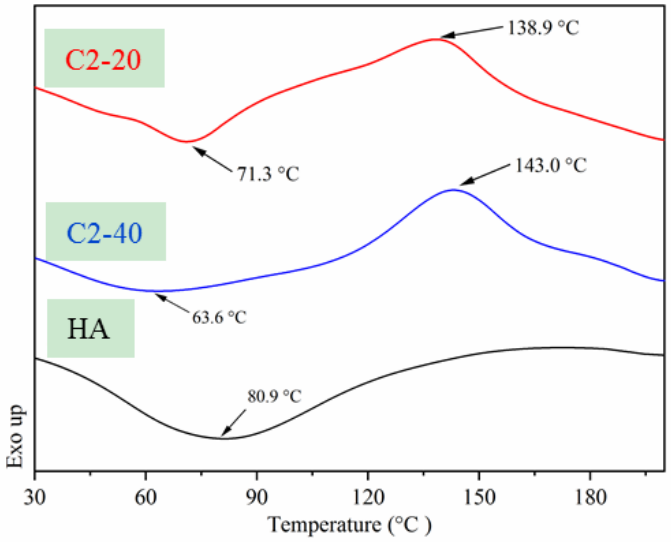

Figure 2.5 DSC thermograms corresponding to the crosslinked polymer used to form C2-20 (top) and C2-40 (middle), and linear HA.

Rheometry was carried out to investigate the kinetics of the crosslinking reaction. Rheograms revealed that C2-20 was formed with a storage modulus (G') of 885 Pa and a loss modulus (G'') of 9 Pa after 130 minutes (Figure 2.6), whilst C2-40 was formed with a G' of 1029 Pa and a G'' of 13 Pa after 140 minutes (Figure 2.6). The value of G' in sample C2-40 was slightly higher than C2-20, which might suggest a higher crosslinking density.

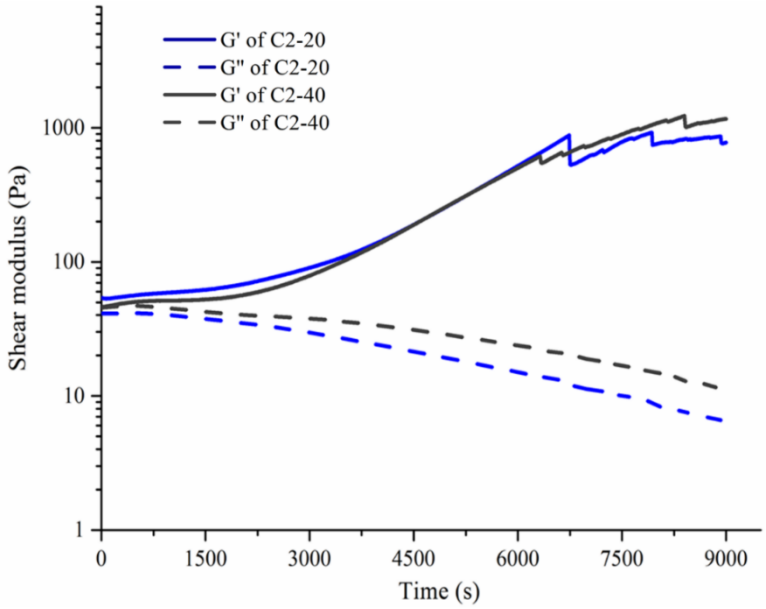

Figure 2.6 Rheological analysis during HA crosslinking to assess gelation kinetics for C2-20 (blue) and C2-40 (grey). The solid line corresponds to G' and the dash line corresponds to G".

Results of both C2-20 and C2-40 confirmed that the hydrogels can be created in a simplie manner within a relatively short timeframe; the gel hardening times displayed by hydrogels formed from reacting mixtures containing cystamine may be attributed to the occurrence of grafted rather than crosslinked HA chains, as supported by TNBS and ninhydrin results. These results give indirect evidence of the impact that the HA/cystamine molar ratio has on the network crosslinking yield. Overall, rheological analysis revealed that the storage modulus of both crosslinked materials exceeded the loss modulus. This confirmed their classification as hydrogels that storage modulus appeared higher than loss

modulus in rheology and the formation of a solid-like hydrogel rather than a viscous liquid (Figure 2.7).

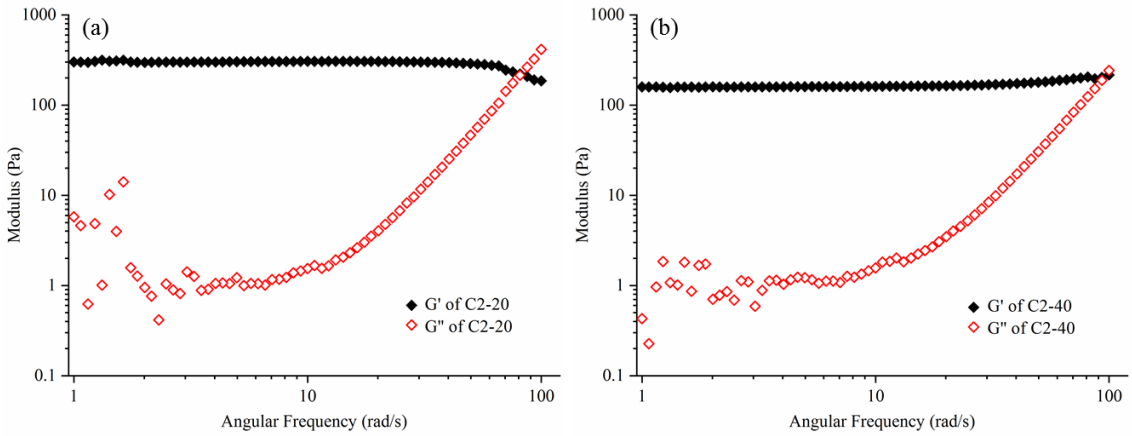

Figure 2.7 Frequency sweep rheological analysis revealing the storage (G') and loss (G'') modulus of hydrogel C2-20 (a) and C2-40 (b).

Due to the superior crosslinking efficiency, hydrogel C2-20 was chosen for further investigations concerning its swelling capabilities, and its susceptibility to disassemble in the presence of the target analyte, GSH. When incubated in deionised (DI) water, newly-synthesised C2-20 displayed a 700 wt.% mass increase after 21 days (Figure 2.8a). In contrast, when incubated in the presence of aqueous GSH solution (5 mM), C2-20 started to break and could not be weighed after two days owing to the fragility of the material. This strongly advocates that GSH-induced cleavage of the disulfide bonds in cystamine-crosslinked HA chains occurs, resulting in the disintegration of the covalent network due to GSH-cystamine bond formation (Figure 2.3). The mass of lyophilised polymer that had been maintained as a hydrogel in aqueous solution that contained GSH was greater than the mass of polymer that had previously been maintained as a hydrogel in aqueous solution that lacked GSH (Figure 2.8b). The difference in the mass of recovered polymer is credited to GSH conjugation to the HA backbone. After four days storage in GSH solution the

hydrogel could not be recovered, rendering lyophilisation and subsequent mass recording was impossible.

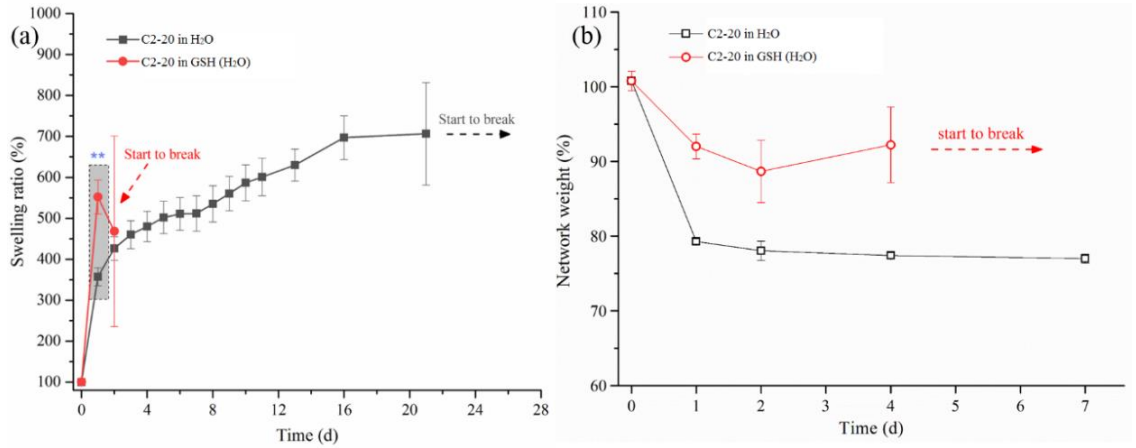

Figure 2.8 Hydrogel C2-20 swelling (a) and degradation (b) in DI water (black line) versus C2-20 swelling in aqueous GSH solution (5 mM, red line).

Next, the compression properties of C2-20 were investigated. C2-20 exhibited great compressibility as evidenced through stress-compression curves (Figure 2.9a), which was usually applied to evaluate the compressive property of materials. Following 48-hour incubation in GSH (5mM)-supplemented PBS solution, the stress at break of C2-20 was significantly lower than the stress at break of both the newly-synthesised C2-20, and C2-20 following 48-hour incubation in GSH-free PBS solution (Figure 2.9b). The original hydrogel could hold up to 82% compression with stress at break of 90±8 kPa. After being immersed in PBS for 48 hours, a slight decrease in stress at break was observed (σ_b= 75±10 kPa) and the compression at break was also reduced to 80%. In the presence of GSH solution, a significant decrease in stress at break (σ_b = 30 kPa), and compression at break (ε_b= 62%) was observed after 48 hours, providing convincing evidence for GSH-mediated hydrogel disassembly.

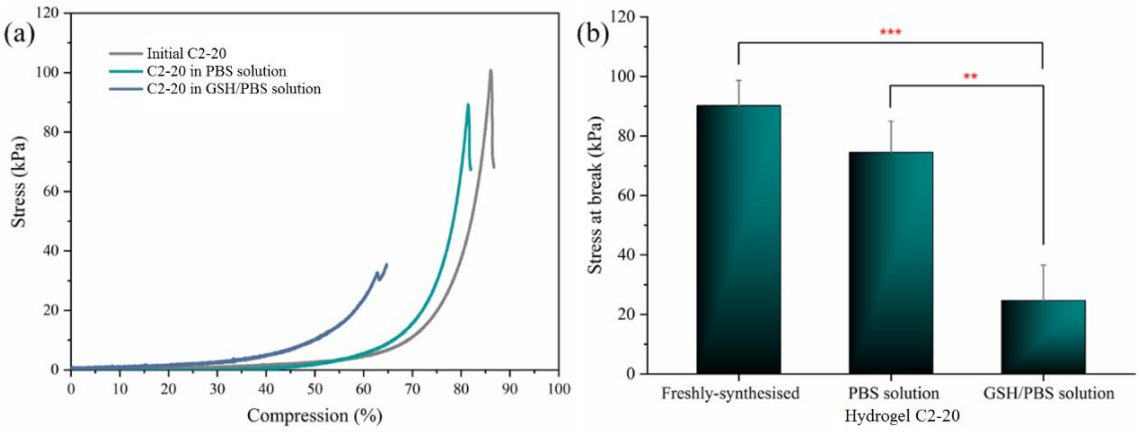

Figure 2.9 (a) Stress-strain curves corresponding to C2-20, C2-20 stored in PBS buffer solution for 48 hours, and C2-20 stored in PBS buffer solution that contained GSH (5 mM) for 48 hours. (b) The breaking stress values of C2-20, C2-20 stored in PBS buffer solution for 48 hours, and C2-20 stored in PBS buffer solution that contained GSH (5 mM) for 48 hours.

The morphology of C2-20 incubated in PBS buffer or GSH-supplemented PBS buffer were assessed by SEM (Figure 2.10), to investigate whether GSH-induced network disintegration resulted in significant changes in material microstructure. SEM images of lyophilised hydrogels were captured following 48-hour incubation, at which point the GSH-treated material was no longer stable in hydrogel form. Clear differences in the morphologies of the two samples can be observed; in the absence of GSH, the material presents a predominantly smooth surface that largely lacks major defects, whereas in the presence of GSH the material contains substantial pores that are ascribed to GSH-mediated crosslinker cleavage (Figure 2.10 a and b, respectively). The freeze-dried internal structure of C2-20 is porous, with an average pore diameter of 58±18 µm (Figure 2.10c). The internal pore diameter of the GSH-treated (48 hours) hydrogel was found to be 176±89 µm after the same lyophilisation process as initial C2-20, whereby the greater pore size again supports the rationale for the degradation effect that GSH has on the crosslinked polymer structure (Figure 2.10d).

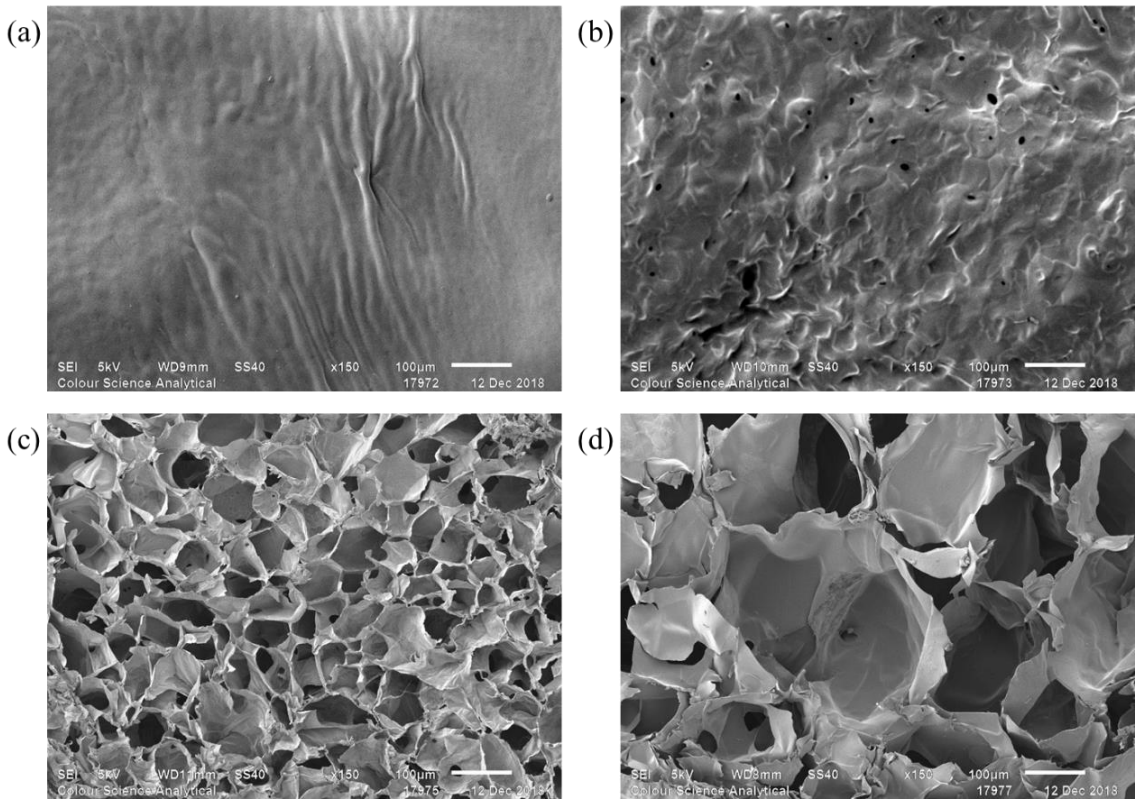

Figure 2.10 SEM images of C2-20 after 48-hour incubation in either PBS solution (a, c), or GSH-supplemented PBS solution (5 mM) (b, d). Scale bar: 100 µm.

In order to apply the hydrogel within a diagnostic setting, the uptake of RITC-dextran by C2-20 was assessed by confocal microscopy. The hydrogels were incubated in RITC-dextran solution, prior to lyophilisation and analysis of the recovered polymeric network. When the hydrogels are incubated in greater concentrations of GSH, more extensive scaffold disruption, and increased gel porosity, arises due to the onset of network degradation. Consequently, the fluorescent marker is able to penetrate more readily in the partially-degraded network upon network cleavage induced by increasing GSH levels (Figure 2.11). The depth to which RITC-dextran was able to penetrate the hydrogel was related to GSH concentration, increasing from 125 µm (No GSH) to 200 µm (5 mM), 250 µm (10 mM), up to 300 µm (20 mM GSH).

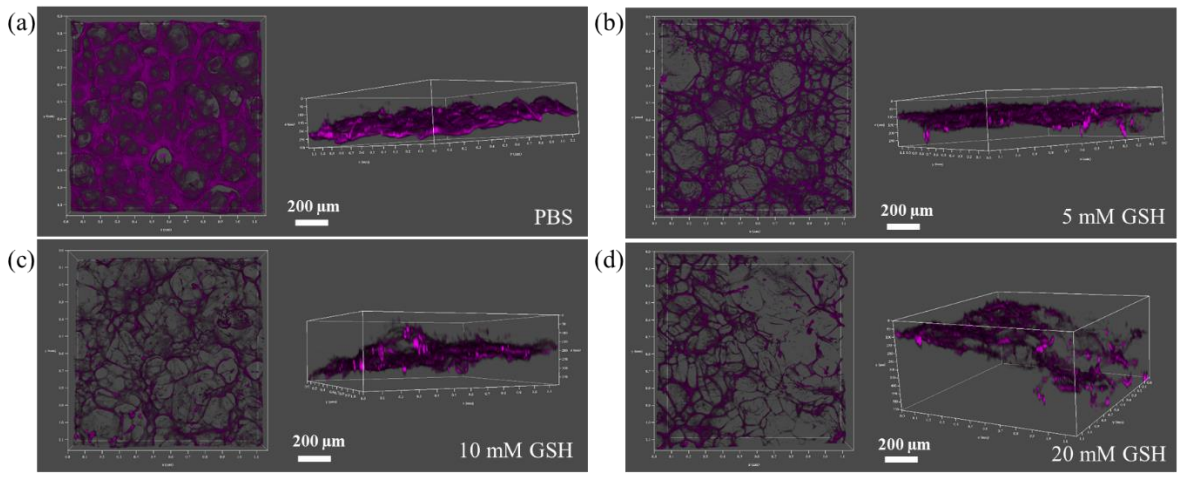

Figure 2.11 Confocal images of lyophilised C2-20 hydrogel network loaded with RITC-dextran in (a) PBS solution, and PBS solution supplemented with (b) 5 mM GSH, (c) 10 mM GSH, and (d) 20 mM GSH. The stained polymer network is provided in the left-hand image of each box, and becomes increasingly disintegrated with increased GSH concentration. The depth to which RITC-dextran was able to penetrate the hydrogel was related to the fluorescence depth profile for each hydrogel and is provided in the right-hand image of each box. Scale bar: 200 µm.

The pronounced effect that GSH has on hydrogel swelling may also be exploited to realise a diagnostic device that undergoes dimension changes that are visible to the naked eye upon interaction with GSH. Figure 2.12 demonstrates the macroscopic changes in C2-20 swelling that occur when the hydrogel is incubated in simulated wound fluids that contain various concentrations of GSH, as a mimetic of varying chronic wound states. As anticipated, hydrogel swelling increases with increasing GSH concentration due to a reduction in the covalent crosslinks that originally maintain the hydrogel. Increasing the GSH concentration from 0 mM to 5 mM results in an increase in hydrogel diameter by ~43%. Increasing the solution GSH concentration from 0 mM to 10 mM results in the hydrogel diameter increasing by 63%, and increasing the GSH concentration

from 0 mM to 20 mM results in hydrogel dissolution (Figure 2.13). As average GSH levels are found to be lower in diabetic foot ulcers (53.4 pmol·mg^{-1} wet weight), compared to control tissues (150.6 pmol·mg^{-1} wet weight), material expansion would be a sign of healthy tissue. Conversely, elevated GSH levels in tumour tissue compared to healthy tissue, and the accompanying increase in hydrogel dimensions, may act as a simple diagnostic test for the exposure of cancerous cells.(137)

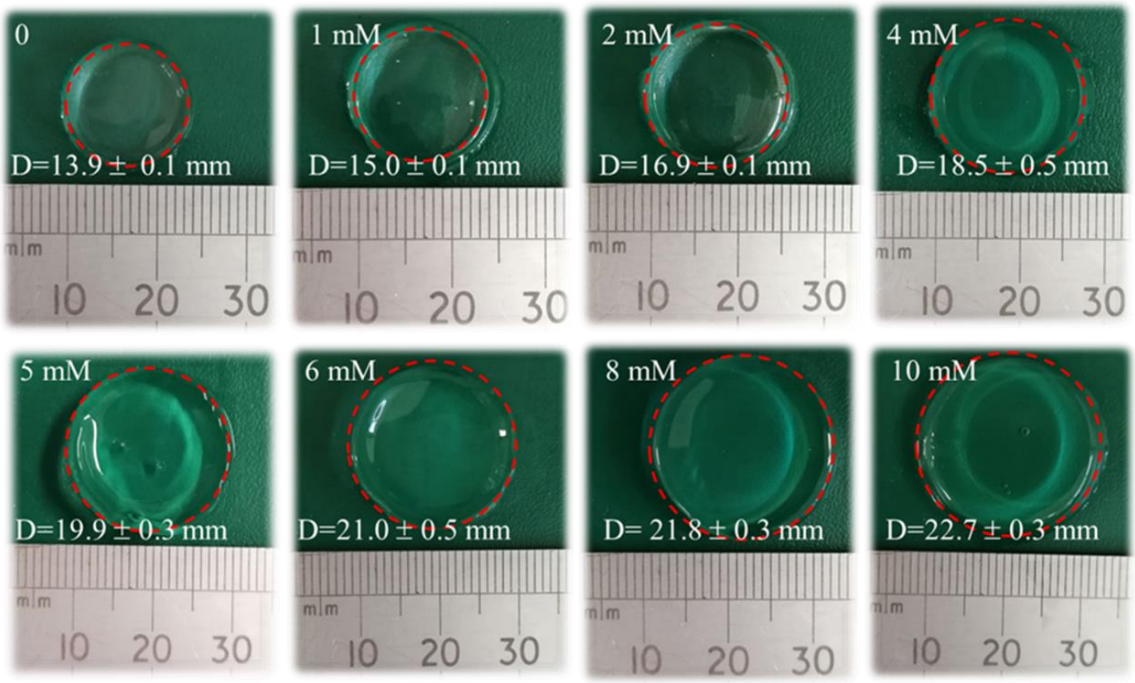

Figure 2.12 C2-20 swelling upon interaction with GSH. The extent of swelling is linked to the GSH concentration in the simulated wound fluid in which the hydrogel was stored. The edges of the three-dimensional hydrogels are circled for clarity.

Figure 2.13 Dissolution of C2-20 after 24-hour immersion in the simulated wound fluid containing 20 mM GSH. The material was too fragile to undergo any form of analysis.

To further probe the suitability of deploying C2-20 as part of a wound management device, the cytotoxicity of the material was assessed using the alamarBlue™ colorimetric assay for cell viability (Figure 2.14). It is essential that a diagnostic material is not detrimental to healthy cells in order to avoid false summations. Additionally, if the hydrogel is intended to be used *in situ* to aid wound healing whilst simultaneously providing diagnostic information, it is essential that the hydrogel promotes fibroblast growth and proliferation over an extended period. Cell viability is positively related to fluorescent intensity in the alamarBlue™ assay. L929 cells grew most rapidly on tissue culture plates (TCPs), in contrast to no cells surviving following culturing on non-treated tissue culture plates (NTCPs). The cells presented excellent proliferation in the presence of C2-20 up to 7 days; a significant increase in cell number was found for each progressive time point. Cell status on TCPs is shown in Figure 2.15, and Figure 2.16 demonstrates cell morphology on C2-20 from day 1 (Figure 2.16a) to day 7 (Figure 2.16d). L929 cells cultured on C2-20 continued to spread and proliferate for the duration of the experiment, confirming the suitability of using C2-20 as a material for wound diagnosis and to aid wound repair.

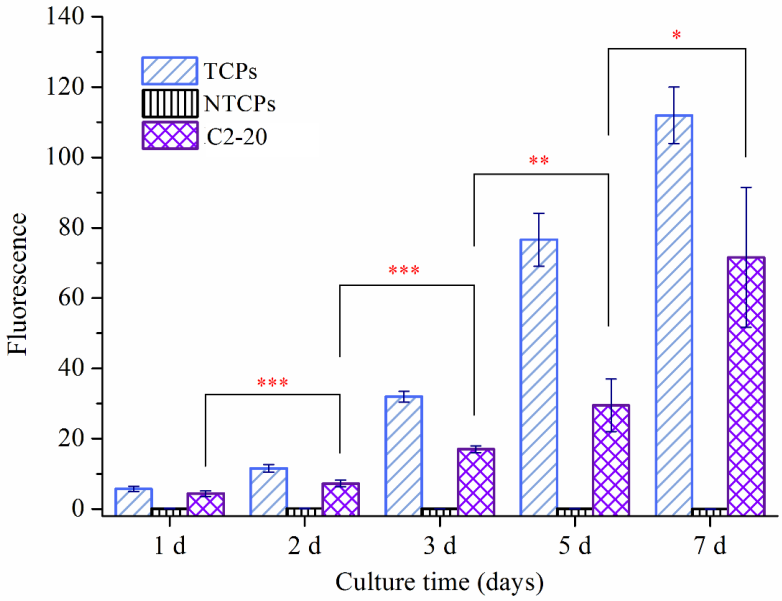

Figure 2.14 L929 cells viability after 7-day culture with hydrogel C2-20, on tissue culture plates (positive control) and non-treated tissue culture plates (negative control).

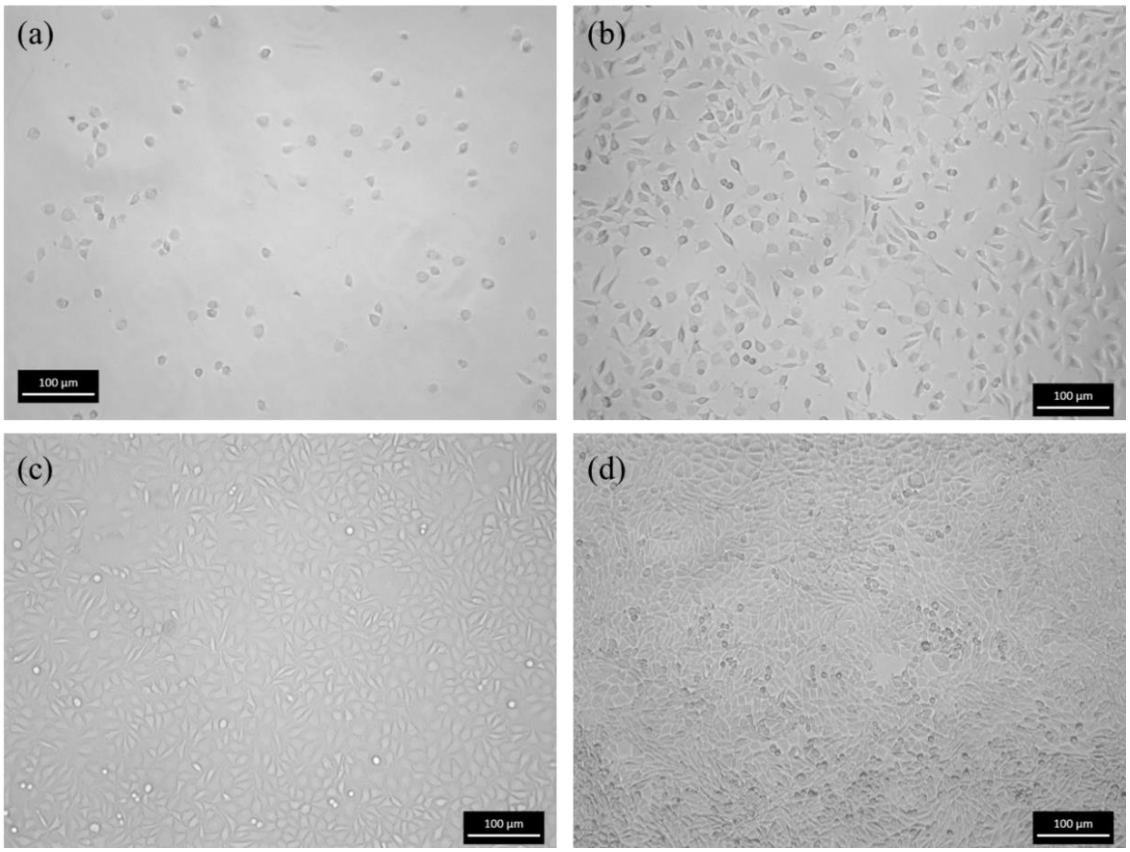

Figure 2.15 Optical microscopy images of L929 fibroblast cells cultured on tissue culture plates for 1 day (a), 3 days (b), 5 days (c) and 7 days (d).

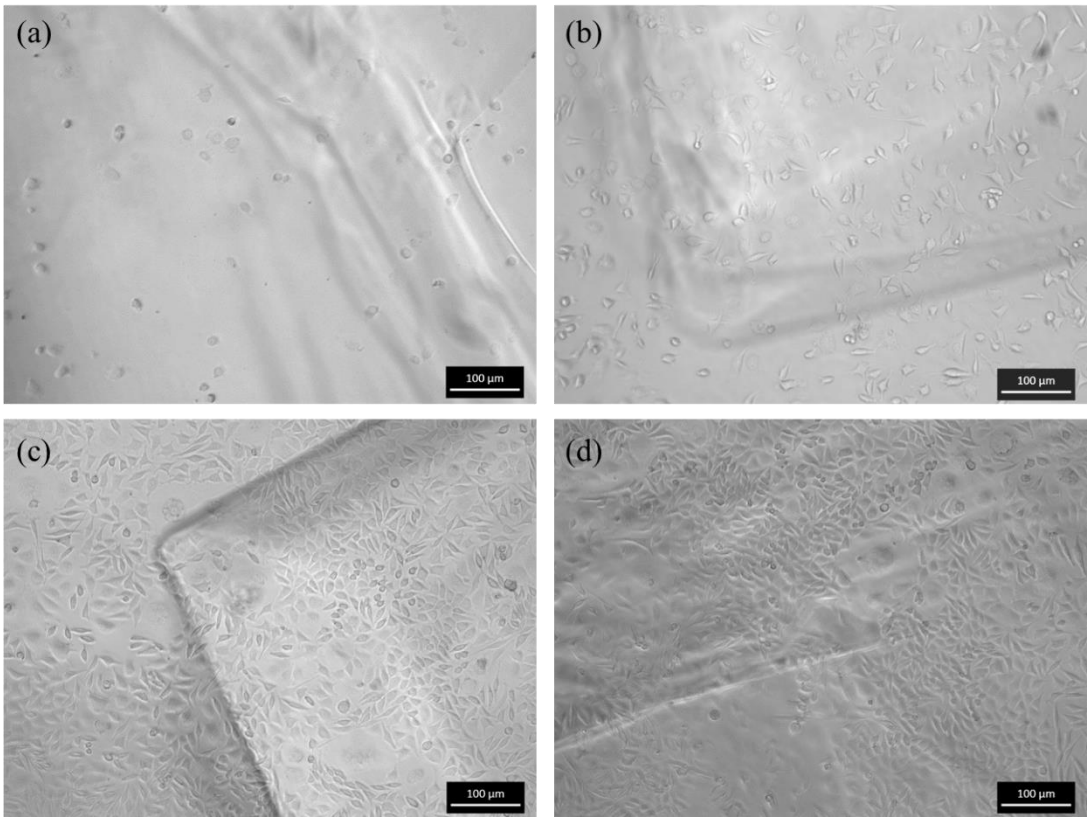

Figure 2.16 Optical microscopy images of L929 fibroblast cells cultured with hydrogel C2-20 for 1 day (a), 3 days (b), 5 days (c) and 7 days (d).

2.4 Conclusion

GSH-responsive, non-cytotoxic, HA-based hydrogels were prepared through the facile crosslinking of HA with cystamine. The hydrogels formed remained robust in aqueous solutions that lacked GSH, but lost structural integrity when incubated in solution that contained GSH. This GSH-induced change altered hydrogel properties both on microscopic and macroscopic levels. The distribution of RITC-dextran within hydrogels that were incubated in the presence of GSH revealed amplified fluorescent probe distribution in correspondence with increased GSH concentrations. Hydrogel crosslinker cleavage by GSH had a sufficiently pronounced effect on the swelling properties of the hydrogel; increased hydrogel swelling upon interaction with GSH-supplemented simulated chronic wound fluid was evident to the naked eye. The hydrogel offers a highly simplistic, label-free,

method to monitor GSH concentration within a sample fluid, and may be used as a support for fibroblast growth and proliferation. Consequently, it is a promising candidate to be used for chronic wound diagnosis and to aid chronic wound repair.

Chapter 3

Hydrogen phosphate-mediated acellular biomineralisation within a dual crosslinked hyaluronic acid hydrogel

- This chapter has been accepted for publication. Reference [Gao, Z., Hassouneh, L., Yang, X., Pang J., Thornton, P.D. and Tronci, G. 2020. Hydrogen phosphate-mediated acellular biomineralisation within a dual crosslinked hyaluronic acid hydrogel. *European Polymer Journal*. (Accepted)]

The creation of hyaluronic acid (HA)-based materials as biomineralisation scaffolds for cost-effective hard tissue regenerative therapies remains a key biomedical challenge. A non-toxic and simple acellular method to generate specific hydrogen phosphate (HPO_4^{2-}) interactions with the polymer network of cystamine crosslinked HA hydrogels is reported (Figure 3.1). Reinforced dual crosslinked hydrogel networks were accomplished after 4-week incubation in disodium phosphate-supplemented solutions that enabled the mineralisation of hydroxyapatite (HAp) crystals across the entire hydrogel structure. HPO_4^{2-}-HA hydrogen bond interactions were confirmed by attenuated total reflectance Fourier transform infrared spectroscopy (ATR-FTIR) and density functional theory (DFT) calculations. HPO_4^{2-}-mediated physical crosslinks proved to serve as a first nucleation step for acellular hydrogel mineralisation in simulated body fluid allowing HAp crystals to be detected by X-ray powder diffraction (2θ = 27°, 33° and 35°) and visualised with density gradient across the entire hydrogel network. On a cellular level, the presence of "*Z*"-shaped aggregated structures proved key to inducing ATDC 5 cell migration whilst no toxic response was observed after 3-week culture. This mild and facile ion-mediated stabilisation of HA-based hydrogels has significant potential for accelerated hard tissue repair *in*

vivo and provides a new perspective in the design of dual crosslinked mechanically-competent hydrogels.

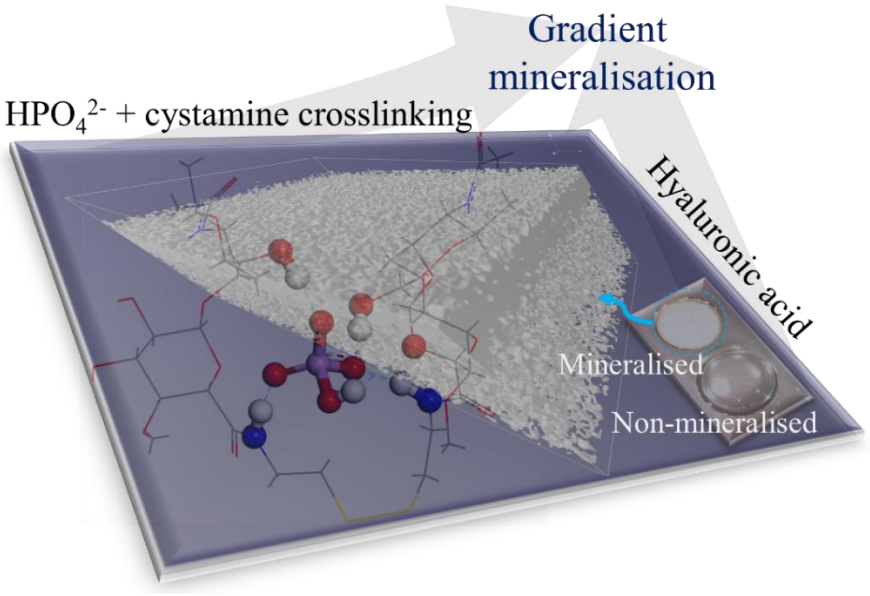

Figure 3.1 Illustration of hydrogen phosphate-mediated acellular biomineralisation within HPO_4^{2-} and cystamine dual crosslinked HA hydrogel.

3.1 Introduction

As the main component of ECM, HA has been applied widely in medicine, for example as a lubricant for osteoarthritis treatment(138-139), wound dressing material to support healing(140) and as post-operation adhesive(141). Recently, HA hydrogels have been applied as implants to support cell growth and aid regeneration of soft tissues including derm,(140) (142) mucosa(141) (143) and tendon(144-145), due to the biocompatibility, biodegradation profile and mechanical properties of HA. The advantageous features of HA in biology, as well as its chemical structure, which can be selectively targeted to fabricate mechanically-competent bioinspired scaffolds, have also been leveraged to support the regeneration of bone. However, this has frequently required either severe or sophisticated synthetic approaches to address the mechanical and composition requirements of bone. Although many methods have been investigated,(146-147) mild non-toxic routes enabling the fabrication of bone-like HA-based architectures have not yet been fully realised.

Ionic interactions, particularly salt effects, enable biomacromolecule cross-linking in a mild manner that avoids chemical synthesis and/or extensive energy radiation.(148-149) The Hofmeister effect details the extent that protein solubility is altered by the presence of different salts in an aqueous environment, and may be used to design protein-based hydrogels with enhanced compressive and tensile properties.(150-151) The mechanism of salt effect in aqueous solutions has been explored in (i) hydration theories, (ii) electrostatic theories, (iii) van der Waals forces, and (iv) internal pressure concepts;(152) however, non-specific ion-mediated interactions may be applied universally in macromolecules.(153-155) Barrett hypothesised that a particular salt could act as either a stabiliser (i.e. kosmotrope) or a destabiliser (i.e. chaotrope) for a specific macromolecule;(156)

for instance, alginate may be particularly well stablised by calcium.(157-159) Therefore, an investigation into whether phosphate groups may be employed for the generation of additional physical crosslinks in a chemically-crosslinked HA hydrogel network was conducted, since phosphate groups are the most common component of buffer salts, and have unique functions in mediating protein denaturation,(160) biomineralisation(161) and the stabilisation of HA-based electrospun fibres(162).

Despite the crucial role of HA and phosphate groups in the ECM of biological tissues and hard tissue repair, only a few systematic studies have been reported concerning phosphate ion interaction with HA-based hydrogels, partially due to the limited control of respective molecular mechanisms and macroscopic effects.(163) Attempts to characterise the interaction between HA and the phosphate head group in phospholipid model membranes have been made through differential scanning calorimetry (DSC), fluorescence spectroscopy, small-angle X-ray scattering (SAXS), infrared spectroscopy (IR) and atomic force microscopy (AFM).(164) However, the resultant phosphate ion-HA interaction was too insignificant to be observed by the above mentioned methods. This underlines the experimental challenge in designing phosphate ion-mediated dual crosslinked HA-based hydrogel systems for the direct build up of bioinspired, mechanically competent HA matrices for hard tissue repair.

Other than phosphate-HA interactions, the integration of hybrid micromorphologies has attracted great interest in bone regeneration, (165) and has been pursued in HA-based hydrogels aiming to realise bioinspired bone-like nanocomposites (147). The *in situ* precipitation of calcium phosphate was reported on the surface of HA hydrogels, yielding a calcium phosphate nanocomposite on the outer layer of the hydrogel scaffold.(146) Ion diffusion

methods have also been studied for mineralisation, including an electrophoresis approach (166) and a double-diffusion system (167). However, only amorphous hydroxyapatite (HAp) was observed in the electrophoresis approach, whereas only calcium phosphate minerals were obtained via the sophisticated double-diffusion system. Consequently, accomplishing time-efficient and controllable formation of HAp crystals with native patterns and growing density is still a great challenge in the design of hierarchical 3-dimensional (3D) structures that mimick human bones.(168)

In this chapter, two hyaluronic acid hydrogels that contained either cystamine or ethylenediamine covalent crosslinks were designed and assessed in a range of salts that partially comprise the Hofmeister series with the aim of developing a simple method to induce dual crosslinking and HAp mineralisation across the hydrogel structure. Hypothesis that non-toxic phosphate-binding sites could be introduced during the crosslinking reaction to further control the swellability and mechanical properties of the HA-based hydrogels and lay down the foundation of a new bioinspired HA-based dual crosslinked structure was set up and investigated in this chapter. Incubation of the hydrogels in aqueous solutions supplemented with hydrogen phosphate (HPO_4^{2-}) generated hydrogen bonds acting as physical crosslinks, thereby yielding a very stable macrostructure with customisable mechanical properties. The mineralisation process of HPO_4^{2-}-conditioned HA hydrogels was monitored in conventional simulated body fluid (c-SBF), whereby unique hierarchical structure and gradients of hydroxyapatite mineral were recorded across the entire hydrogel network and confirmed by X-ray computed microtomography (µCT). The simplicity and mildness of this dual crosslinking and mineralisation approach enables method transferability to other

biopolymers and offer great promise for the creation of bioinspired materials for cost-effective bone regenerative therapies.

3.2 Materials and methods

3.2.1 Materials

HA sodium salt (molecular weight: 1,200 kDa, cosmetic grade) was purchased from Hollyberry Cosmetic, 4-(4,6-dimethoxy-1,3,5-triazin-2-yl)-4-methyl-morpholinium chloride (DMTMM) and 2-(N-morpholino) ethanesulfonic acid (MES) were purchased from Fluorochem. $(NH_4)_2SO_4$, $Na_2HPO_4{\cdot}7H_2O$, tris(hydroxymethyl)aminomethane (TRIS), cystamine dihydrochloride and ninhydrin reagent were purchased from Alfa Aesar. Na_2SO_4, CH_3COONa, $NaHCO_3$, KCl, $K_2HPO_4{\cdot}3H_2O$, $MgCl_2{\cdot}6H_2O$, $CaCl_2$, ethylenediamine was ordered from VWR. 2,4,6-trinitrobenzenesulfonic acid (TNBS), alamarBlue™ assay kit, CellTracker™ Green CMFDA Dye and LIVE/DEAD cell viability kit were purchased from ThermoFisher Scientific. All other reagents were purchased from Sigma-Aldrich.

3.2.2 Hydrogel preparation

HA hydrogels was fabricated in previous method as illustrated in Chapter 2.(169) Briefly, HA powder was dissolved in MES buffer (0.1 M) to obtain a weak acidic (pH=5.5) at room temperature in 2 wt.% concentration. DMTMM (2 equivalents per HA repeat unit) was then added at 37 °C to activate the carboxyl groups of HA. Keep the temperature at 37 °C for 1 hour, and a molar ratio of either 0.4 moles of cystamine or ethylenediamine relative to the moles of each HA repeat unit was added to the solution. The stirring speed was increased to 1000 rpm for 5 minutes and either 0.6 g or 0.8 g of the reacting solution was cast into 24-well plates. HA hydrogels were obtained after 2-hour incubation at 37 °C. Cystamine

crosslinked hyaluronic acid hydrogels were named as C2-40 and ethylenediamine crosslinked hydrogels were abbreviated as E2-40.

3.2.3 TNBS assay to determine the extent of polymer crosslinking

Polymer cross-linking density was investigated using the 2,4,6-trinitrobenzene sulfonic acid (TNBS) assay. 0.8 g of newly-synthesised hydrogel was freeze-dried without the washing step. Each dry network was immersed in 2 mL $NaHCO_3$ solution (4 wt.%) at 40 °C for 30 minutes to remove any unreacted cystamine or ethylenediamine. 1.0 mL of the supernatant was collected and measured by the TNBS assay. 1.0 mL TNBS solution (0.5 wt.% in deionised water) was added to the supernatant in the dark and incubated at 40 °C for 3 hours with a rotation speed of 120 rpm. 3 mL HCl (6 N) was added to the incubated solution and the temperature raised to 60 °C for 1 hour to terminate the reaction. After cooling to room temperature, the sample solutions were diluted with 5 mL of deionised water. The unreacted TNBS was washed out by extraction with 20 mL diethyl ether (×3). 5 mL of the retrieved sample solution was immersed in hot water to evaporate any diethyl ether and diluted with 15 mL of deionised water. Finally, 2 mL of each solution was analysed by UV-Vis spectroscopy at 346 nm. Quantification of any cystamine or ethylenediamine residue was carried out by comparison with a cystamine or ethylenediamine calibration curve.

3.2.4 Hydrogel swelling tests

Various ion-hydrogel interactions were compared through changes in swelling ratios and network degradation. Each replicate of C2-40 and E2-40 hydrogels of known wet weight (ω_0) was individually immersed in either $(NH_4)_2SO_4$, Na_2SO_4, $Na_2HPO_4 \cdot 7H_2O$, CH_3COONa, NaCl or deionised water (50 mL solution). Swelling tests in PBS buffer solution (LONZA) and conventional simulated body fluid (c-

SBF) were also carried out. The wet weight was recorded at different time points (ω_t) up to 4 weeks. All the single-salt solutions used were in 50 mM concentration and replaced by fresh solution every week with the same volume. The c-SBF solution was prepared as reported previously.(170) Briefly, all the salts were added to 960 mL deionised water in the following order: 8.036 g NaCl, 0.352 g $NaHCO_3$, 0.225 g KCl, 0.230 g $K_2HPO_4 \cdot 3H_2O$, 0.311 g $MgCl_2 \cdot 6H_2O$, 40 mL HCl (1.0 M), 0.293 g $CaCl_2$, 0.072 g Na_2SO_4, 6.063 g TRIS. The pH of the solution was adjusted to pH 7.4 by adding HCl (1.0 M).

The swelling ratio was calculated via bellowing Equation 3.1:

$$\boldsymbol{Swelling\ ratio}\ (\%) = \frac{\boldsymbol{\omega_t}}{\boldsymbol{\omega_0}} \times \mathbf{100} \qquad \text{Equation 3.1}$$

3.2.5 Hydrogel compression tests

Hydrogel compression properties were measured using Bose ELF 3200 apparatus with a 0.02 mm/s compressive rate. All replicates were cut into 3 mm diameter cylinders. Compression stress and strain of either initial or salt-treated C2-40 and E2-40 hydrogels were evaluated and compared.

3.2.6 Morphology study of the hydrogel network following salt treatment

Hydrogel morphology was observed using a HITACHI 3400 scanning electron microscope (SEM) under 20 kV voltage with gold coating. All hydrogels were treated with different salts for 4 weeks and flushed with deionised water. SEM analysis was carried out on freeze-dried hydrogel networks. During the course of incubation, the hydrogel structures were also observed by optical microscopy (Zeiss) at different time points after various treatments.

3.2.7 Mechanistic study

HPO_4^{2-} interaction with the hydrogels formed was investigated via attenuated total reflectance Fourier transform infrared spectroscopy (ATR-FTIR, Bruker spectrometer) at room temperature and density functional theory (DFT) calculations. The optimized structures were obtained by DFT calculations at b3lyp/6-31G(d) level carried out using Gaussian 16 program.(171) The binding energy between the HA repeat unit and HPO_4^{2-} was simply calculated as $\Delta E=E_{total}-(E_{HA}+E_{HPO4})$, in which the single point energy was calculated at b3lyp/6-311+G(d,p) level. For display, blue dashed lines indicated the hydrogen bonds, oxygen (O) atoms were depicted in red, nitrogen (N) in blue, sulfur (S) in yellow, carbon (C) in grey, hydrogen (H) in white and phosphorus (P) in pink. All the atoms which were involved in hydrogen bond formation are reported as spheres.

3.2.8 Cell adhesion study during Na_2HPO_4 treatment of C2-40 hydrogels

ATDC 5 chondrocytes (chondrogenic cell line) were used as non-mineralising joint resident cells of the bone-cartilage interface, which normally do not induce mineralization. Initial C2-40 network (0.6 g) was washed by sterile deionised water (×3) and basal cell culture medium (BM) (×3), which was composed of 50 vol.% dulbecco's modified eagle's medium (DMEM, D6546) and 50 vol.% Ham's nutrient mixture F12 (12-615), and supplemented by 5 vol.% fetal calf serum (FCS) and 1 vol.% penicillin and streptomicilin (PS). The final concentration of phosphorus in BM was 0.884 mM. Cells were labelled by Cell Tracker Green (CMFDA) and re-suspended in medium containing 2×10^5 cells/mL. 100 µL cell suspension (2×10^4 cells) was injected on the surface of each hydrogel (n=3). 2 mL of BM was added into each well after 3 hours seeding. Cell attachment and growth was observed and recorded after 48 hours.

To study the influence of Na_2HPO_4 on cell migration, BM was replaced by Na_2HPO_4 treated medium (TM) after 1-week of culture. TM was prepared from

the basal medium, supplemented by sterile $Na_2HPO_4 \cdot 7H_2O$ powder to achieve a final concentration of 1.884 mM (1 mM increase in phosphate, compared with BM). In the control group, the medium was replaced by fresh BM.

Cell attachment and growth were investigated by fluorescence/optical microscope (Zeiss), cell migration was studied via Laser scanning confocal microscopy (LEICA TCS SP8, excitation wavelength 488 nm). All the samples were washed by sterile PBS (×3) to remove any dead cells and impurities before calcein-AM staining.

3.2.9 Acellular mineralisation

After 4-week immersion in Na_2HPO_4 solution (50 mM, 1.0 L, 37 °C), C2-40 hydrogels (n=3) were transferred into deionised water for 24 hours to remove any free phosphate salt, then soaked in 200 mL calcium chloride (10 mM) for another 24 hours.(172) Calcium-treated C2-40 samples were flushed by deionized water to remove any surface salt and subsequently soaked in 1.0 L c-SBF for 2 weeks at 37 °C for mineralisation. The entire process was presented in Figure 3.2. Non-Na_2HPO_4 treated C2-40 samples were immersed in $CaCl_2$ (10 mM, 200 mL) for 24 hours and underwent the same mineralisation operation as a control group.

The mineral structure was confirmed by X-Ray powder diffraction (XRD) at room temperature from 20°-60°. Freeze-dried initial and mineralised C2-40 networks and mineralised C2-40 networks after being burnt at 1000 °C for 30 minutes were measured. The 3D structure of mineralisation was investigated by X-ray computed microtomography (μCT) (Skyscan 1072, Bruker, Kontich, Belgium). Samples were scanned at 100 kVp, 100 mA, and 11.19 μm pixels, with a 1-mm aluminium plus copper filter and a scanning time of around 60 minutes. A reconstruction software program (NRecon; SkyScan) was used to convert the

raw data into bitmap (bmp) files. 3D alignment and registration of samples were done using Data Viewer software (v1.4.3; Bruker microCT). Both CTan and CTvol (v1.10.11.0; Bruker microCT) software were used for the 3D structural analysis.

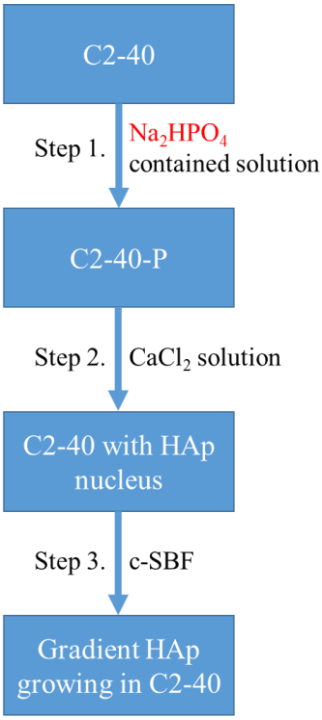

Figure 3.2 Illustration of mineralisation process.

3.2.10 Statistical analysis

For statistical analysis, all the results were analysed with at least three replicates (n≥3). The results are presented as Mean±SD. The significant difference was calculated through One way ANOVA analysis with a p-value at 0.05, which was considered as significant. These were labelled as *p ≤ 0.05, **p ≤ 0.01, ***p ≤ 0.001, ****p ≤ 0.0001.

3.3 Results and discussion

3.3.1 Hydrogel crosslinker density

Two hydrogels were formed, denoted as C2-40 and E2-40, whereby C and E signify HA crosslinking with either cystamine or ethylenediamine, respectively; 2 is the wt.% concentration of HA in the hydrogel-forming solution, whilst 40 is the mol.% of each crosslinker, with respect to HA's carboxylic groups, added during the HA crosslinking reaction. The density of reacted crosslinkers was evaluated by TNBS assay and calculated through ethylenediamine calibration equation: $y=0.0658x-0.0246$, $R^2=0.9743$, y=absorbance, x=ethylenediamine concentration (mM) as presented in Figure 3.3 or cystamine calibration equation: $y=0.0666x-0.0184$, $R^2=0.9933$, y=absorbance, x= cystamine concentration (mM) as evaluated in chapter 2.(169) When adding 40 mol.% of either cystamine or ethylenediamine, approximately 25 mol.% of crosslinker reacted with HA during gel formation (Table 3.1), ensuring that a comparable crosslink density was expected for both hydrogel networks.

Table 3.1 Composition of hyaluronic acid hydrogels formed.

Sample Name	HA quantity (wt.%)	Crosslinker quantity (mol.% of -COOH)	
		Added in	Reacted (Mean±SD)
C2-40	2.0	40.0	25.30±0.85
E2-40	2.0	40.0	25.27±0.01

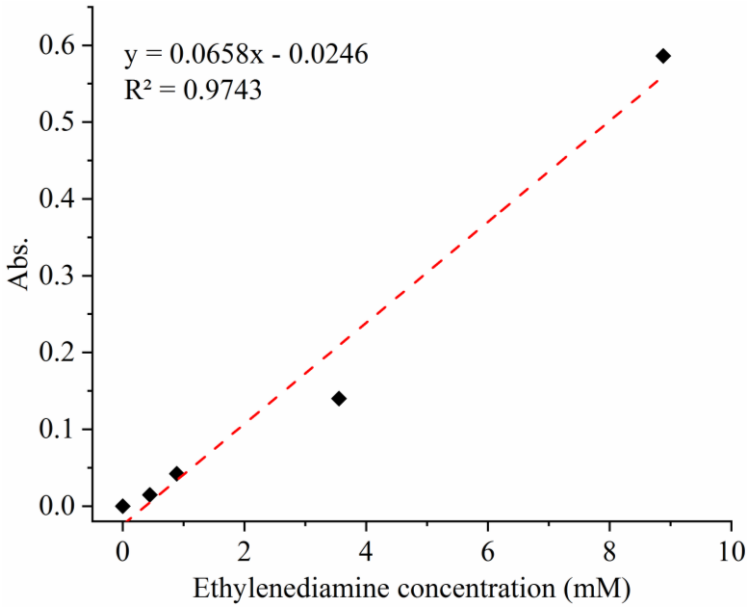

Figure 3.3 TNBS calibration curve of ethylenediamine.

3.3.2 Swelling behaviour of HA hydrogels in salt-supplemented aqueous solutions

Hydrogel swelling equilibrium was reached after 1 day for both C2-40 and E2-40 hydrogels immersed in various solutions (Figure 3.4 a&b). The swelling ratio (SR) of C2-40 samples was found to be in the region of 150 wt.% in all salt solutions, in contrast to a swelling ratio of 425 wt.% in deionised water. The interaction of selected salts with C2-40, which results in decreased hydrogel swelling, followed the order Na_2HPO_4 > $(NH_4)_2SO_4$ = Na_2SO_4 > NaCl > CH_3COONa. For E2-40, lower swelling ratio values (~325 wt.%) were observed in water, compared with hydrogel C2-40, which suggested that cystamine and ethylenediamine had different influence on hydrogel swelling. Anion-HA hydrogel interactions were obvious in the 4-week swelling study and followed the order Na_2SO_4 ≥ $(NH_4)_2SO_4$ > NaCl > CH_3COONa > Na_2HPO_4. When comparing the two hydrogels in salt solutions, the most striking difference is the swelling behaviour in Na_2HPO_4-supplemented solutions. Following incubation of C2-40 in Na_2HPO_4, a significant decrease in the SR was observed from 123±2 wt.% (1 day) to 62±1 wt.% (28

days). In contrast, the SR of E2-40 in Na_2HPO_4 increased from 140±5 wt.% (1 day) to 161±4 wt.% (28 days). This observation was hypothesised to reflect the specific hydrogen bond interaction between HPO_4^{2-} and cystamine-crosslinked HA chains.

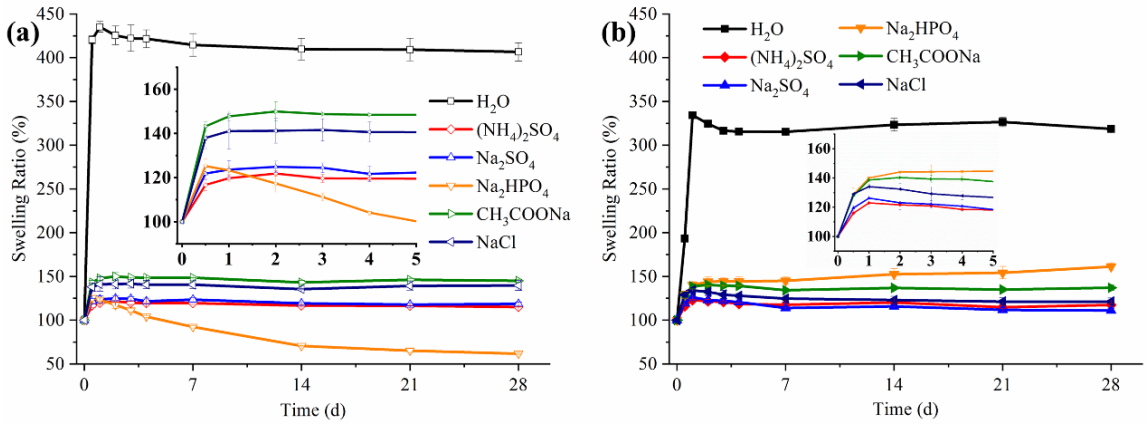

Figure 3.4 Swelling ratio of C2-40 (a) and E2-40 (b) hydrogels in $(NH_4)_2SO_4$, Na_2SO_4, Na_2HPO_4, CH_3COONa, NaCl and deionised water (H_2O). Insert graphs: Time (d) in X-axis and Swelling ratio (%) in Y-axis. All the salt solutions used were in 50 mM concentration and replaced by fresh solution every week with the same volume, the H_2O group was replaced by 50 mL deionised water every week.

As observed in the Na_2HPO_4-supplemented solution, the swelling ratio of samples C2-40 in PBS solution presented a similar decreasing trend over time (SR: 101±3 wt.% (1 day) → 76±2 wt.% (28 days)) (Figure 3.5), supporting the hypothesis that phosphate ions reduce hydrogel swelling. However, the swelling ratio of ethylenediamine crosslinked hydrogel (E2-40) was stable (~120%) for the first 7 days before marginally decreasing over the next 21 days (SR: 119±1 wt.% (7 days) → 114±2 wt.% (28 days)) (Figure 3.5). Based on the significant decrease in SR measured in hydrogel C2-40 following incubation in both Na_2HPO_4 and PBS solution, the swelling ratio was also recorded in conventional simulated body

fluid (c-SBF) to further elucidate any HPO_4^{2-}-mediated interaction with cystamine-crosslinked HA.

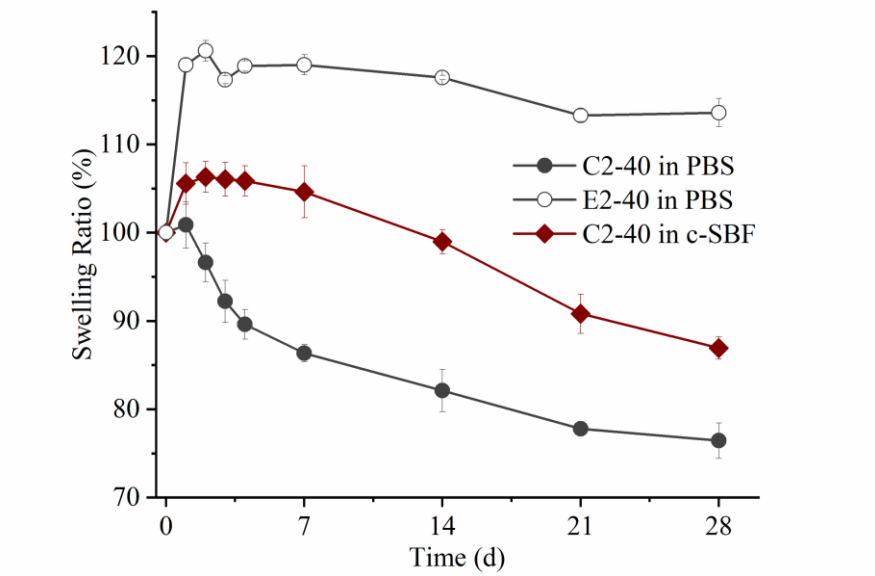

Figure 3.5 Swelling ratio of C2-40 and E2-40 hydrogels in PBS and C2-40 in c-SBF.

As expected, a similar but slower decrease in hydrogel swelling was recorded in c-SBF over time, which is likely due to the different phosphate concentration across the selected solutions (Table 3.2). The significant difference in swelling ratio of hydrogel C2-40 was therefore attributed to the interactions between HPO_4^{2-} ions and cystamine-crosslinked hyaluronic acid, offering a new dimension for adjusting the swelling of the hydrogel by altering the chemical composition of the crosslinker.

Table 3.2 The swelling clarification of C2-40 hydrogels in phosphate-supplemented solutions after 4 weeks.

Solution Name	Phosphorus concentration (mM)	Swelling Ratio (%) Mean±SD
Na_2HPO_4	50	61.69±0.66

PBS	6.658	76.44±2.00
c-SBF	1.001	86.93±1.26

**Concentration of hydrogen phosphate and dihydrogen phosphate.*

3.3.3 Compressive properties of salt-treated hydrogels

Both C2-40 and E2-40 hydrogels were reinforced by ions to some degree, whereby stiffer networks and varying compression strain and stress at break were measured as presented in Figure 3.6 and Figure 3.7, which further proved the effect of salts on hydrogel mechanical properties.

Among the salt-treated samples, the most interesting phenomenon was observed in C2-40 hydrogels in Na_2HPO_4 environment, whereby the lowest value of compression strain at break was recorded after 1 day (77±0.3%) before decreasing to 54±1.5% after 4 weeks treatment. All the other groups formed a relatively stable network (Figure 3.6, b and d). This observation further supported the development of selective, strong HPO_4^{2-}-mediated physical crosslinks in the C2-40 hydrogel following salt treatment, so that the mechanical behaviour of resulting dual crosslinked hydrogel network could be adjusted from elastic to stiff. This variation in mechanical behaviour was also supported by the trends of compression stress at break measured in Na_2HPO_4-treated and water-incubated groups after 1 day and 4 weeks (Figure 3.6, a and c). However, in E2-40 hydrogel groups, no elastic-stiff change was observed in all testing salts solution after 1 day and 4 weeks (Figure 3.7).

The additional interactions between HPO_4^{2-} groups and the cystamine-crosslinked HA network were therefore investigated as a means to induce acellular biomineralisation of cystamine crosslinked HA hydrogel, aiming to develop a cell-friendly design of bioinspired bone-like composites.

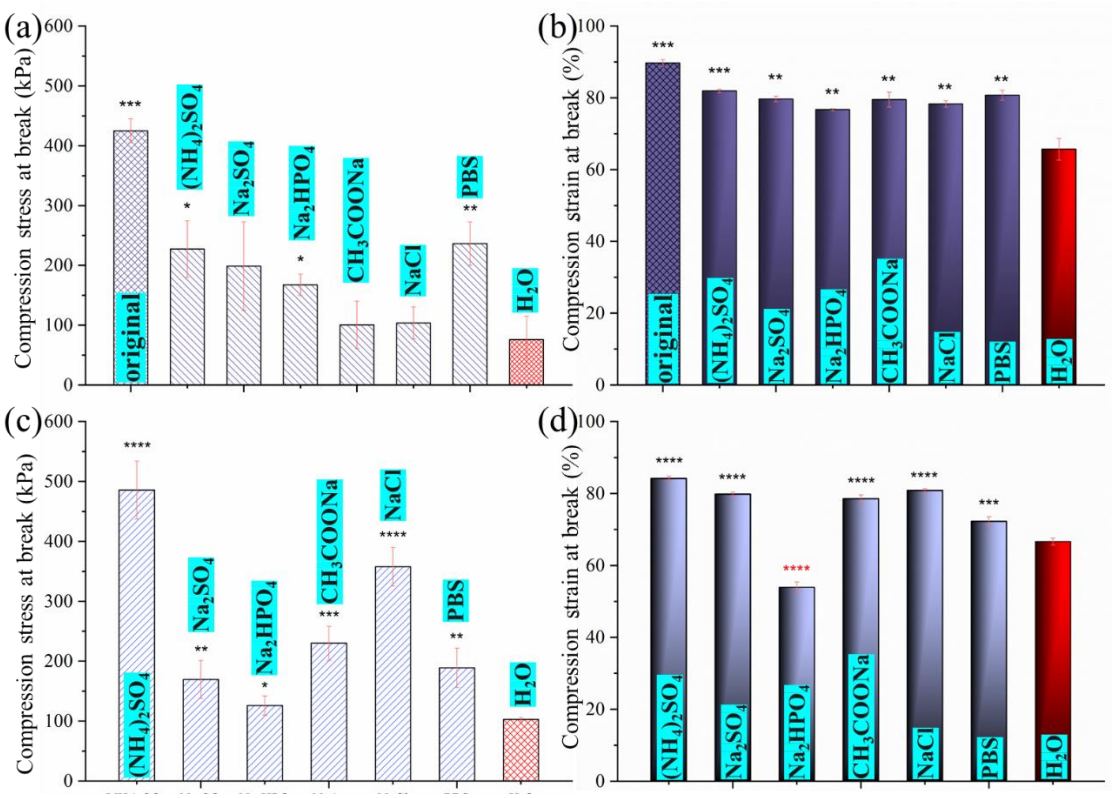

Figure 3.6 Compression measurement of original hydrogel C2-40 and after being immersed in different salt solution, compression stress at break after 1 day (a) and 4 weeks (c), compression strain at break after 1 day (b) and 4 weeks (d). All the statistical analysis was presented after comparison with H_2O group.

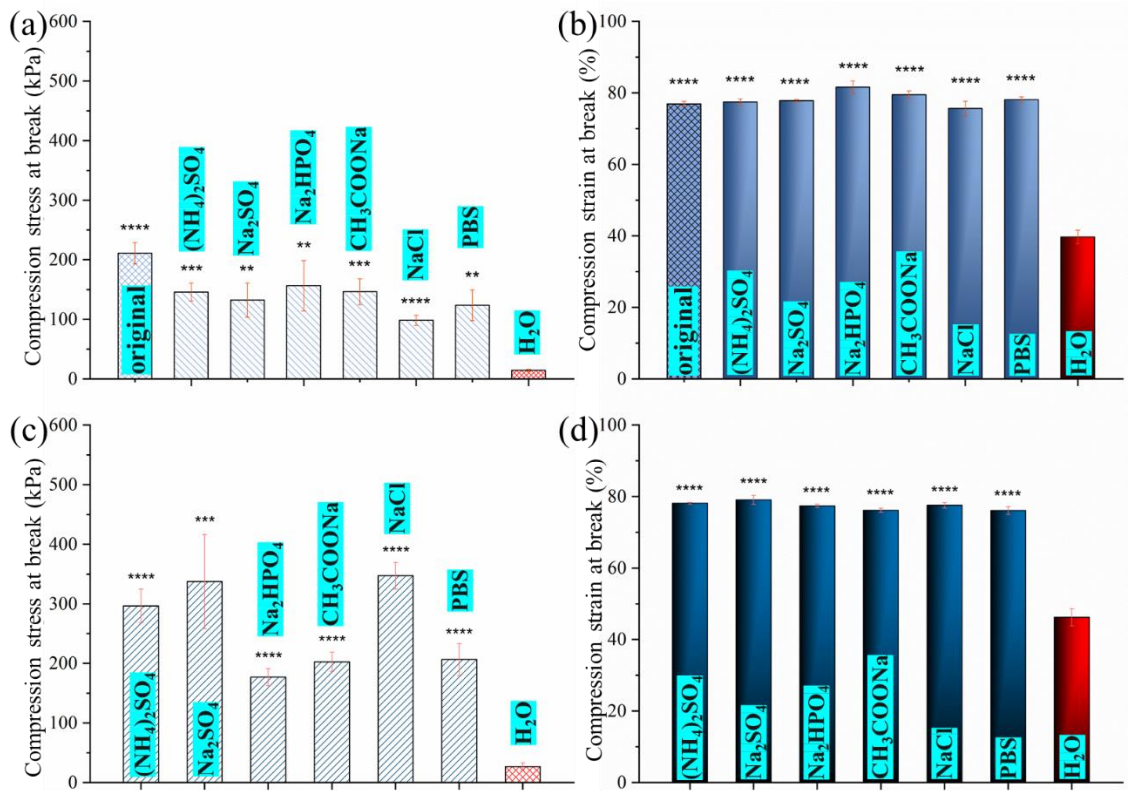

Figure 3.7 Compression measurement of original hydrogel E2-40 and after being immersed in different salt solutions, compression stress at break after 1 day (a) and 4 weeks (c), compression strain at break after 1 day (b) and 4 weeks (d). All the statistical analysis was presented after comparison with H_2O group.

3.3.4 Salt-induced morphology change of HA hydrogels

The surface morphology of freeze-dried hydrogels was investigated by SEM after 4-week immersion in Na_2HPO_4-supplemented solution. Distinguished surface morphology changes were observed in all testing groups, compare with H_2O control group. Crystal-like salts were not observed by SEM in both hydrogel samples (C2-40 in Figure 3.8 and E2-40 in Figure 3.9), suggesting that salts diffused into the hydrogel structure and attached to the network, in agreement with the salt-enhanced compression properties and decreased swelling ratio.

The interesting phenomenon was also shown in the different morphologies between C2-40 and E2-40 after treating by a same salt. For example, in Na_2SO_4 group. The aligned porous structure of C2-40 surfaces (Figure 3.8b), however, did not appear in E2-40 samples (Figure 3.9b). Similar change was also observed in Na_2HPO_4 group, that Na_2HPO_4 stack with C2-40 network (Figure 3.8c), however, formed porous structure with E2-40 (Figure 3.9c). which further supported the hypothesis that HPO_4- has a targetable function to cystamine crosslinked hyaluronic acid hydrogels.

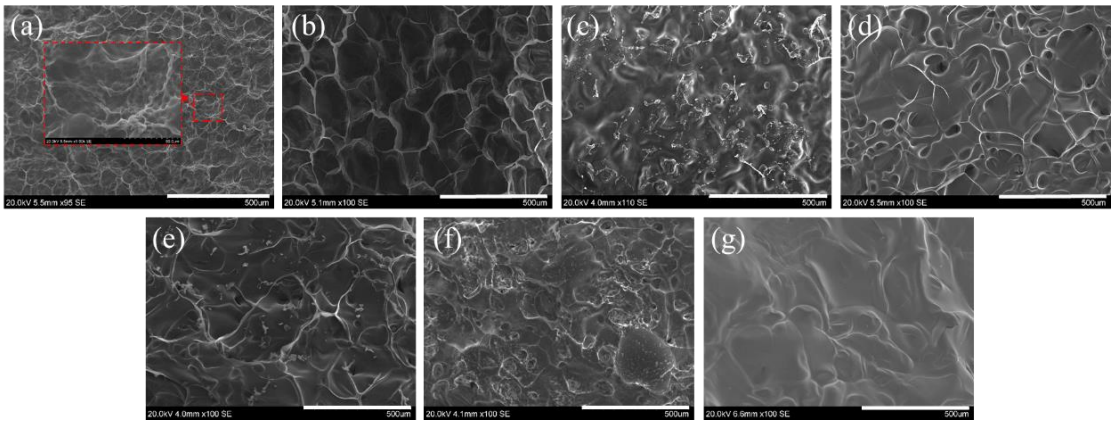

Figure 3.8 SEM images of freeze dried C2-40 hydrogels after being immersed in related solution for 4 weeks. $(NH_4)_2SO_4$ (a), Na_2SO_4 (b), Na_2HPO_4 (c), CH_3COONa (d), NaCl (e), PBS (f), H_2O (g).

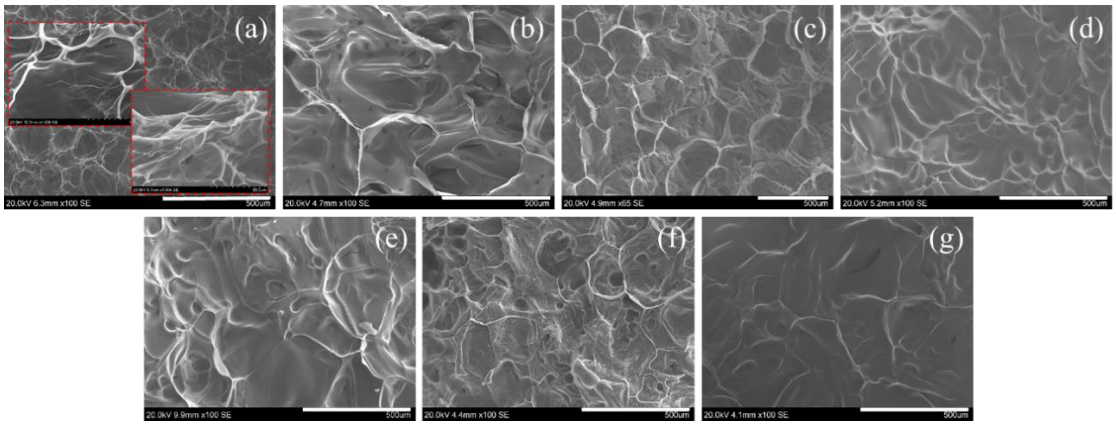

Figure 3.9 SEM images of freeze dried E2-40 hydrogels after being immersed in related solution for 4 weeks. $(NH_4)_2SO_4$ (a), Na_2SO_4 (b), Na_2HPO_4 (c), CH_3COONa (d), NaCl (e), PBS (f), H_2O (g).

To further elucidate the extent of the above-mentioned ion interactions in morphological change, hydrogels were incubated in the presence of Na_2HPO_4 (50 mM), PBS solution and c-SBF for up to three months. Initial HA hydrogels were highly transparent that could not be observed by optical microscopy. However, visible aggregation of the hydrogel surface was observed surprisingly after incubated in HPO_4^{2-}-contained buffer (Figure 3.10), whereby parallel “Z” shape aggregates conjugated with each other in 7-10 μm gaps after Na_2HPO_4 treatment, in addition to lightly conjugated parallel channels with 10-13 μm gaps (Figure 3.10a). Although Z-shaped channels were observed to be more linear in c-SBF (Figure 3.10c), no visible aggregation was seen in hydrogels incubated for three weeks in either deionised water or other HPO_4^{2-} free salt solutions. These results suggest the development of strong interactions between hydrogel C2-40 and HPO_4^{2-} ions as the mechanism behind microscale aggregation on the hydrogel surface. On the other hand, when the incubation time in PBS solution was extended from 3 weeks to 3 months, regular “Z” shapes with 20-30 μm gaps were clearly visible in C2-40 hydrogels (Figure 3.10 d&e). This result is attributed to the slow HPO_4^{2-} interaction in PBS solution with respect to c-SBF, due to the decreased concentration of phosphate ions (Table 3.2). Deep microscale aggregation, rather than surface conjugation, was observed as highlighted by the red arrows. This aggregation mechanism provided the opportunity for creating reinforced dual crosslinked hydrogel networks with adjustable morphologies in near-physiological conditions (as indicated by previous compression tests, Figure 3.6 b&d) and an easy and stable method to build up HPO_4^{2-} sites in the hydrogel for subsequent acellular biomineralisation.

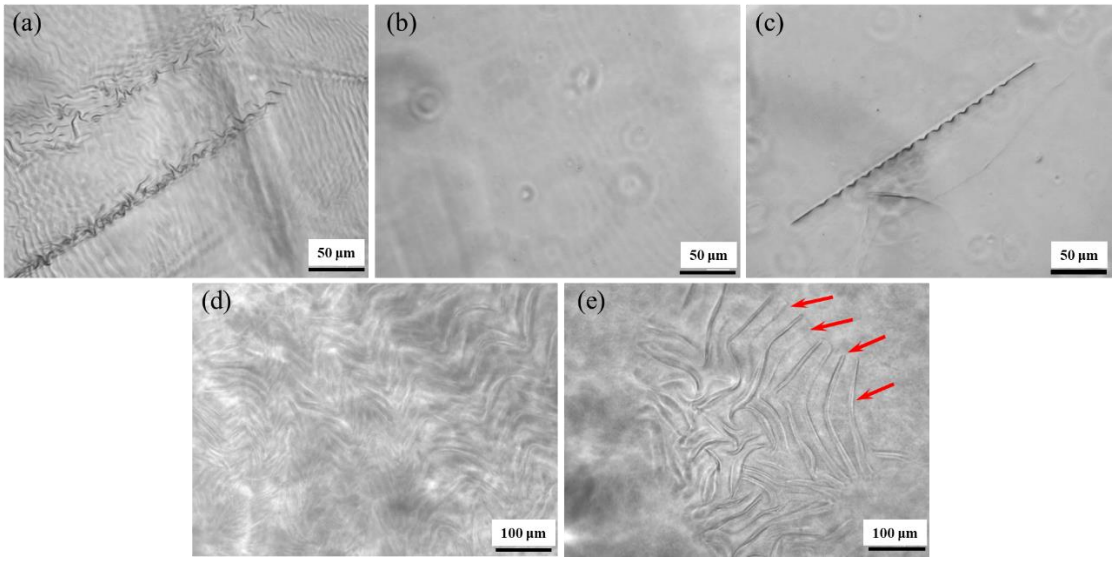

Figure 3.10 Optical images of C2-40 aggregation after being immersed in Na_2HPO_4 (a), PBS (b), c-SBF (c) for 3 weeks, and C2-40 hydrogels after in PBS buffer for 3 months. Aggregation at deeper network was indicated with red arrows.

3.3.5 Mechanism study of HPO_4^{2-} stabilisation

The development of physical crosslinks between HPO_4^{2-} and cystamine-crosslinked hyaluronic acid was further supported by quantum chemistry calculations. Three models of cystamine-crosslinked hyaluronic acid (C-HA) repeat unit were optimised according to their energy minimum configuration (Figure 3.11 a&b). The most stable structure was achieved with the lowest total interaction energy ($\Delta E_{C\text{-}HA3}$=-170.751 kcal/mol) in model C-HA3, where 3 atoms of oxygen (O) in the HPO_4^{2-} species form hydrogen bonds with the NH (1, 5) and OH (2, 3) groups of crosslinked HA, whilst the OH group in HPO_4^{2-} forms hydrogen bonds with the O atom of HA (4). On the other hand, increased total interaction energy were measured with the other two models ($\Delta E_{C\text{-}HA1}$=-162.075 kcal/mol, $\Delta E_{C\text{-}HA2}$=-169.501 kcal/mol), as presented in Figure 3.11.

To investigate the influence of both the disulfide bridge and the number of carbon atoms in the crosslinking chain, the same binding sites as in C-HA were

calculated in HA structure models crosslinked with either 1,6- hexane diamine (6 carbon atoms), butane-1,4-diamine (4 carbon atoms) or ethylenediamine (2 carbon atoms), and abbreviated as H-HA, B-HA, E-HA, respectively (Figure 3.11a).

In the H-HA models, the strongest interaction was obtained in model H-HA3 with a $\Delta E_{H\text{-}HA3}$=-162.149 kcal/mol (Figure 3.11 and Table 3.3), which was 8.602 kcal/mol higher than the one recorded in model C-HA3 ($\Delta E_{C\text{-}HA3}$=-170.751 kcal/mol). Although no direct binding contribution of the S-S bridge was observed, the optimised structure and the reduced binding energy proved an indirect effect. In B-HA models, $\Delta E_{B\text{-}HA3}$=-167.491 kcal/mol was calculated in the most stable configuration, hinting at a lower interaction compared to the 1,6-hexanediamine-crosslinked HA model. Since butane-1,4-diamine is two carbon atoms shorter than 1,6-hexanediamine, the lower interaction measured in model B-HA3 with respect to H-HA3 suggests that the crosslinker length affects the development of HPO_4^{2-}-mediated physical crosslinks in the hyaluronic acid crosslinked chain. This observation is supported by the energy calculations in model E-HA, describing HA chains crosslinked with ethylenediamine as the shortest crosslinker of the three. Only one stabilised structure was obtained with this system, with a final $\Delta E_{E\text{-}HA}$=-155.330 kcal/mol, corresponding to the lowest interaction of all optimised models. Nevertheless, the lack of a stable configuration in the other two models of E-HA is against the development of HPO_4^{2-}-mediated hydrogen bonds in ethylene diamine-crosslinked HA, thereby supporting the role of the crosslinker length in the development of phosphate ion-HA secondary structures.

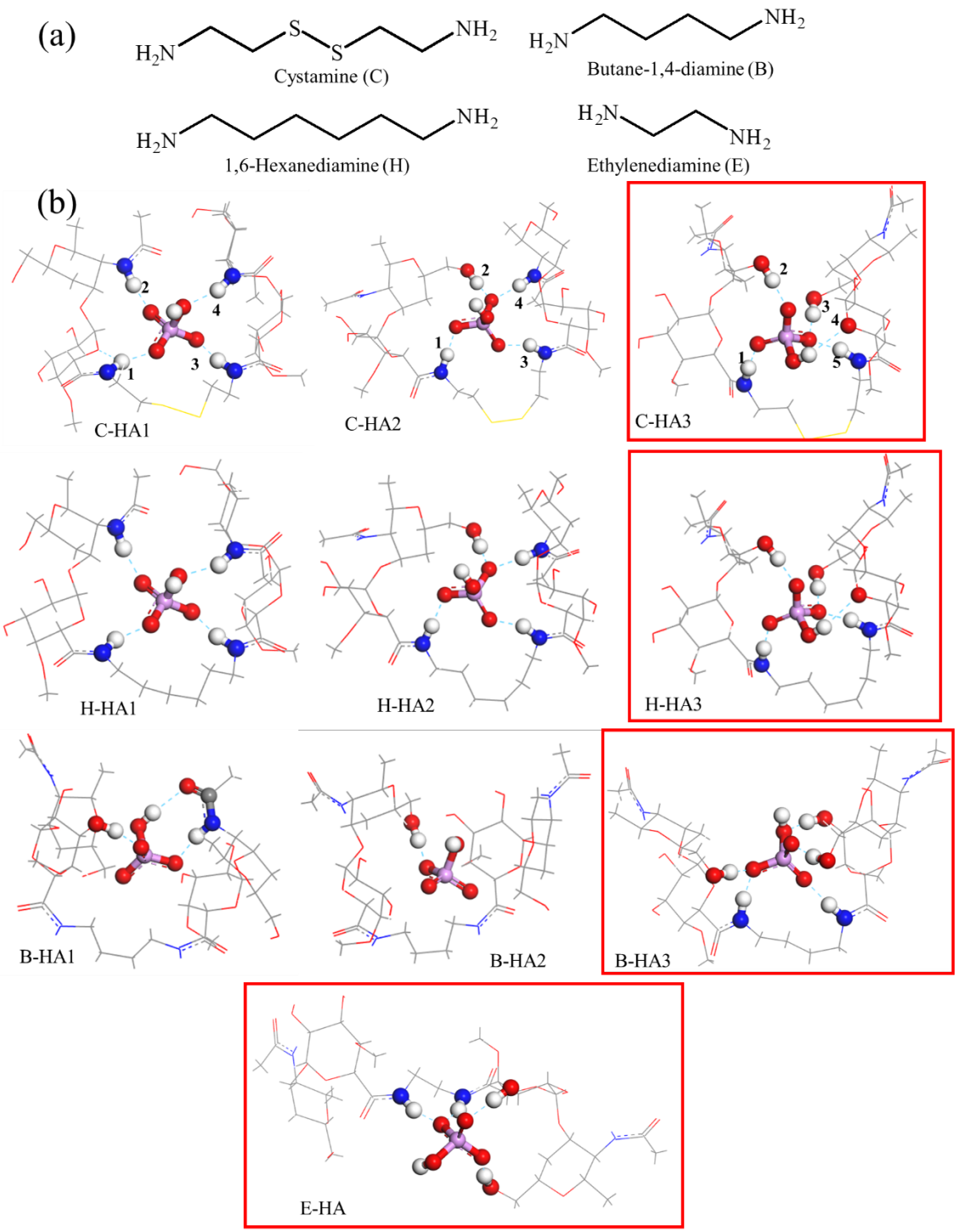

Figure 3.11 Hydrogen phosphate interactions optimised through DFT calculations. Molecular structure of computed crosslinkers (a). Hydrogen bond interaction calculations between HPO_4^{2-} and crosslinked hyaluronic acid repeat unit, crosslinked by cystamine (C-HA), 1,6-hexanediamine (H-HA), butane-1,4-diamine (B-HA) or ethylenediamine (E-HA). The optimised models with lowest interaction energy in each group were in red squares.

Table 3.3 Optimised computing results of interaction energy in different models.

Model Name	ΔE (kcal/mol)
C-HA1	-162.075
C-HA2	-169.501
*C-HA3	-170.751
H-HA1	-152.556
H-HA2	-160.341
*H-HA3	-162.149
B-HA1	-150.107
B-HA2	-146.913
*B-HA3	-167.491
E-HA	-155.330

Experimentally, a band corresponding to a P=O vibration was observed in the IR spectrum after Na_2HPO_4 treatment, with new peaks at 1230 cm^{-1} and 1202 cm^{-1} present in both C2-40 and E2-40 samples, which were initially shown as 1261 cm^{-1} and 1185 cm^{-1} in Na_2HPO_4 (Figure 3.12a). C2-40 and E2-40 hydrogels were

washed with deionised water for 24 hours to remove any free Na_2HPO_4 residue and freeze-dried prior to IR measurement. The existence of a shifted peak related to the P=O vibration provided strong evidence for hydrogen phosphate interaction between P=O and cystamine crosslinked hyaluronic acid units. The most interesting phenomenon was the obvious shift to almost disappearance of the original 1700 cm^{-1} peak (Figure 3.12b) in the IR spectrum of Na_2HPO_4-treated sample C2-40, which is attributed to the amide linkage of HA (position 5 of model C-HA3, Figure 3.11) and which is still clearly visible in the IR spectrum of sample E2-40 following the same salt treatment. The proposed hydrogen bond between the HPO_4^{2-} ion and the nitrogen atom (N) of the amide bond (position 5 of model C-HA3, Figure 3.11) (169) may shift this peak to 1640 cm^{-1}. This result strongly supports the mechanism of multiple hydrogen bonds in cystamine-crosslinked HA chains.

As the most stable interaction was obtained when the phosphate-amide site binding was considered, in agreement with Barrett's work on hyaluronic acid solutions,(156) this research proposed that minimising steric hindrance by adjusting the length of the crosslinker is critical to providing proper access to HPO_4^{2-} ions and enabling coordination and physical crosslinking with amide bonds. Furthermore, the introduction of disulfide bridges in the HA network provided HA crosslinked chains with increased flexibility and increased opportunities for developing secondary interactions with phosphate groups.(173) This potential intermolecular interaction may induce rearrangengement of the disulfide bonds and hydrophilic-hydrophobic sites, so that detectable effects could be observed at the macroscale and on respective material properties as shown in results.

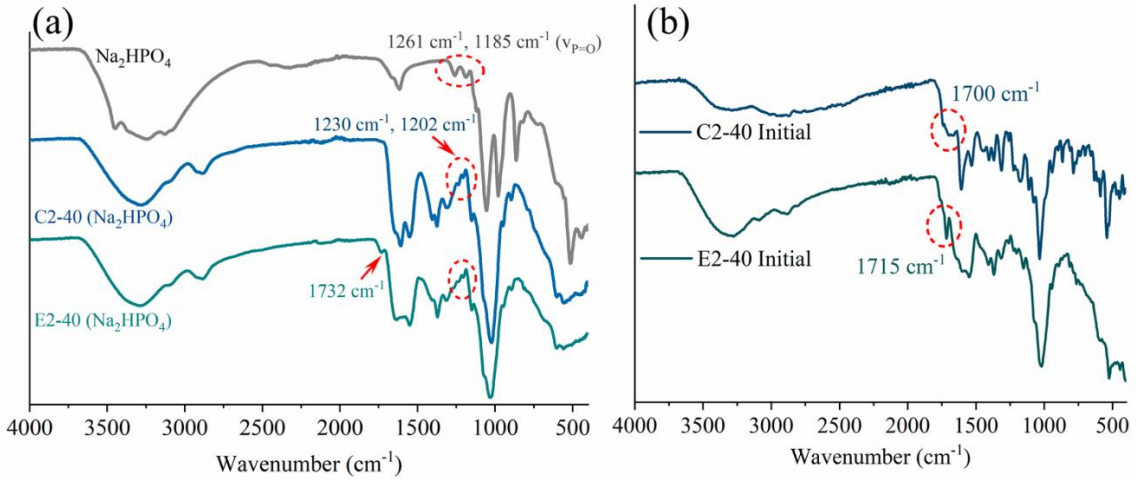

Figure 3.12 (a) IR spectrum of Na_2HPO_4 (top), Na_2HPO_4 treated C2-40 network (middle) and E2-40 network (bottom) for 4 weeks. (b) IR spectrum of initial C2-40 and E2-40 networks without salt treatment.

3.3.6 ATDC 5 cell adhesion study with C2-40 hydrogels during HPO_4^{2-} treatment

Following the results obtained in acellular conditions, a biocompatibility study was carried out with ATDC 5 chondrocytes. Chondrocytes were selected as non-mineralising joint-resident cells, aiming to investigate both the material-induced cell response and any cell culture-induced effect on the material morphology. After 2-day cell culture, some aggregated HA network was already observed on the surface of freshly-synthesised hydrogel C2-40 (Figure 3.13a), in line with the presence of phosphate groups in the cell culture medium (0.844 mM in BM). The aggregation kinetics were accelerated with respect to previously discussed acellular conditions, an observation which can be explained by considering the multiple ingredients in cell culture medium and cell metabolism. At the cellular level, the fluorescent-labelled live cells aligning along the aggregated structure

are visible (Figure 3.13b), whereby the weak fluorescence is likely due to the quenching of the cell-labelling dye following cell growth.

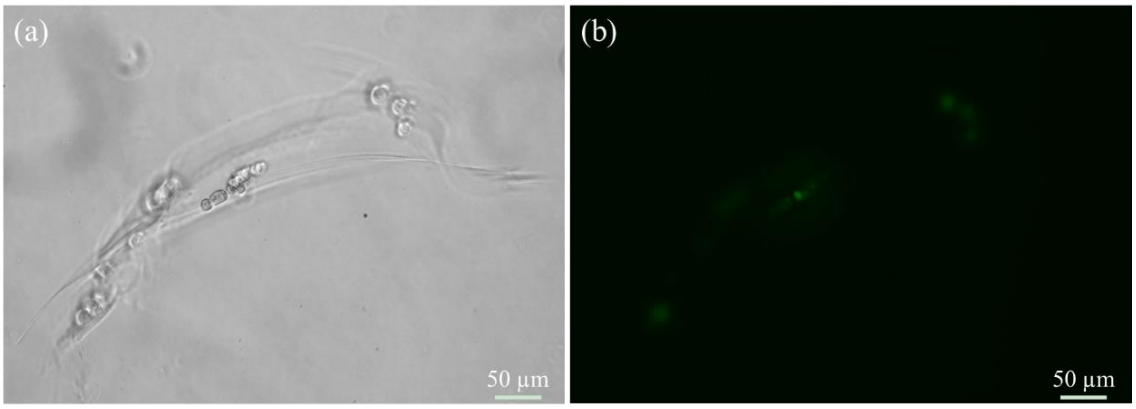

Figure 3.13 Cell Tracker Green labelled ATDC 5 cells on C2-40 surface after 2-day culture in BM, optical image (a) and fluorescent image (b).

After 1-week cell attachment and migration in BM, the conditional cell culture was started with replaced fresh TM (1.884 mM phosphate), control group was replaced by BM (0.884 mM phosphate). The cell culture time was then recounted as “conditional cell culture time”. After another 3 days of cell culture and calcein-AM staining, few fluorescent cells were observed via 3D confocal microscopy in either BM group (a) or TM group (b) (Figure 3.14). To confirm this, C2-40 hydrogels without cells were set as a blank control, whereby only one fluorescent dot with a maximum length of 10 µm was observed in the confocal image (Figure 3.15). This observation is unlikely to be related to living cells and is mostly attributed to impurity or fluorescence from HPO_4^{2-} aggregation, as the cells observed in the hydrogels were approximately 30 µm in length and 10 µm in width (Figure 3.14).

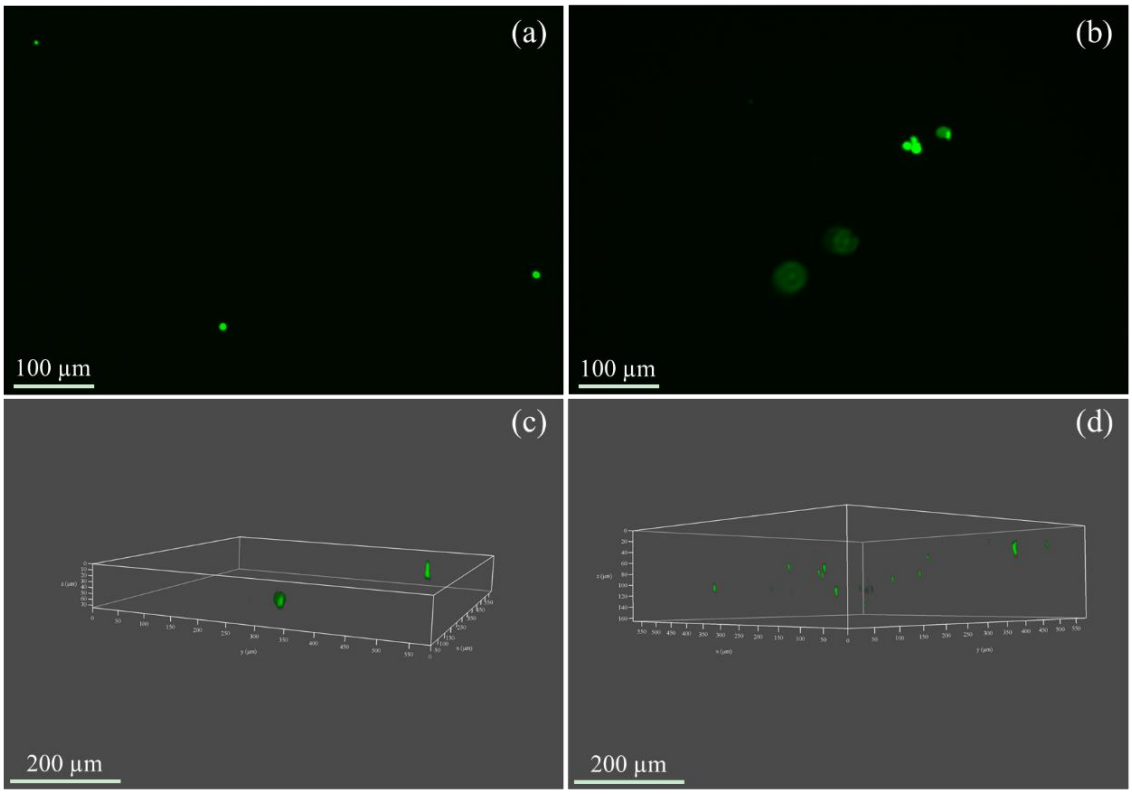

Figure 3.14 After 3-day conditional culture, live ATDC 5 cells were stained via calcein AM and observed by fluorescence microscope, cell migration was investigated by laser confocal microscope. BM (a) and (c), TM (b) and (d).

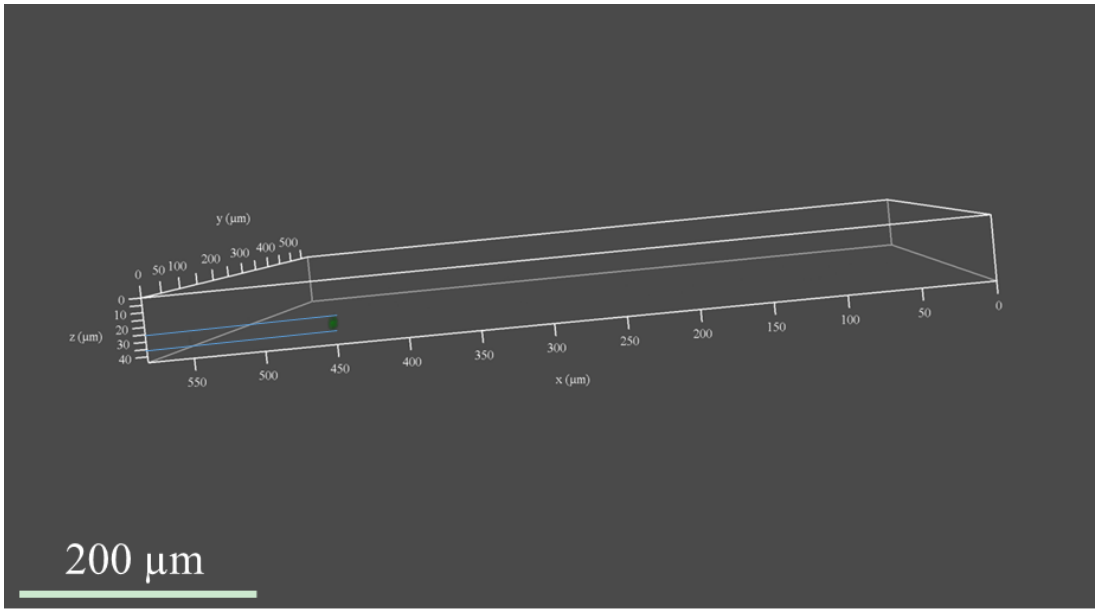

Figure 3.15 After 3-day conditional culture, laser confocal image of blank control C2-40 gel in TM group.

When ATDC 5 cells were independently seeded on the surface of each initial C2-40 hydrogel in both BM and TM, most of the cells were found to adhere to the TCPs (Figure 3.16). Few dead cells were captured, regardless in BM or TM groups. The slightly weaker Live staining (green) in TM group, should be caused by the high cell density, which meant that the Na_2HPO_4 treatment was non-toxic during a 3-week conditional cell culture period and could increase ATDC 5 cells proliferation at some degree (Figure 3.16) after comparing with BM groups.

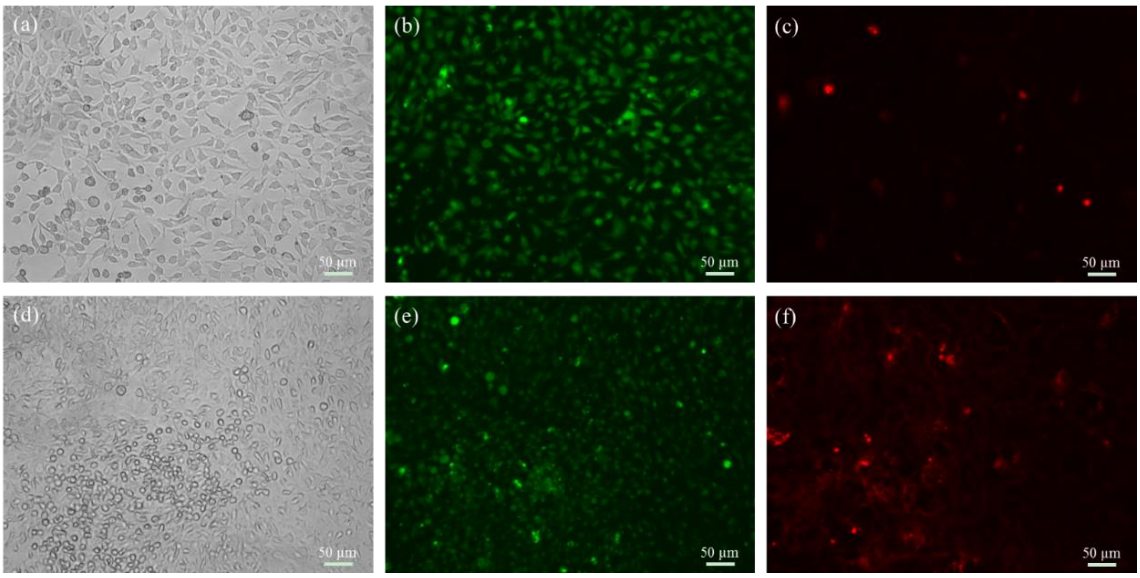

Figure 3.16 ATDC 5 cells growth after 3-week conditional culture on TCPs. Cells were cultured in either BM (a-c) or TM (d-f). Cells were stained via Live (Green) & Dead (Red) marker and observed by optical/fluorescence microscope.

These results demonstrate that the salt-induced hydrogel aggregation process provides a regular channel for cell attachment and growth on the HA hydrogel surface as expected (Figure 3.17). The cell-free formation of previously described salt-mediated microstructures (Figure 3.10) can be proposed as the first stage of the hydrogel biomineralisation process. Although HA hydrogels were known for 3D cell culture as scaffolds, however, no obvious ATDC 5 cells were aggregated in C2-40 hydrogels no matter in BM or TM groups (Figure 3.17).

Here, the absence of cells is key to minimising the risk of cell aggregation on the hydrogel surface as the first step for mineralisation, which could otherwise induce steric effects, cause local tissue inflammation and delay HAp crystallisation for bone regeneration in hydrogel networks.

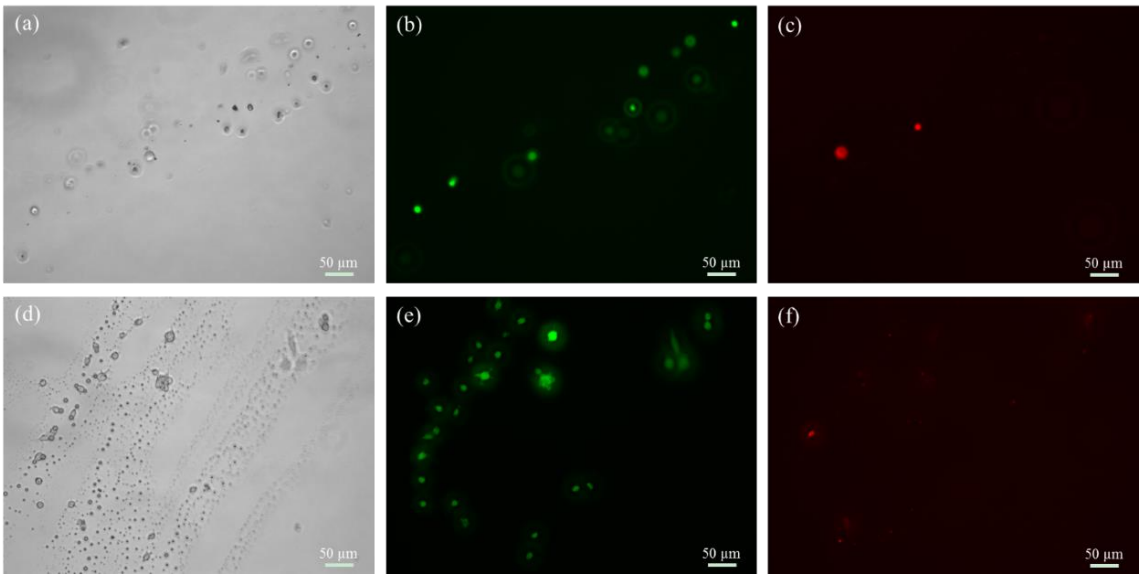

Figure 3.17 ATDC 5 cells growth after 3-week conditional culture on C2-40 hydrogels. Cells were cultured in either BM (a-c) or TM (d-f). Cells were stained via Live (Green) & Dead (Red) marker and observed by optical/fluorescence microscope.

3.3.7 HAp growth characterisation within HPO_4^{2-}-treated HA-based hydrogels

Both Na_2HPO_4 and non-Na_2HPO_4-treated C2-40 replicates were transferred into deionised water for 24 hours to remove any free salt, and then further treated with 200 mL $CaCl_2$ (10 mM) for 24 hours. The calcium concentration was chosen from a study on milk as one of the main sources for calcium supplementation.(172) All the samples were flushed with deionised water before the mineralisation process, which was subsequently carried out in c-SBF (1.0 L) at 37 °C for 2 weeks. Remarkably, a homogeneous HAp phase formed in the C2-40 hyaluronic acid

network (Figure 3.18a, left), with full mineralisation observed across the whole hydrogel structure (Figure 3.19). No visible mineral was observed in the control group without HPO_4^{2-} treatment, ensuring that the hydrogel surface remained transparent (Figure 3.18a, right). To further characterise the mineralised structure of Na_2HPO_4-conditioned hydrogel, XRD analysis was carried out (Figure 3.18b). A clear stacking structure corresponding to HAp was observed after heating the sample at 1000 °C for 30 minutes. Some diffraction was recorded for the freeze-dried network at 2θ = 27°, 33° and 35°, again corresponding to the HAp phase,(174) whilst no peak was observed in the initial freeze-dried C2-40 hydrogel network.

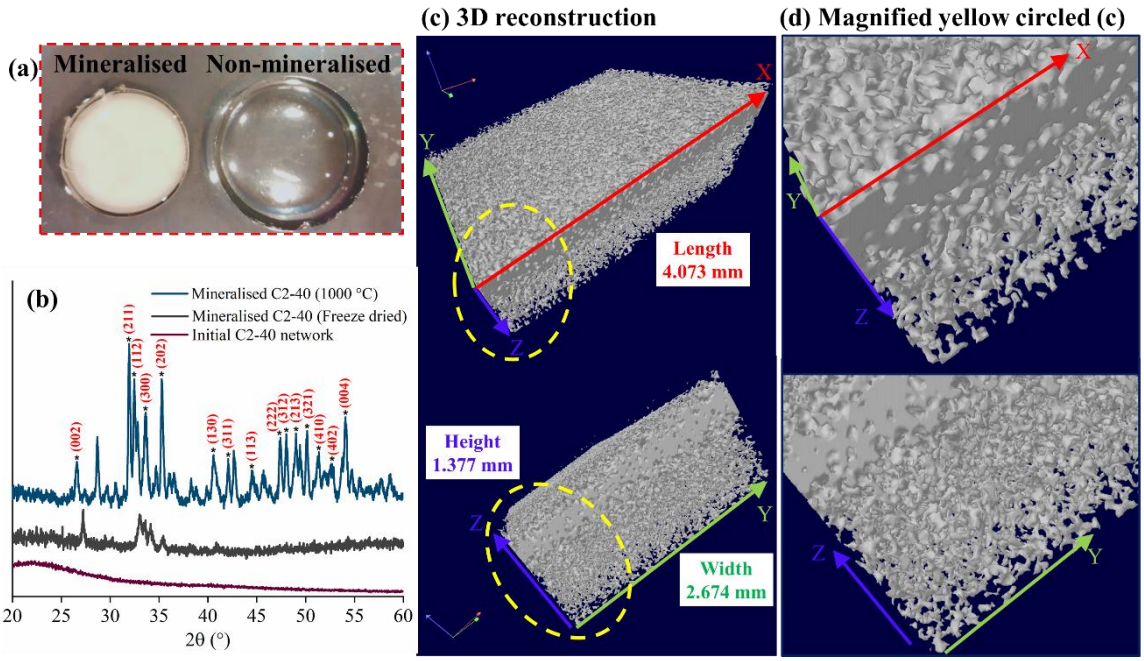

Figure 3.18 Optical images of wet mineralised C2-40 hydrogels and non-mineralised C2-40 control after HPO_4^{2-} treatment (a). XRD results of mineralised C2-40 (b), after 1000 °C burning (top), freeze-dried mineralised network (middle), initial freeze-dried C2-40 network (bottom). 3D reconstruction of mineralised C2-40 after µCT scanning (c), Length-Height direction (top), Height-Width direction (bottom). The presented images were minerals inside C2-40 at wet status, HA network of C2-40 was invisible in µCT scanning.

Figure 3.19 Optical images of the wet mineralised sample C2-40 after HPO_4^{2-} treatment (side view, left) and C2-40 control (top surface, right).

In addition to XRD spectra and digital macrographs, µCT was carried out as a non-damaging technique to visualise the 3D macrostructure of the mineralised C2-40 composite obtained following 2-week incubation in c-SBF (Figure 3.18).The cross-sectional image in Figure 3.20 clearly reveals the gradient decreasing HAp density along with Z-axis direction, in agreement with the results obtained from the µCT 3D reconstructed models (Figure 3.18 c and d). Mineral growth with remarkable growing density was successfully achieved after Na_2HPO_4 hydrogel treatment, rather than ion distribution surrounding the gel surface or limited formation of mineral particles.(146) (166) This result demonstrates the high potential of the HAp-mineralised C2-40 hydrogel as a scaffold for hard tissue repair, particularly as gradient hydrogels for tissue regeneration.(175)

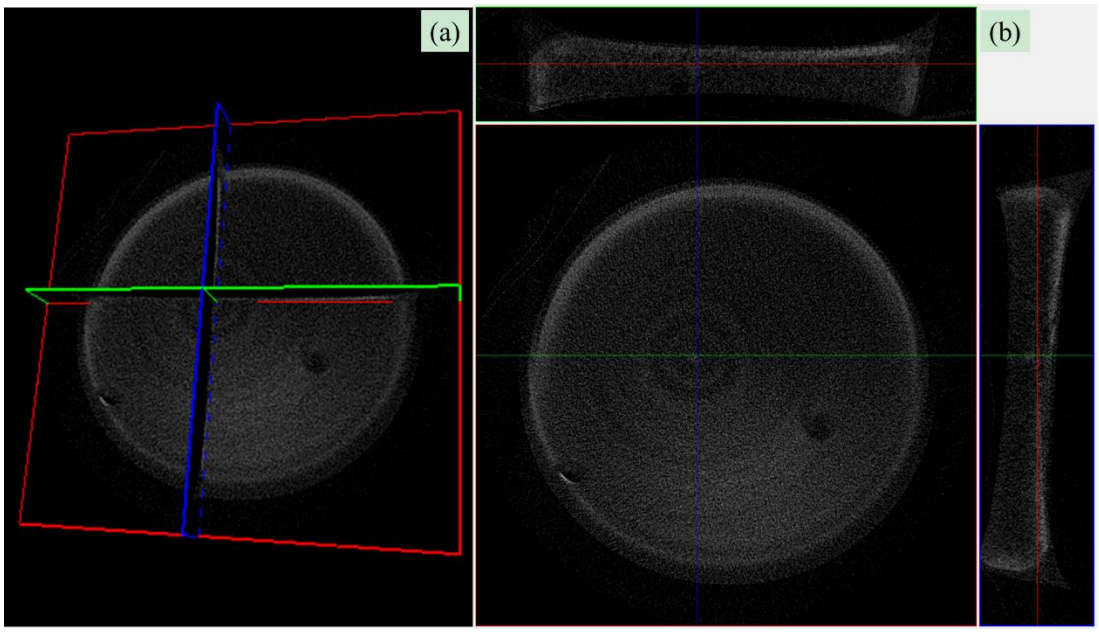

Figure 3.20 Macro-pattern study of mineralised C2-40 from µCT scan, combined 3-dimension image (a), cross section of each axis (b).

3.4 Conclusion

The effect of the inclusion of a range of salts within cystamine and ethylenediamine-crosslinked HA-based hydrogels was investigated as an acellular route to realise dual crosslinked bioinspired bone-like nanocomposites. Specific and strong hydrogen bond interactions acting as physical crosslinks were first discovered between cystamine-crosslinked HA chains and HPO_4^{2-} groups, as indicated by the decreased swelling and decreased compression at break, IR spectroscopy and DFT calculations. The introduction of phosphorus nuclei was key to enable this interaction, which was successfully leveraged to accomplish HAp growth across the hydrogel structure. Gradient HAp was obtained and visualised by μCT 3D reconstruction after hydrogel incubation in 1.0 L conventional simulated body fluid for 2 weeks. A novel acellular method to generate 3-dimensionally dual crosslinked and mineralised structures is developed that has great appeal for hard tissue repair.

Chapter 4

The Facile and Additive-Free Synthesis of a cell-friendly Iron(III)-Glutathione Complex

- This chapter has been published. Reference [Gao, Z., Carames-mendez, P., Xia, D., Pask, C.M., Mcgowan, P.C., Bingham, P.A., Scrimshire, A., Tronci, G. and Thornton, P.D. 2020. The facile and additive-free synthesis of a cell-friendly iron(III)–glutathione complex. *Dalton Transactions*. **49**, pp. 10574-10579.]

The straightforward creation of an unreported glutathione-stabilised iron(III) complex is reported. In contrast to previous reports, glutathione was shown to coordinate and stabilise iron directly under physiological conditions in the absence of additional sulfur containing molecules, such as sodium sulfide. The complex was extensively characterised; the molecular geometry was determined as two inequivalent octahedra, approximately 2/3 of which is slightly distorted towards more tetrahedral in character, with the remaining 1/3 more regularly octahedral. The dispersion of the iron(III)-glutathione complex in aqueous solution yielded particles of 255±4 nm in diameter that enhanced the growth and proliferation of L929 fibroblast cells over 7 days, and inhibited the activity of matrix metalloproteinase-13. Consequently, the unprecedented glutathione-stabilised iron(III) complex disclosed has potential use as a simple-to-prepare growth factor for inclusion within cell culture media, and is an excellent candidate as a therapeutic for the treatment of metalloproteinase-13-associated diseases. Illustrated in Figure 4.1.

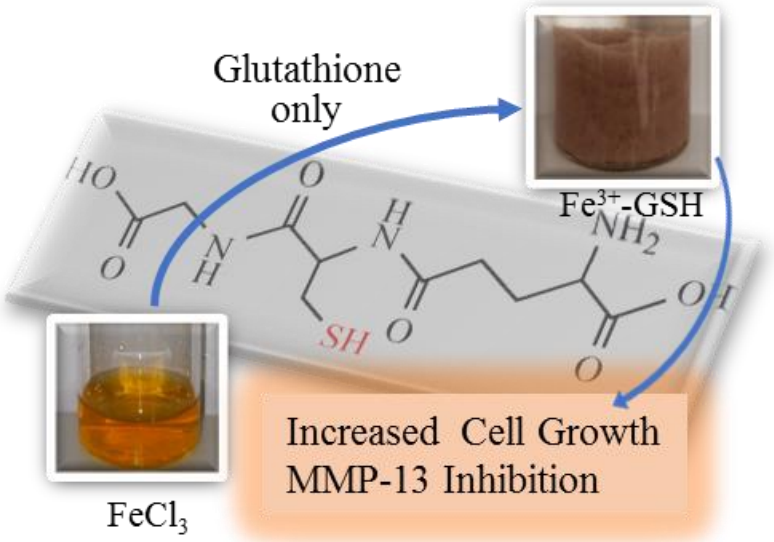

Figure 4.1 Illustration of Iron(III)-Glutathione formation and functions.

4.1 Introduction

GSH, (structure was presented in Figure 2.2 in page 33) is imperative for cellular defence against reactive oxygen species that cause apoptosis and tissue inflammation.(176) Free radicals and reactive oxygen species are deactivated by the sulfhydryl moiety that the tripeptide presents, undergoing conversion to stable and innocuous compounds. Numerous disease states are linked to GSH deficiency in cells, including chronic hypertension,(177) pulmonary fibrosis,(178) human immunodeficiency virus-related disease,(179) and respiratory distress syndrome.(180) GSH is administered as an oral supplement, however the half-life of GSH within the blood plasma (t = 1.6 min) ensures that a significant proportion of the supplement is oxidized prior to reaching the gastrointestinal tract.(181) Consequently, alternative cell-friendly methods of GSH storage and localized delivery, or reversible GSH modification, are required to elevate depleted tissue GSH levels.

Transition metal ions perform a number of cellular functions within eukaryotes, including photosynthesis and respiration.(182) Metalloproteins, which contain a metal ion cofactor, play a vital role in the storage and transport of enzymes and signal transduction proteins, and make-up a third of proteins within the human body.(183) Iron is the most abundant redox-active metal within the body owing to its presence within haemoglobin. The natural presence of haemoglobin *in vivo* provides great encouragement for the formation of iron-protein and iron-peptide complexes as materials that are suitable to be deployed within living organisms.

Complexes that contain redox-active metal centres may be exploited as therapeutics and diagnostic tools.(184) Notably, such organometallic materials have been proposed as contrast agents in which the variety of oxidation states that the redox-active metal can adopt is associated with distinct paramagnetic

properties that enable their effective detection *in vivo*.(185) Iron has potential for use within a contrast agent composition due to its capability to form high-spin Fe^{3+} complexes. Wang *et al*. recently reported biochemically responsive Fe^{2+}-PyC3A complexes that, upon oxidation by reactive oxygen species, form Fe^{3+}-PyC3A that enable contrast enhancement within inflamed pancreatic tissue.(186) Within healthy tissue, Fe^{2+}-PyC3A is maintained and so signal enhancement does not occur.

GSH has been reported to form stable complexes with transition metals including mercury,(187) silver,(188) cadmium,(189) and zinc.(190) Consequently, it has been cited as a candidate for metal speciation in aqueous environments for the detection and remedy of heavy metal pollution.(191) However, the formation of hydrolytically-stable iron-GSH complexes is more limited, especially in a cluster-free configuration. Qi *et al*. reported that glutathione-complexed clusters [2Fe-2S] are stabilised by glutathione aggregates that form intermolecular salt bridges and hydrogen bonds, providing a stable binding pocket for the [2Fe-2S] cluster core.(192-193) However, despite these advances, the binding of glutathione to ferrous iron in the absence of iron-sulfur cluster formation has not been reported due to the rapid reduction of Fe^{3+} in the presence of GSH.(194-195) In this case, a complex that contains GSH ligands, but lacks [Fe_2S_2] bridged dimers, is anticipated to form.

This chapter reports the formation of a Fe^{3+}-GSH complex by combining equimolar quantities of GSH and $FeCl_3$. Additives that promote iron-sulfur cluster formation, for instance sodium sulfide, were not included in the synthesis. Analysis reveals that reduced GSH forms a complex with Fe^{3+}, yielding a stable complex suitable for extensive characterisation. Notably, the Fe^{3+}-GSH complex possessed excellent cell compatibility, promoting the growth and proliferation of

L929 fibroblast cells over seven days *in vitro*. Consequently, it is highly promising as a drug-free approach to enhance fibroblast growth in vitro within cell culture medium at low concentrations (< 0.5 mg/mL), and as a constituent to restore homeostasis in chronic tissue states.

4.2 Materials and methods

4.2.1 Materials

Iron(III) chloride hexahydrate and Iron(II) chloride tetrahydrate were purchased from Sigma-Aldrich, L-glutathione (reduced) was purchased from Alfa Aesar, L-glutathione oxidised (GSSG) was purchased from BioSci. alamarBlue™ Assay kit was purchased from ThermoFisher Scientific.

4.2.2 Fe^{3+}-GSH complex preparation

123 mg (0.4 millimoles) of GSH was added to 4 mL $FeCl_3$ solution (0.1 M), and the mixture was mildly agitated by vortex mixing for 2 min. Then, the complex was precipitated in 40 mL ethanol. The products were collected by centrifugation at 10,000 rpm for 15 min. The Fe^{3+}-GSH complex produced was washed three times with ethanol and dried at 37 °C.

To determine the effect that GSH in its oxidised form (GSSG) has on the oxidation state of Fe, and if it can act as a chelating agent with Fe, 123 mg (0.2 millimoles) of GSSG were added to 4 mL $FeCl_2$ solution (0.1 M). Agitation in ethanol, and product precipitation, collection and drying were performed similar to the previous complex formation with GSH.

4.2.3 Fe^{3+}-GSH complex structure analysis

The coordination between Fe^{3+} and GSH was confirmed by UV-Vis spectroscopy. Various amounts of GSH solution (0.1 M) were independently added to 600 µL

$FeCl_3$ (0.1 M) at different molar ratios. Deionised water was then added to dilute the complex solution to a final concentration of 40 mM $FeCl_3$. Absorbance was measured with baseline correction at 690 nm, at which point no components of the solution absorb significantly. Nine different molar ratios of Fe:GSH between 6:1 and 1:1.5 were assessed.

The structure of the Fe^{3+}-GSH complex was assessed by fluorescence spectroscopy (FS). 1.0 mg/mL Fe^{3+}-GSH suspension was prepared via ultrasonic agitation for 10 min to achieve a homogeneous H_2O dispersion. 2 mL of each dispersion was used for FS analysis at room temperature, using an excitation wavelength of 408 nm. The blank and control spectra were carried out using 0.1 M $FeCl_3$, 0.1 M GSH and a $FeCl_3$-GSH mixture (1.2:1, 1:1 and 1:1.2 molar ratio) with consistent $FeCl_3$ concentration.

^{57}Fe Mössbauer spectroscopy was applied to confirm the Fe^{3+}-GSH configuration and iron valence. Measurements were carried out using acrylic absorber discs (area 1.767 cm^2) loaded with sample to achieve a Mössbauer thickness of 1. The 14.4 keV γ-rays were supplied by the cascade decay of 25 mCi ^{57}Co in Rh matrix source, oscillated at constant acceleration by a SeeCo W304 drive unit, detected using a SeeCo 45431 Kr proportional counter operating with 1.745 kV bias voltage applied to the cathode. All measurements were carried out at room temperature over a velocity range of ±4 mm s^{-1}, and were calibrated relative to α-Fe foil. Spectral data were fitted using the Recoil software package, using Lorentzian line shapes. Proton nuclear magnetic resonance spectroscopy (^1H NMR, Bruker AV400, 400 MHz) was carried out on Fe^{3+}-GSH solution (D_2O) to investigate the coordination between Fe and GSH. For further structural information, attenuated total reflectance Fourier transform infrared (ATR-FTIR, Bruker) spectroscopy was used to analyse dried Fe^{3+}-GSH powder between 400-

4000 cm^{-1}. Circular dichroism (CD) spectroscopy was applied to investigate the chirality change from GSH to Fe^{3+}-GSH complex. CD spectra was carried with a bandwidth of 2.0 nm between 250-750 nm.

Proton nuclear magnetic resonance spectroscopy (^1H NMR, Bruker AV400, 400 MHz) was carried out on Fe^{3+}-GSH solution (D_2O) to investigate the coordination between Fe and GSH. For further structural information, attenuated total reflectance Fourier transform infrared (ATR-FTIR, Bruker) spectroscopy was used to analyse dried Fe^{3+}-GSH powder between 400-4000 cm^{-1}. Circular dichroism (CD) spectroscopy was applied to investigate the chirality change from GSH to Fe^{3+}-GSH complex. CD spectra was carried with a bandwidth of 2.0 nm between 250-750 nm in 10 mm cuvette with 5 ml/mL concentration.

X-ray photoelectron spectroscopy (XPS) was carried out on Fe^{3+}-GSH and GSH powder at room temperature using a Thermo Scientific 250Xi instrument. 1.000eV/step was used for a complete scan and 0.050 eV/step used to scan a particular element.

Electrospray ionisation mass spectrometry (ESI-MS, Bruker maXis impact) was conducted to further elucidate the complex structure. The complex was dispersed in deuterated water and, due to the limited solubility of the Fe^{3+}-GSH complex in deuterated water, deuterated water that contained 20 µL HCl. Positive ion polarity was used in this measurement with scan from 50 m/z to 1500 m/z.

The Fe content of the Fe^{3+}-GSH complex was quantified by thermogravimetric analysis (TGA), with a measurement taken from 10 °C to 710 °C via a heat increase rate of 10 °C/min. The sample was maintained at 710 °C for a further 60 minutes to ensure the complete decomposition of organic matter.

4.2.4 Fe^{3+}-GSH complex water stability analysis

The stability of the Fe^{3+}-GSH complex in H_2O was evaluated by dynamic light scattering (DLS) (Malvern, Nano ZS) at 25 °C with a concentration of 0.5 mg·mL^{-1} in H_2O. Ultrasonic agitation of the solution was conducted prior to analysis. Further analysis of the same samples was carried out after 24 hours at room temperature without any further sample agitation.

4.2.5 Fe^{3+}-GSH complex magnetism evaluation

Fe^{3+}-GSH complex magnetism was measured with from 0-3 T at room temperature by Vibrating-sample magnetometer (Quantum Design, SQUID VSM system).

4.2.6 Fe^{3+}-GSH complex stacking structure investigation

Powder X-ray diffraction (XRD) analysis was scanned from 5°-60° at room temperature, results were fitted by the Lorentz system, before the packing mode was determined using Bragg's law and the Scherrer equation.

$$n\lambda = 2d_{hkl}\sin\theta \qquad \text{Bragg's law}$$

where n is a positive integer, λ is the wavelength of the incident wave, θ is scattering angle, d is crystal lattice spacing.

$$\tau = \frac{K\lambda}{\beta\cos\theta} \qquad \text{Scherrer equation}$$

where τ is the mean size of the ordered (crystalline) domains, K is Scherrer constant, λ is X-ray wavelength, β is FWHM (Full Width at Half Maximum) of XRD peak, θ is scattering angle.

4.2.7 Cytotoxicity tests with Fe^{3+}-GSH complex

The Fe^{3+}-GSH complex was dispersed in cell culture medium at an initial concentration of 2.5 mg·mL^{-1}. L929 murine fibroblasts were cultured (37 °C, 5%

CO_2) in Dulbecco's modified Eagle's medium (DMEM) supplemented with 10 vol.% Fetal bovine serum (FBS), and 0.5 vol.% penicillin–streptomycin. The cell suspension (2×10^4 cells·mL^{-1}) was transferred to a 96-well-plate (100 µL perwell), followed by the addition of increasing Fe^{3+}-GSH concentrations from 0.125 up to 1.25 mg·mL^{-1} in each well. The cell viability was quantified by alamarBlue™ assay after 1 to 7-day culture. Cells cultured on either TCPs or NTCPs were selected as either positive or negative control, respectively.

4.2.8 Metalloproteinase 13 (MMP 13) regulation study

10 mg/mL Fe^{3+}-GSH complex was prepared in 120 mM HCl solution and diluted by deionised water to 2.308 mg/mL. GSH was dissolved in 120 mM HCl solution (1.765 mg/mL, regards TGA data) and set as control group to compare the effect with Fe^{3+}-GSH complex. Both complex and GSH solution were further diluted by H2O (×4) and each 20 µL diluted samples were added into each well of 96-well-plate, followed by 80 µL H2O.

Pro-MMP 13 was activated following the commercial protocol. Briefly, 5 µL MMP 13 (10 µg/20 µL) was dissolved in AMPA working solution (1 mM) to 1 µg/mL and then incubated at 37 °C for 40 minutes. Activated MMP 13 was diluted by *p*-aminophenyl mercuric acetate (AMPA) solution (2 mM) to 25 ng/mL and then immediately added to samples in a 100 µL/tube to ensure that the final concentration of enzyme was 12.5 ng/mL and the testing samples were 25 µL/mL. Deionised water with equal volume of APMA solution (2 mM) was set as a blank and deionised water with equal volume of activated MMP 13 was set as the none treatment group (control group).

After 12-hour or 24-hour reactions, retained MMP 13 activity was quantified using a MMP activity assay kit (Fluorometric Green, ab112146). Each 50 µL of reacted

sample was pipetted into a new 96-well-plate, followed by 50 µL MMP Green Substrate solution. MMP 13 activity was recorded in fluorescence after a 1-hour reaction in the dark at 37 °C using a microreader (Ex/Em=490/525 nm).

4.2.9 Statistical analysis

All the measurements were carried with at least 3 replicates (n≥3). Significant difference was calculated through ANOVA with p value of 0.5 and presented as *p ≤ 0.5, **p ≤ 0.1, ***p ≤ 0.01, ****p ≤ 0.001, *****p ≤ 0.0001.

4.3 Results and discussion

To confirm complex formation upon GSH addition to $FeCl_3$ solution, UV-Vis spectroscopy was used to track metal-chelate coordination for various molar ratios after 30 minutes, when the solution colour remained consistent. The specific absorbance peak at 456 nm was ascribed to Fe-S formation.(196) However, following Fe^{3+}-GSH complex formation, two additional absorption peaks were detected in this system at positions of 452 nm and 550 nm (Figure 4.2a) that didn't present in the spectrum of $FeCl_3$ solution (Figure 4.3). These peaks are attributed to Fe^{3+}-GSH coordination.(197) A regular decrease in absorbance intensity was observed in solutions containing a decreasing molar ratio of $FeCl_3$:GSH (6 → 1), until no peak could be detected in solutions containing a molar ratio lower than 1 (Figure 4.2). This observation can be rationalised by the fact that when solutions with a $FeCl_3$:GSH molar ratio of 1:1.2 or lower were analysed, Fe^{2+} was present exclusively and so no Fe^{3+}-associated absorbance could be recorded, illustrating that binding between Fe^{3+} and GSH occurred only at increased $FeCl_3$:GSH molar ratios (i.e. >1). This observation also reveals that the thiol-induced reduction of Fe^{3+} to Fe^{2+} is expected to occur prior to Fe^{3+} chelation in solutions with increased GSH content, and that the chelating

interaction detected by UV-Vis spectroscopy was exclusively between GSH and Fe^{3+}, rather than between GSH and Fe^{2+}, in solutions with decreased GSH content.

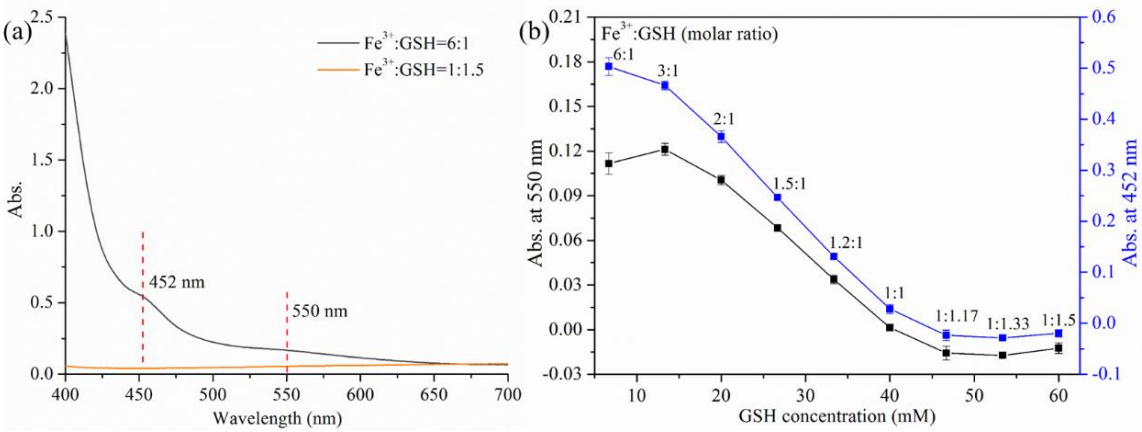

Figure 4.2 UV-Vis Spectroscopy of Fe^{3+}-GSH complex solution formed in H_2O with 40 mM $FeCl_3$. (a): Full wavelength spectrum of solutions containing an $FeCl_3$:GSH molar ratio of either 6:1 (black) or 1:1.5 (orange). (b): Tracking of 452 nm (right-y-axis) and 550 nm (left-y-axis) absorbances recorded in solutions with varied $FeCl_3$:GSH molar ratios from 6:1−1:1.15.

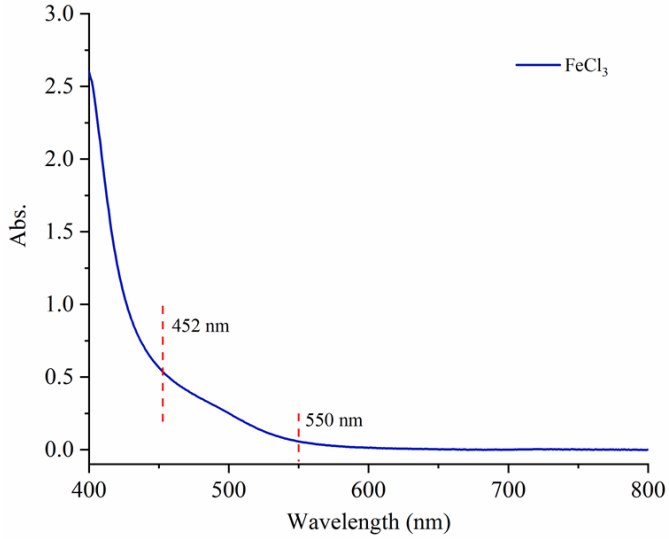

Figure 4.3 UV-Vis spectrum of a 40 mM $FeCl_3$ aqueous solution depicting absorption peaks at 452 nm and 550 nm.

Monitoring the colour of the Fe^{3+}-GSH complex-yielding solution ($FeCl_3$:GSH= 1:1) revealed that the starting yellow-like ferric chloride solution immediately shifted to a dark green colour for approximately three seconds upon addition of GSH (Figure 4.4A). The solution then became lighter yellow, in comparison with the starting $FeCl_3$ solution, as shown in Figure 4.4A. The quick formation of dark green solution is attributed to the reduction of Fe^{3+} to Fe^{2+}, and the oxidation of the GSH thiol, whereby either a disulfide bridge forms between two GSH molecules, a Fe-S bond forms, or a combination of both may form depending on the selected Fe^{3+}:GSH molar ratio (Figure 4.4B). As the pH of the solution containing both $FeCl_3$ and GSH is acidic (pH < 3), the disulfide bridge may be reduced and Fe^{2+} undergo oxidation after approximately 3 seconds rather than air oxidation which usually takes days in sealed environment, when the light yellow solution formed. Then ethanol was added into the yellow solution as presented in Figure 4.4A, f, yielding a pale red precipitate (Figure 4.4A, g), which was washed by ethanol for three times and dried at 37 °C for further characterisation. The proposed mechanism for complex formation is provided in Figure 4.4B.

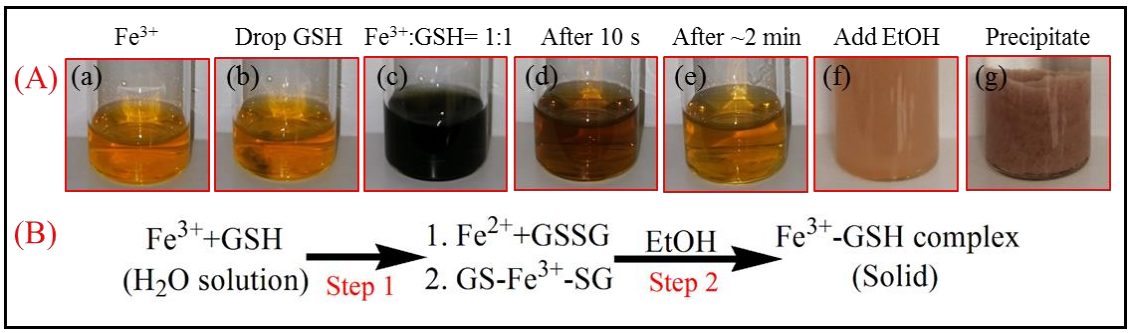

Figure 4.4 Colour solution change that accompanies the transition of $FeCl_3$ solution to the precipitated Fe^{3+}-GSH complex (A) and proposed mechanism of Fe^{3+}-GSH complex formation (B).

The capability of GSSG to induce iron oxidation, as shown in step 2, was confirmed by the GSSG-induced colour change of a $FeCl_2$ solution. The solution was shifted from colourless to pale red colour, which is ascribed to the formation of a Fe^{3+} coordinated GSH complex (Figure 4.5). This phenomenon confirmed the redox reaction between S-S bond Fe^{2+} and the possibility of forming a stable Fe^{3+}-GSH complex.

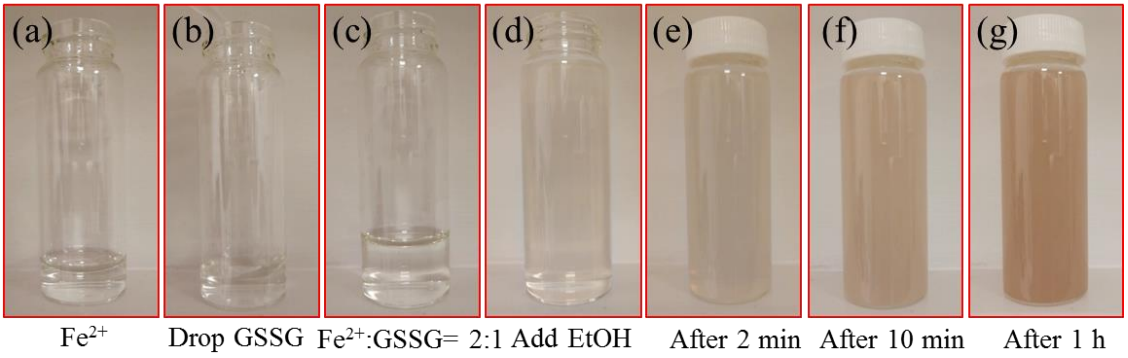

Figure 4.5 Colour change of the ferrous chloride solution following addition of oxidised glutathione, describing the transition from the Fe^{2+} oxidation state to the Fe^{3+}-GSH complex.

The iron valence of the Fe^{3+}-GSH complex was evaluated by ^{57}Fe Mössbauer spectroscopy at room temperature, 293 K (Figure 4.6). All iron in the complex was confirmed to be ferric (Fe^{3+}) valance, with no evidence of any magnetically ordered phases.(192) (193) (198) Approximately 60% of the spectral area is consistent with Fe^{3+} with an octahedral structure that is slightly distorted towards tetrahedral in character, as evidenced by the relatively low Δ (doublet 1, centre shift (δ) = 0.417 $mm \cdot s^{-1}$, quadrupole splitting (Δ) = 0.650 $mm \cdot s^{-1}$), and approximately 40% of the spectral area is consistent with a more regular octahedral Fe^{3+} structure (doublet 2, δ = 0.447 $mm \cdot s^{-1}$, Δ = 0.987 $mm \cdot s^{-1}$). (192) (193) (198)

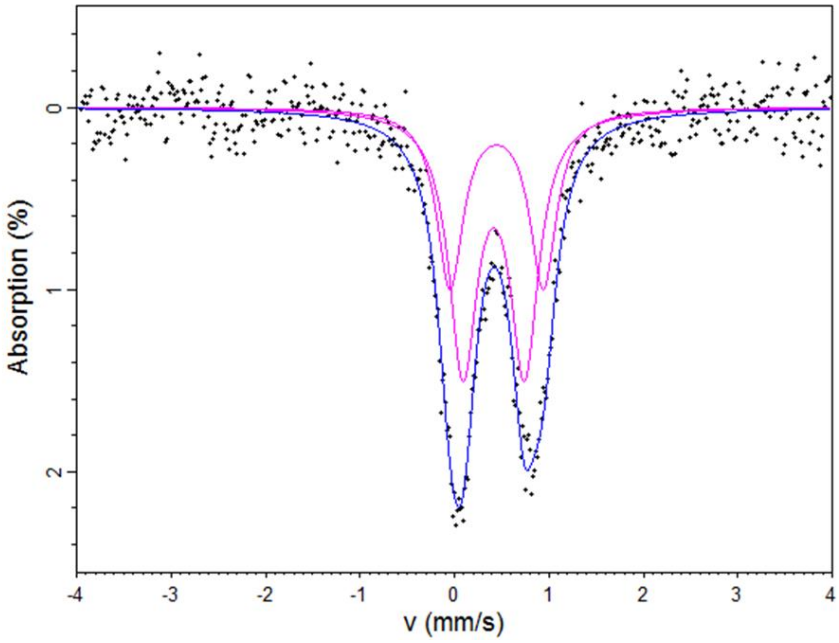

Figure 4.6 Fitted Mössbauer spectrum for the Fe^{3+}-GSH complex powder at 293K.

The ^{1}H-NMR spectrum was carried out to investigate the coordinating structure of the Fe^{3+}-GSH complex as displayed in Figure 4.7, whereby broader peaks can be observed compared to the spectrum of GSH. Peak broadening is ascribed to the paramagnetism of ferric ions (Fe^{3+}), which affects the magnetic field of the instrument and consequently covered related proton splits. However, an obvious shift of the C$\underline{H_2}$-S (position c) protons from 2.87 ppm to 2.89 ppm and 3.19 ppm is evident, and is attributed to Fe-S binding, as the strong metal-chelate coordination affects the neighbouring carbon environment.(192) This conclusion was also further confirmed and is discussed in the later X-ray photoelectron spectroscopy.

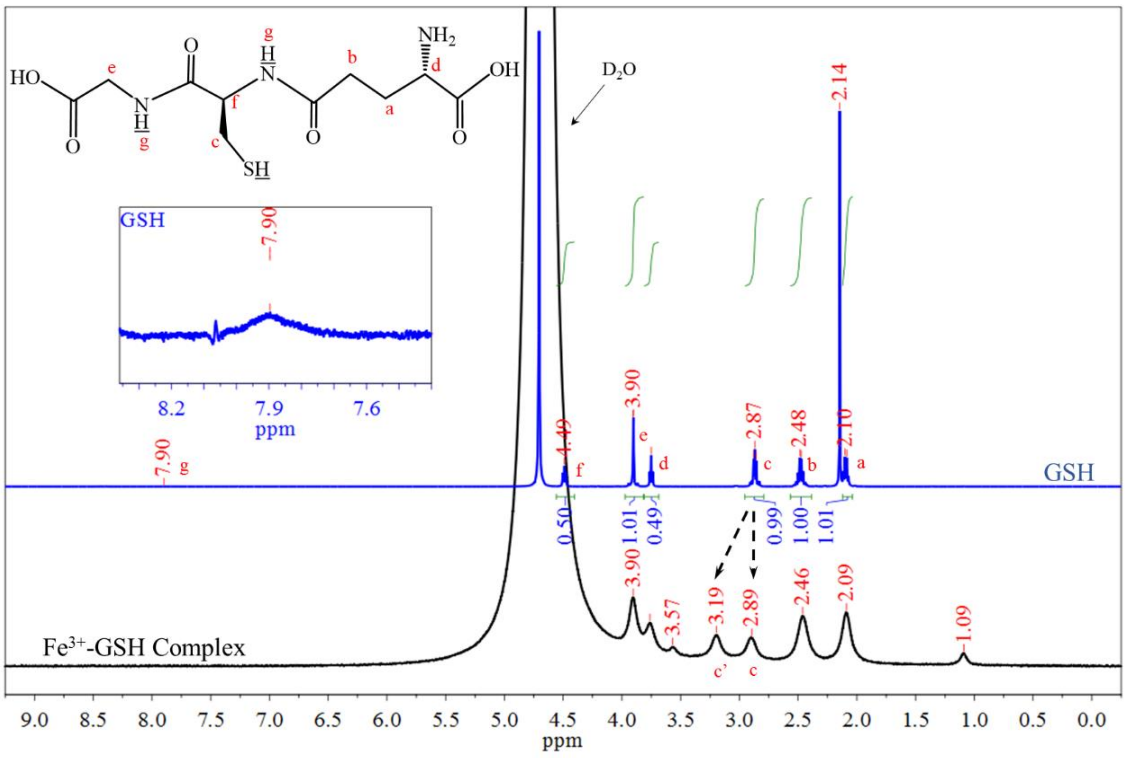

Figure 4.7 ^{1}H-NMR spectra of Fe^{3+}-GSH complex (black) and GSH (blue) in D_2O.

FTIR spectroscopy also revealed differences between the spectra of GSH and Fe^{3+}-GSH complex. A significant shift in the C=O peak position from 1708 cm^{-1} (GSH) to 1737 cm^{-1} (Fe^{3+}-GSH complex) suggested the coordination between Fe^{3+} and glutathione carbonyl oxygen (C=O) as presented in Figure 4.8. The peak at 2522 cm^{-1} in GSH, corresponding to a thiol vibration (-SH), disappeared from the spectrum of the complex, suggesting Fe-S binding. The peaks at 3271 cm^{-1}, 1636 cm^{-1}, and 1526 cm^{-1} correspond to the amine groups of GSH.

Combining the previous unique spectrum from Mössbauer spectroscopy with ^{1}H NMR and FTIR spectra, Fe-S and Fe-O two binding sites in this complex have been strongly proved.

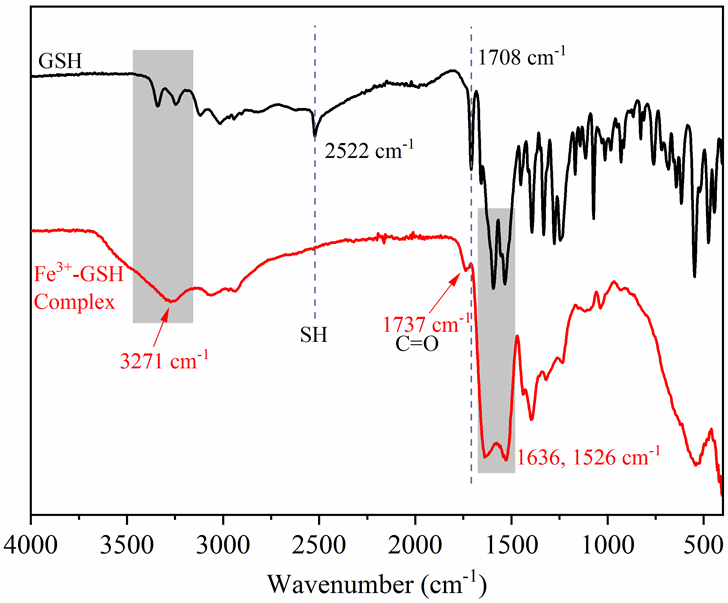

Figure 4.8 IR spectra of GSH (black) and the Fe^{3+}-GSH complex (red).

The Fe^{3+}-GSH complex was also found to display specific peaks in its CD spectrum (Figure 4.9). Compared with uncoordinated GSH in deionised water, the Fe^{3+}-GSH complex presented a broad positive peak from 750 to 460 nm and a negative peak from 460 to 302 nm, assigned to Fe^{3+} coordination. In 60 mM HCl solution, no obvious structural change was observed for the GSH molecule, however, in the spectrum of the Fe^{3+}-GSH complex, an abrupt change was recorded, whereby the opposite trend was observed, at 750-422 nm and 422-360 nm, with respect to when the complex was incubated in H_2O. This change may be due to the presence of H^+,(199) suggesting a partly de-complex process in by acid and a reversible pH-induced peptide folding within the Fe^{3+}-GSH complex. This interesting phenomenon also provided ideas in the study of peptide configuration induction via using metal-chelation method.

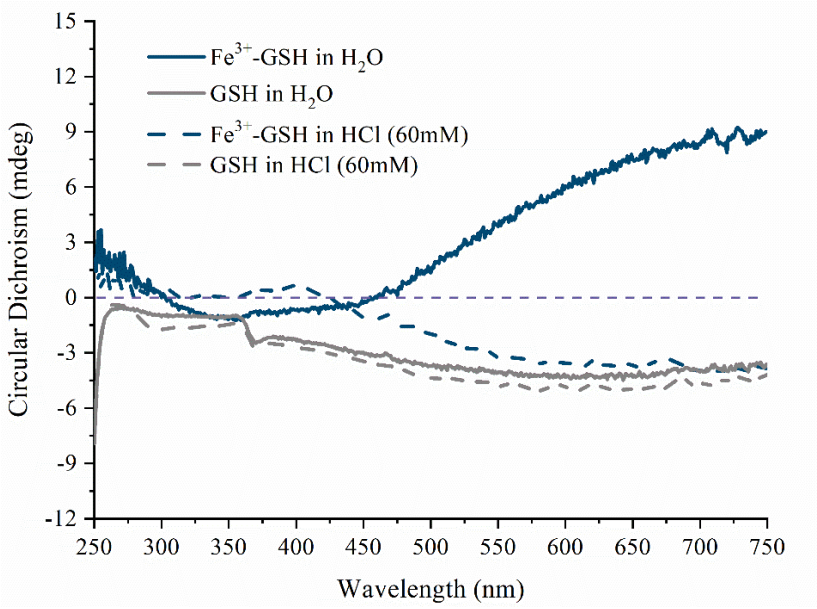

Figure 4.9 Circular dichroism spectra of GSH (grey solid) and Fe^{3+}-GSH complex (blue solid) in deionized water and GSH (grey dash) and Fe^{3+}-GSH complex (blue dash) in 60 mM HCl.

Surface element analysis excluded the formation of S-S bonds and further confirmed the chemical composition in coordinated binding energy of the Fe^{3+}-GSH powder. GSH powder was used as a control. The elements present in the Fe^{3+}-GSH complex are presented in Figure 4.10, which reveals that significant shifts were detected in C=O, C-O and S-related bonds (Figure 4.11). No S-S bond was detected in this complex, which would be revealed by a peak at 166 eV, or greater.(200) The thiol group is protected from forming disulfide bridges with other GSH molecules by Fe^{3+} chelation. In addition, no evidence for Fe^{2+} was found, which would be anticipated to appear at 708 ev,(201) rather than the pre-peak, which is normally observed in Fe related compounds.(202) This confirmed the exclusive existence of ferric iron, consistent with the results from Mössbauer spectroscopy.

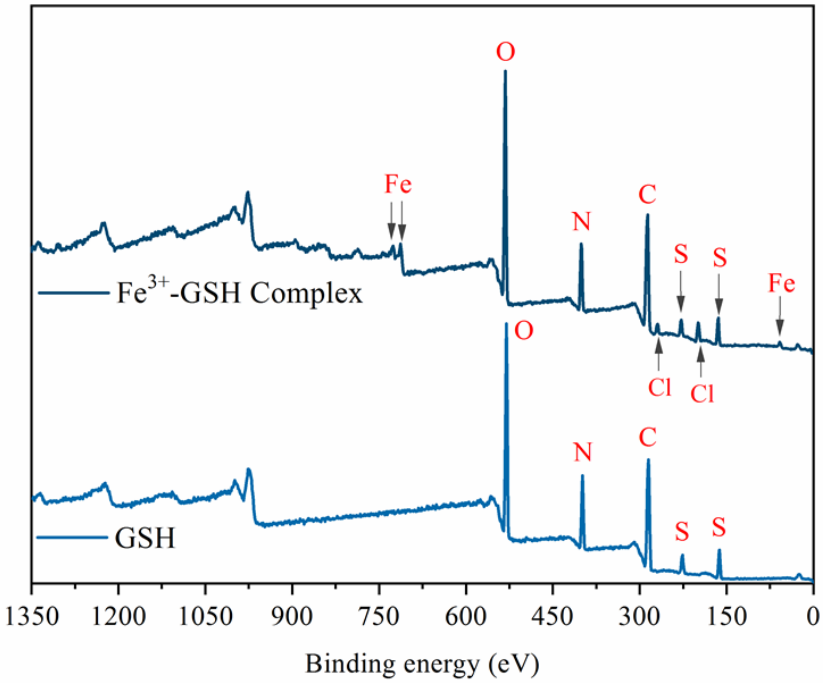

Figure 4.10 X-ray photoelectron spectroscopy (full spectrum of elements) of Fe^{3+}-GSH complex and GSH.

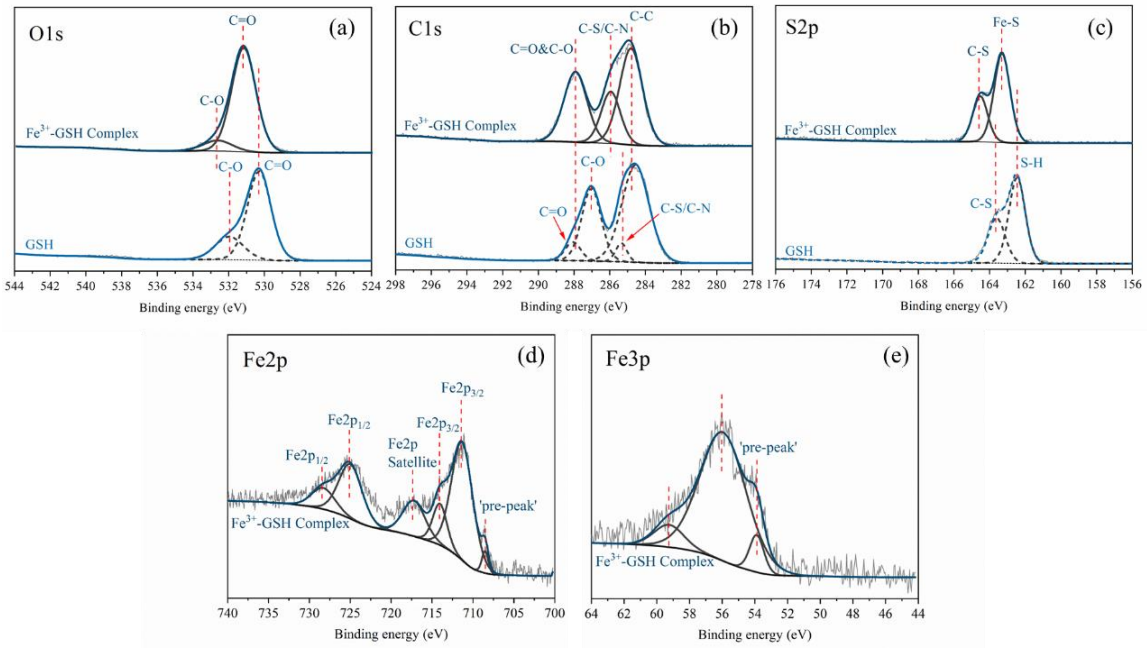

Figure 4.11 X-ray photoelectron spectra of the Fe^{3+}-GSH complex and GSH, C1s (a), S2p (b), O1s (c). Fe2p (d) and Fe3p (e) of Fe^{3+}-GSH complex.

X-ray powder diffraction analysis is a powerful technology for structure analysis. The results from this Fe^{3+}-GSH complex powder revealed that 2θ=23.58° with a full width at half maximum value of 12.13°, as shown in Figure 4.12a. The d spacing of the complex was calculated to be 0.38 nm, and Dp=0.70 nm. The Fe^{3+}-GSH complex was confirmed to possess a 3-layer packing mode, which varied markedly to the crystal structure that was obtained for $FeCl_3 \cdot 6H_2O$ (Figure 4.12b), confirming that a new stacking structure is formed for the Fe^{3+}-GSH complex. The loss of crystal structures also suggested successful synthesis of this new complex.

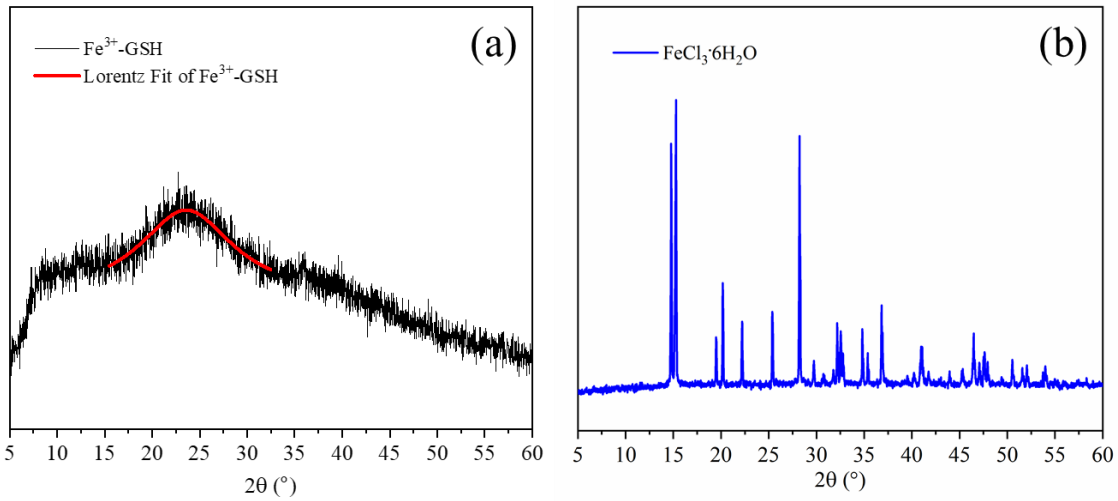

Figure 4.12 X-ray powder diffraction spectrum of Fe^{3+}-GSH complex (a) and Iron(III) chloride hexahydrate ($FeCl_3 \cdot 6H_2O$) (b).

Fluorescence spectroscopy exposed an emission peak at 555 nm under excitation wavelength of 408 nm for the Fe^{3+}-GSH complex dispersed in deionised water (Figure 4.13a). This peak was also present in the spectrum corresponding to a mixture of $FeCl_3$ and GSH (Figure 4.13b). Upon the addition of HCl to the complex solution, the emission peak at 555 nm disappeared. A peak at 473 nm position formed, which lies between values of pure GSH (470 nm) and $FeCl_3$ (493 nm) (Figure 4.13b). The peak at 555 nm is considered to result from the strong binding between Fe^{3+} and GSH, yielding a rigid structure that provides

a new emission peak. Its disappearance after adding HCl suggests that this structure is not stable in acidic solution, with the coordination between Fe^{3+} and GSH reduced, as supported by the accompanying solution colour change from a turbid pale yellow/creamy colour to a transparent colourless solution.

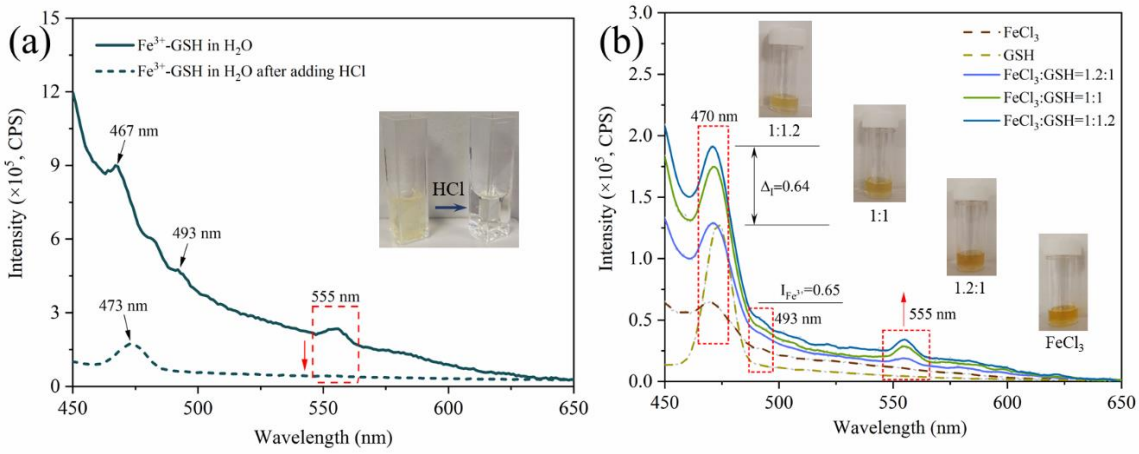

Figure 4.13 Fluorescence spectra analysis of the Fe^{3+}-GSH complex. (a): Fe^{3+}-GSH complex in deionised water with concentration of 1.0 mg/mL, initial status (solid) and after adding 20 µL HCl (dash) under 408 nm excitation wavelength. (b): Fluorescence spectrum of $FeCl_3$ (−−), GSH (−−) and $FeCl_3$-GSH mixture with a molar ratio of 1.2:1 (—), 1:1 (—) and 1:1.2 (—). Spectra were recorded with an excitation wavelength of 408 nm.

Thermogravimetric analysis (TGA) was carried out to further corroborate the chemical composition and composition of the complex. As observed in Figure 4.14, the first mass loss of 12.0% was considered due to water evaporation; the next mass loss from 88.0% to 11.5%, which commenced at 148.3 °C, is ascribed to the loss of GSH. After heating up to 611.8 °C, the complex max remained constant at 11.5%, which was due to the presence of iron. Consequently, it was found that the complex contains 87% GSH and 13% Fe by mass. This is very close to the theoretical composition of 84.6% GSH and 15.4% Fe, based on a total complex mass of 145.4 mg that contains 123 mg GSH.

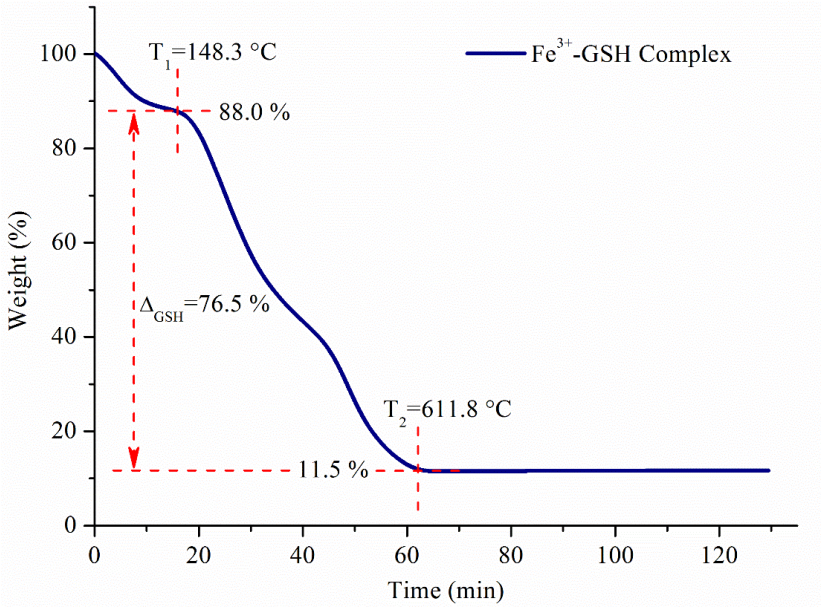

Figure 4.14 TGA thermogram of Fe^{3+}-GSH complex.

Although Fe was coordinated to water-soluble GSH, the solubility of the Fe^{3+}-GSH complex in water remained low due to the ionisation equilibrium of Fe itself. Iron ions tend to gain hydroxide ligands in neutral and basic water. Mass spectroscopy analysis revealed peaks at 615 m/z, attributed to GSSG, and 308 m/z, attributed to GSH (Figure 4.15). In contrast to mass spectrometry, XPS investigations revealed the absence of S-S bridges, suggesting that the formation of the oxidised product in the mass spectra is attributed to the electron source forming ionised species, which form GSSG in the instrument channel. Significant enhancement in peak intensity was observed after adding 20 µl HCl (final concentration of HCl was 120 mM), from 8.9×10^5 to 13.2×10^5 peak intensity at 615 m/z and from 0.8×10^5 to 5.3×10^5 at 308 m/z. The peak at 669 m/z confirms the formation of the GS-Fe-SG complex, although its intensity surprisingly increased upon the addition of HCl. The enhancement of this peak following HCl addition, together with the change in solution colour from medium yellow to almost a colourless solution, suggested the ionisation of the Fe^{3+}-GSH complex

had occurred, resulting in the oxidisation of GSH to GSSG, and the partial formation of Fe^{2+} species.

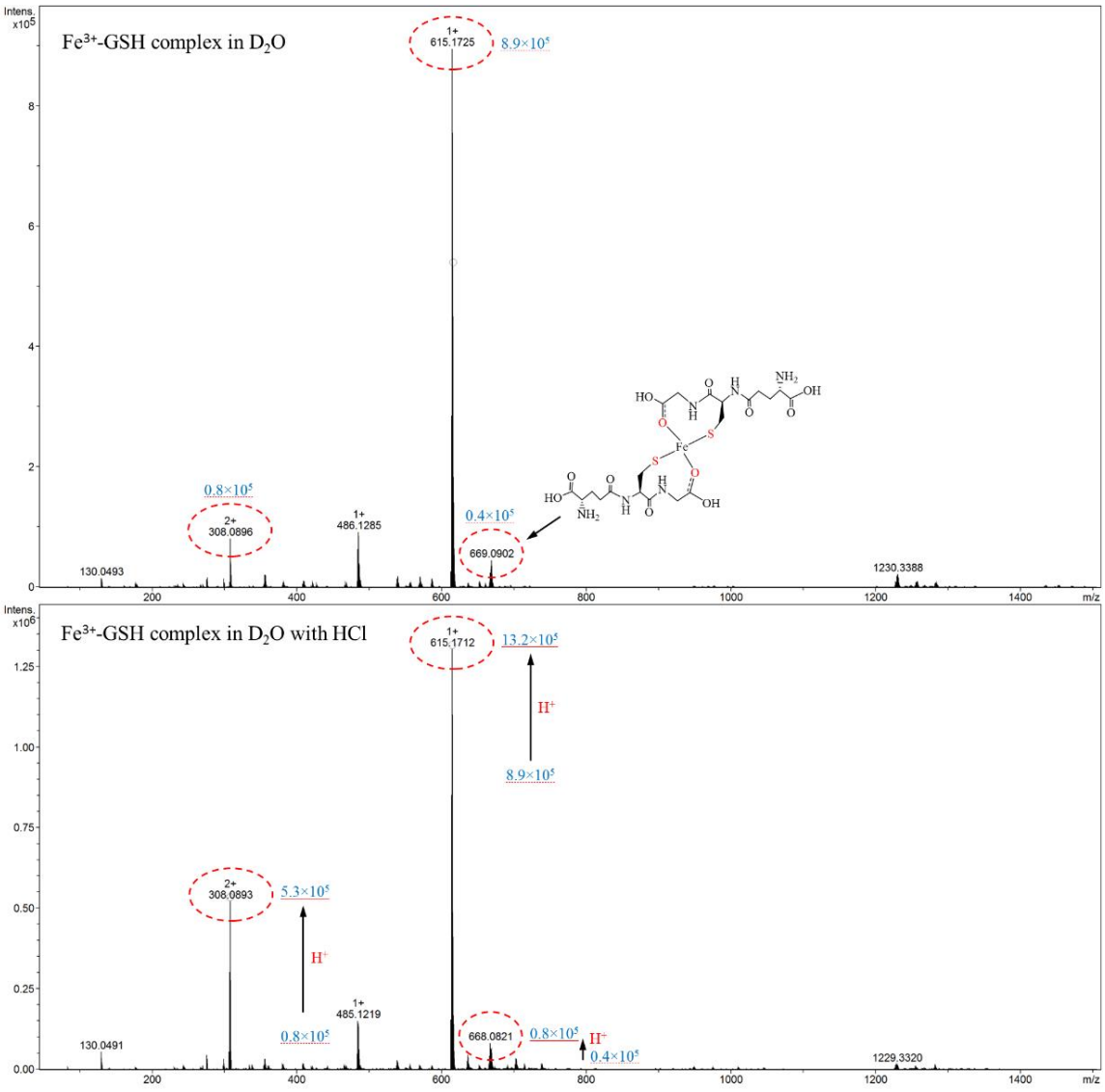

Figure 4.15 Mass spectra of Fe^{3+}-GSH in D_2O without (a) and with HCl (b).

DLS analysis revealed that the Fe^{3+}-GSH complex was stable in water, leading to nanoaggregates with an average effective size of 255±4 nm (PDI=0.258±0.015). Following 24-hour storage in water at room temperature, the complex remained well dispersed with an average effective size of 257±2 nm (PDI=0.247±0.008, Figure 4.16). This characteristic may be exploited to generate bespoke Fe^{3+}-GSH carriers capable of the prolonged, or redox-mediated, release

of GSH to, for example, chronic tissues that have downregulated levels of GSH.(169)

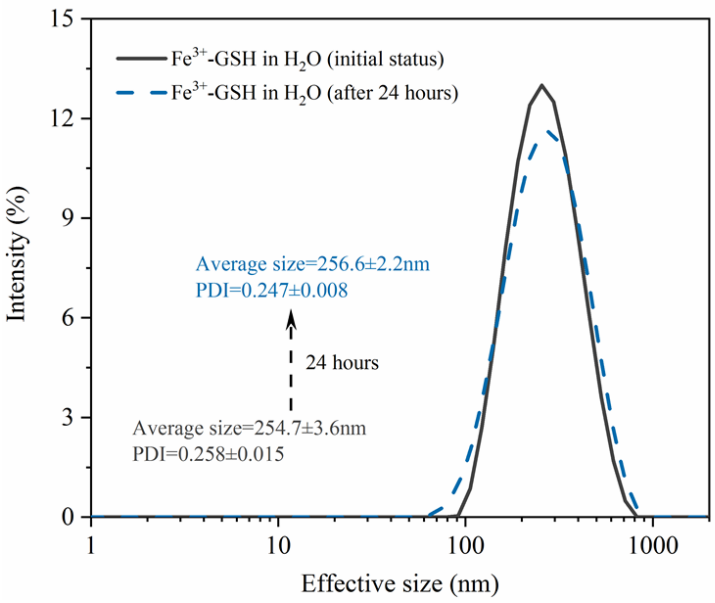

Figure 4.16 The effective size of Fe^{3+}-GSH in H_2O at a concentration of 0.5 mg/mL, initial status (solid) and storage in water for 24 hours (dash).

The magnetic property of Fe^{3+}-GSH was observed using a vibrating-sample magnetometer. The increase in magnetic moment from -0.1474 emu/g to 0.1474 emu/g was recorded as the increasing magnetic field within 3 T, revealing the paramagnetism of the complex (Figure 4.17). This paramagnetic property under 3 T, which is the widely used magnetic field clinically for magnetic resonance imaging (MRI), provided potential application of this Fe^{3+}-GSH complex, for example, as a potential contrast agent. Combining its stable dispersion in water as nanoaggregates (Figure 4.16), great potential can also be expected in prolonging its paramagnetism *in vivo* for a time-dependent observation through MRI.

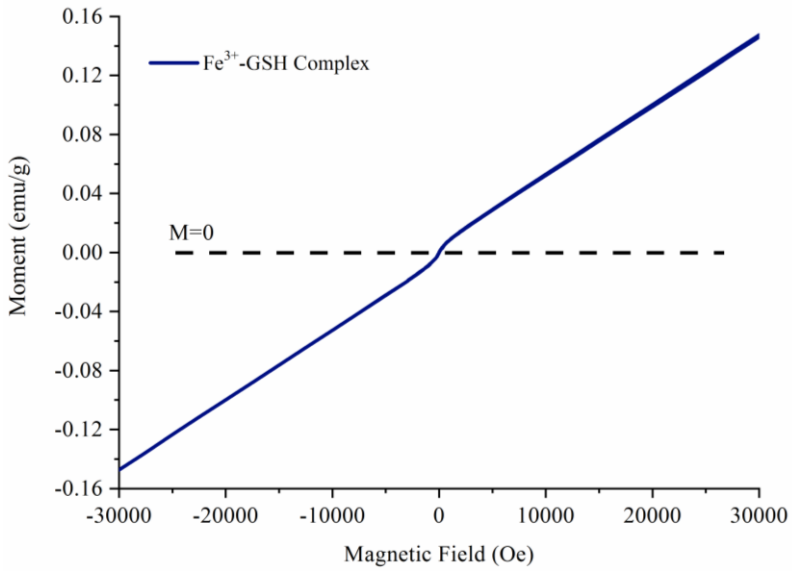

Figure 4.17 Vibrating-sample magnetometer measurement of Fe^{3+}-GSH from -3 T to 3 T magnetic field at room temperature.

Following systematic characterisation of the complex, attention moved to its applicability within a biological environment. Cytotoxicity experiments were carried out with L929 mouse fibroblasts and confirmed high cellular tolerability of the Fe^{3+}-GSH complex. Growth and proliferation of L929 cells were measured during a 7-day culture (Figure 4.18) with all the complex concentrations used in the cell culture medium, strongly supporting the excellent complex cytocompatibility (Table 4.1). Even compared with TCPs, only temporary inhibition was found in cell proliferation in the first 3 days. After 5-day culture, no significant difference could be observed in cell growth with cells cultured with either 0.125 mg/mL, 0.25 mg/mL, 0.5 mg/mL or 0.75 mg/mL of Fe^{3+}-GSH. After 7 days culture, L929 cells in 0.125 mg/mL presented significant higher viability and no significant difference was found in 0.25 mg/mL and 0.5 mg/mL condition. When high Fe^{3+}-GSH content (> 0.5 mg/ml) was supplemented to the cell culture medium, cells proved to grow slower with respect to cells cultured on TCPs, suggesting a significant GSH-induced impact on cellular activity at increased complex concentrations. In addition to possessing cellular tolerability, the Fe^{3+}-

GSH complex proved also to be stable following 24-hour incubation in cell culture medium, suggesting long-lasting GSH storing capability (Figure 4.19, a-d). Provided the relaxation time can be evaluated, potential applicability as magnetic resonance contrast agent might be additional advantages of this complex.

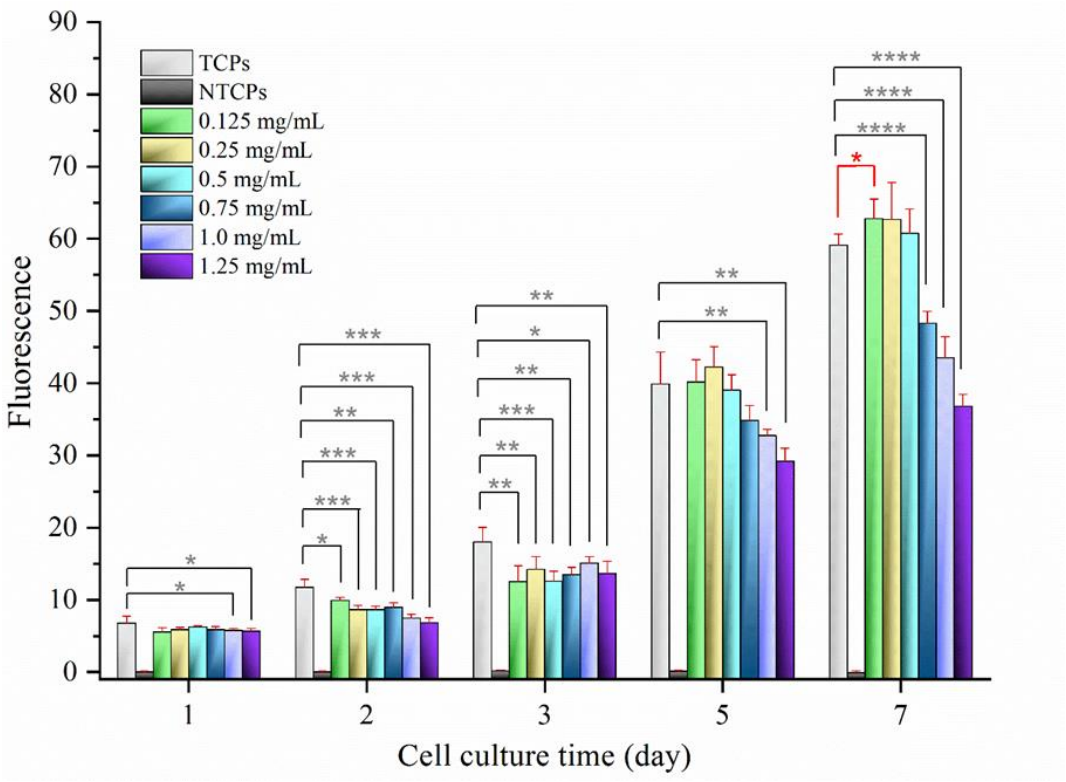

Figure 4.18 L929 cell viability without/with Fe^{3+}-GSH complex for 7 days culture.

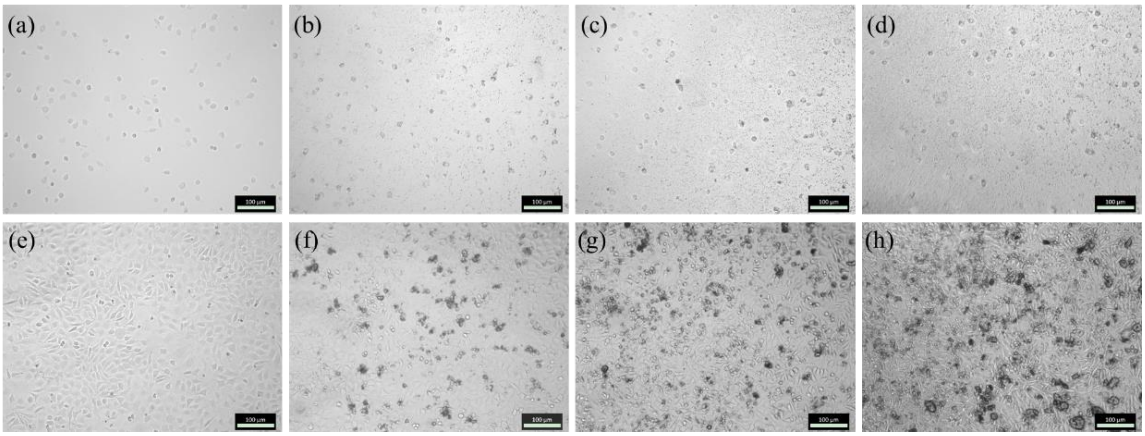

Figure 4.19 Optical images captured following 1-day (a-d) and 7-day (e-h) culture of L929 murine fibroblasts on either TCPs (a, e), or cells culture medium supplemented with Fe^{3+}-GSH complex at a concentration of 0.125 mg·mL^{-1} (b, f), 0.25 mg·mL^{-1} (c, g) or 0.5 mg·mL^{-1} (d,h). Scale bar=100 µm.

Table 4.1 Statistical analysis of L929 cells viability following 7-day cell culture on either TCPs or cell culture medium supplemented with varied concentrations of Fe^{3+}-GSH complex. p ≤ 0.5 (*), p ≤ 0.1(**), p ≤ 0.01 (***), p ≤ 0.001 (****).

	1 day	2 days	3 days	5 days	7 days
TCPs	***	***	****	****	
0.125 mg/ml	****	----	****	****	
0.25 mg/ml	****	***	****	***	
0.5 mg/ml	****	***	****	****	
0.75 mg/ml	****	****	****	****	
1 mg/ml	****	****	****	***	
1.25 mg/ml	**	****	****	***	

MMP 13 activity decreased to 79.5±6.7% after 12-hour incubation with the complex (Figure 4.20). A further decrease to 77.6±2.1% was observed over the next 12 hours. After 48 hours incubation, MMP 13 activity was downregulated to 73.9±1.0%. A significant difference was shown at time points, compared with the MMP 13 group. Conversely, no significant difference was observed in the GSH group. This quick and lasting downregulation proved the ability of the Fe^{3+}-GSH complex to inhibit MMP 13 activity, and suggested great potential for the complex to be applied to inflammation, wound, and arthritis management by downregulating MMP activity.

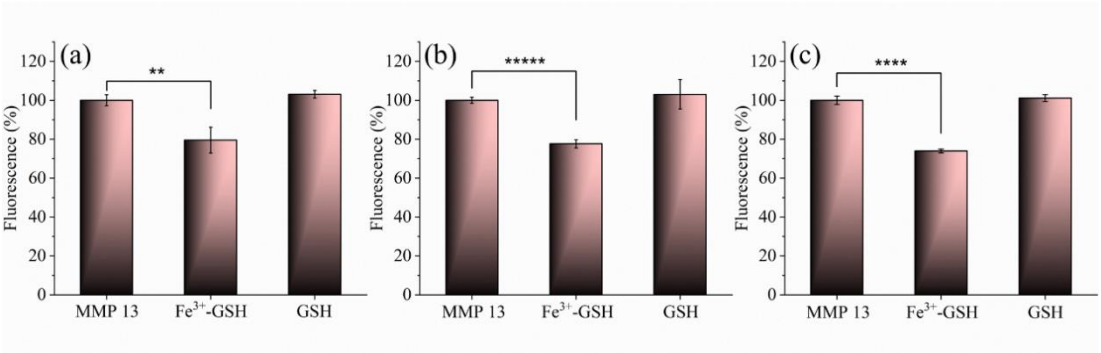

Figure 4.20 MMP 13 activity following incubation with Fe^{3+}-GSH or GSH for (a) 12 hours, (b) 24 hours, (c) 48 hours.

4.4 Conclusion

The formation of a Fe^{3+}-GSH complex without sulfur within its structure is reported and characterised for the first time. Aggregate formation of the complex in water yielded stable particulates with an initial average effective size of 255±4 nm. Such aggregates dispersed in aqueous solution and were found to be non-cytotoxic against L929 fibroblast cells. Fibroblast growth and proliferation was enhanced versus TCPs after seven days of cell culture, suggesting that the material has great compatibility to L929 cells and also potential ability in GSH storing in cell culture medium. Additionally, the complex kept reducing the activity

of MMP-13 over 48 hours, rendering it a highly promising candidate as a treatment for MMP-13-associated conditions.

Chapter 5

An injectable, self-healing and MMP-inhibiting hyaluronic acid gel formed via crosslinking with an iron-glutathione complex

- This chapter has been published. Reference [Gao, Z., Yang, X., Jones, E., Bingham, P.A., Scrimshire, A., Thornton, P.D. and Tronci, G. 2020. An injectable, self-healing and MMP-inhibiting hyaluronic acid gel via iron coordination. International Journal of Biological Macromolecules. 165, pp.2022–2029.]

Regulating the activity of matrix metalloproteinases (MMPs) is a potential strategy for osteoarthritis (OA) therapy, although delivering this effect in a spatially and temporally localised fashion remains a challenge. Aiming to develop a material-based approach to restore tissue homeostasis and reduce patient pain, this chapter presents an injectable and self-healing hydrogel enabling MMP-13 regulation and biomechanical competence *in situ* (Figure 5.1). The hydrogel is realised exploiting the prompt coordination between hyaluronic acid (HA) and a recently developed cell friendly iron-glutathione complex in aqueous environment. Complete solution gelation was successfully achieved within 1 minute at room temperature, with the resulting hydrogel displaying up to 300% in shear strain and no toxic effects to ATDC 5 chondrocytes, in line with the self-healing property and biocompatibility requirements of knee joint interventions. Together with the coordination capability with HA, the presence of the iron-glutathione complex was key to induce significant inhibition of MMP-13 activity in defined solutions *in vitro*, unlike the case of a commercial HA injection (OSTENIL® PLUS). 24-hour incubation with a clinical synovial fluid sample collected from a late-stage OA patient revealed reduced MMP activity of 81.0±7.5% in the presence of the

reported hydrogel, compared to 92.3±27.3% when OSTENIL® PLUS was included and 100.0±17.6% in native synovial fluid, providing prospective improvement in clinical treatment compared to a commercially available medication.

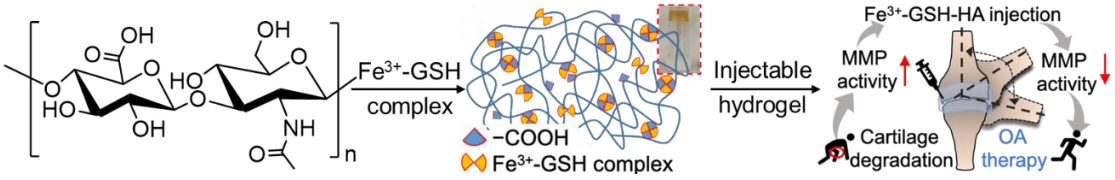

Figure 5.1 Illustration of self-healing Fe^{3+}-GSH hydrogel for osteoarthritis injection.

5.1 Introduction

OA is a chronic and irreversible disease which results in continuous cartilage degradation, increased joint friction, and pain. The onset and progression of OA is closely linked to proteolytic imbalances, whereby upregulated activity of MMPs, particularly MMP-13 (collagenase), results in the pathological breakdown of articular cartilage.(203-205). MMP-13 concentration strongly correlates to VEGF concentration, which plays an important role in angiogenesis and can serve as a biomarker for OA diagnosis and therapeutic monitoring.(206) In addition, the overexpression of MMP-13 is found in advanced osteoarthritic synovial fluid.(207) Injectable, non-cytotoxic and biomechanically viable materials that are able to inhibit MMP-13 are highly sought to restore tissue homeostasis and minimise the risks of knee replacement.(208)

Injectable materials enable the delivery and localisation of therapeutic compounds at a target diseased site. In particular, injectable materials that mimic the features of the extracellular matrix (ECM) are ideal therapeutic scaffolds since they enable cell attachment, proliferation and temporally controlled mechanical function with minimal toxic effect following degradation.(209-210). As such, they have been widely employed as carriers for improved mesenchymal stem cell (MSC) delivery for bone repair and OA management.(211) Hydrogel systems that contain synthetic polymers have shown promise as materials for OA management due to their injectability and versatility in presenting bioactive functionalities that downregulate MMP activity and prolong the activity of encapsulated MSCs.(212) Yet, the limited degradability of many synthetic polymers, and the demands of polymer synthesis make their translation to commercial products challenging. The design of injectable hydrogels from ECM-derived polymers that can correct proteolytic imbalances may provide an

alternative cell-free and regulatory-friendly strategy for OA management, which avoids non-biodegradable synthetic polymers.

HA is an anionic non-sulfated glycosaminoglycan that constitutes one of the main components of cartilaginous ECM.(213) Consequently, commercial HA injections, for instance OSTENIL® PLUS, are routinely applied in the clinic for the management of osteoarthritic joints, where they provide for mechanical supplementation. Significantly improved knee function and pain relief were confirmed through the Visual Analog Scale (VAS) score and the Western Ontario and McMaster Universities Osteoarthritis Index (WOMAC) score. (138) (214) HA injections are usually suggested to be delivered every 1-2 weeks to the joint cavity, although they are unable to control OA-related MMP upregulation. Despite HA's capability to interact with, and stimulate chondrocytes *in vivo*, these products are only designed to offer a palliative, short-lived biomechanical solution that is used as a last resort prior to joint replacement. Intelligent HA formulations that include therapeutics for OA treatment through MMP-13 inhibition, and retain mechanical stability, are highly sought. To pursue this vision, a cell-friendly iron-glutathione (Fe^{3+}-GSH) complex recently reported from previous research in Chapter 4.(215) was investigated for use as both a crosslinker of HA to yield an injectable hydrogel, and as a potential therapeutic to inhibit MMP-13 activity, exploiting the competitive metal-coordinating reaction between complex iron (Fe) and free sulfhydryl groups of active MMPs.

Hydrogel injectability has been pursued via dynamic covalent chemistries in thermo-reversible biopolymer-based hydrogels, including Schiff-base reactions,(216) Diels-Alder reactions (DA) click coupling,(217-218) as well as via thermal gelation mechanisms(219) compliant with injection-mediated delivery. On the one hand, the formation of covalently crosslinked hydrogels with

appropriate mechanical properties in physiological conditions to reduce joint friction has up to now proven challenging. This is largely due to the fact that the presence of covalent crosslinks reduces hydrogel's dynamic tensile, compressive and shear strain, limiting hydrogel's ability to bear multiple load-bearing cycles, as in the case of articular cartilage. On the other hand, although thermosensitive polymer formulations have been developed, only a limited number have been made with HA formulations free of the synthetic polymer phase.(219)

Other than covalent networks, redox-based self-healable and injectable polymer hydrogels were achieved that can withstand relatively high shear strain (~50%).(140) (220) Likewise, metal-coordinated hybrid materials have been reported serving as electroconductive materials,(221) catalyst supports,(222) and for magnetic resonance imaging(186) (223). Ultimately, composite hydrogels have been made of multiple biopolymers and bioglass and ionically crosslinked by calcium dications.(224) The composite material is able to withhold quercetin, an MMP inhibitor, so that 70% reduction in MMP-13 expression was reported after 48 hours, which proved key to induce cartilage repair after 12 weeks *in vivo*. These studies provide novel design concepts that harness the functionalities of metals and peptides, aiming to build simple ECM mimetics with flexible mechanical properties and MMP inhibition capability.

In this chapter, the straightforward creation of a non-toxic HA-based hydrogel that is injectable and self-healing is reported. HA combined with an iron (III)-glutathione (Fe^{3+}-GSH) complex results in the formation of a physical hydrogel upon co-injection. Crucially, the Fe^{3+}-GSH complex has the dual function of being the crosslinker within the hydrogel, and also providing a therapeutic effect for inhibiting MMP activity, as confirmed with synovial fluid (SF) clinical samples collected from patients with late-stage OA. Consequently, the hydrogel may act

as a self-healable scaffold that reduces joint friction and halts cartilage degradation, whilst boosting local cell function. Delivery of this system *in situ* has significant potential in OA therapy, aiming to prevent the degradation of cartilage whilst correcting growth factor concentrations and cellular activity towards cartilage repair.

5.2 Materials and methods

5.2.1 Materials

The hyaluronic acid sodium salt (molecular weight: 1,200 kDa, cosmetic grade) was purchased from Hollyberry Cosmetic. GSH was purchased Alfa Aesar. alamarBlue™ assay kit was from ThermoFisher Scientific. Human recombinant Pro-MMP 13 was purchased from Antibodies.com, and the MMP activity assay kit (Fluorometric Green, ab112146) was from ABChem. All the other reagents were provided by Sigma-Aldrich.

5.2.2 Rheology of HA solutions supplemented with Fe^{3+}-GSH

Different concentrations of Fe^{3+}-GSH complex were added to the HA solution (Table 5.1) to achieve the optimal hydrogel with most stable rheological property. To exclude the influence of HA concentration on gel formation, the final concentration of HA in the gel-forming mixture was controlled to 1.33 wt.% by addition of deionised water. All test group samples were named as “Fe xxx”, in which “xxx” corresponds to the volume of Fe^{3+}-GSH solution (µL) in the HA solution (mL). All control samples were named as “Ctrl xxx”, in which “xxx” corresponds to the volume (µL) of Fe^{3+}-GSH solvent (120 mM HCl) per mL of HA solution.

Fe^{3+}-GSH-supplemented HA solution was injected onto an MCR 302 Rheometer (Anton Paar) and pressed by a 25 mm parallel plate (1.5 mm gap) at 37 °C with

a variable shear rate to study the viscosity of hydrogels formed with different Fe^{3+}-GSH complex content.

Table 5.1 Formulation of different samples.

Sample name	HA (2 wt.%, mL)	Fe^{3+}-GSH (10 mg/ml, μL)	HCl (120 mM, μL)	H_2O (μL)
Fe 100	1	100	0	400
Fe 200	1	200	0	300
Fe 300	1	300	0	200
Fe 400	1	400	0	100
Fe 500	1	500	0	0
Ctrl 0	1	0	0	500
Ctrl 100	1	0	100	400
Ctrl 200	1	0	200	300
Ctrl 300	1	0	300	200
Ctrl 400	1	0	400	100
Ctrl 500	1	0	500	0

**Solvent information: HA (H_2O), Fe-GSH (120 mM HCl), $FeCl_3$ (120 mM HCl), HCl (H_2O).*

5.2.3 Preparation of Fe^{3+}-GSH-HA hydrogel (Fe 300)

The Fe^{3+}-GSH complex was prepared using previous method.(215) Briefly, 123 mg (0.4 millimoles) of GSH was added to 4 mL $FeCl_3$ aqueous solution (0.1 M), and the mixture was mildly agitated by vortex mixing for 2 min until the solution became yellow. Then, the complex was precipitated by adding 40 mL ethanol (×3) and collected by centrifugation at 10,000 rpm for 15 min. The Fe^{3+}-GSH complex was dried at 37 °C for further use.

10 mg of Fe^{3+}-GSH complex was dissolved in 1 mL HCl solution (120 mM). Each 300 µL Fe^{3+}-GSH complex solution was added to 1 mL hyaluronic acid solution (2 wt.%) and stirred at room temperature for 1 min to obtain a self-healing hydrogel (Fe^{3+}-GSH gel).

The self-healing behaviour of all hydrogels formed was characterised by determining the reversible viscosity from a low shear strain (0.01%) for 200 s, followed by a high shear strain (500%) measurement for 100 s at 37 °C. Ten low-to-high shear strain gaps were measured in this process using an Anton Paar MCR 302 rheometer.

5.2.4 Determination of hydrogel rheological properties

The shear modulus (G’ and G’’) of the Fe^{3+}-GSH crosslinked hydrogel (Fe 300) was measured via a frequency sweep using an MCR 302 rheometer (Anton Paar). This method was set with a 25 mm parallel plate at 37 °C, 1.5 mm gap, from 1-100 rad·s^{-1} under 5% amplitude. G’ and G’’ were determined at 37 °C over a shear strain range of 0-500% with a constant angular frequency (5 rad·s^{-1}). Every 1.0 mL volume of Fe^{3+}-GSH gel was injected onto the sample plate and slightly pressed by a 25 mm parallel plate geometry with a gap of 1.5 mm. Hyaluronic acid with the same amount of HCl solution only was measured as a

control for both shear modulus and shear strain. All the experiments were repeated at least three times.

5.2.5 Molecular mechanism study

^{57}Fe Mössbauer spectroscopy was applied to study iron chelation and valence in self-healing hydrogel. Measurements were carried out using acrylic absorber discs (area: 1.8 cm^2) loaded with a dried gel sample to achieve a Mössbauer thickness of 1. The 14.4 keV γ-rays were supplied by the cascade decay of 25 mCi ^{57}Co in Rh matrix source, oscillated at constant acceleration by a SeeCo W304 drive unit, detected using a SeeCo 45431 Kr proportional counter operating with 1.745 kV bias voltage applied to the cathode. All measurements were carried out at 293 K over a velocity range of ±6 $mm \cdot s^{-1}$, and were calibrated relative to α-Fe foil. Spectral data were fitted using the Recoil software package, using a single Lorentzian line shape.

5.2.6 Cytotoxicity studies

ATDC 5 chondrocytes were cultured (37 °C, 5% CO_2) in a mixed medium of Dulbecco's modified Eagle's medium (DMEM) and Ham's F12 medium (1:1 in volume), supplemented with 5 vol.% fetal bovine serum (FBS), and 1 vol.% penicillin-streptomycin. A defined amount of self-healing gel was transferred into individual wells of a 96-well-plate and diluted by cell culture medium to a final concentration of 0 μL (TCPs), 5 μL, 10 μL, 20 μL, 30 μL, 40 μL and 50 μL per well, followed by addition of 100 μL cell suspension (5×10^4 cells/mL) in each well (n=4). The ATDC 5 cell metabolic viability was quantified by alamarBlue^{TM} assay after 1-day and 5-day culture. Cells cultured on TCPs were set as the control group.

5.2.7 Acellular MMP-13 inhibition study

The self-healing gel, as well as an HA solution and a commercial HA gel for OA injection, OSTENIL® PLUS (both with the same HA concentration as the self-healing gel), were added to deionised water (×4). Then, 20 µL of each sample was added to individual wells of a 96-well plate, followed by adding 80 µL H_2O per well.

Pro-MMP 13 was activated following the manufacturer protocol. Briefly, 5 µL MMP-13 (10 µg MMP-13/20 µL sample) was dissolved in a AMPA working solution (1 mM) to 1 µg/mL and then incubated at 37 °C for 40 min. Activated MMP-13 was diluted with AMPA solution (2 mM) to 25 ng/mL and then immediately added into the sample wells (each containing 100 µL of the sample), corresponding to a final MMP-13 concentration of 12.5 ng/mL to cover the enzymatic concentration (6 ng/mL) recorded in synovial fluid samples of advanced OA patients.(207) Deionised water with an equal volume of APMA solution (2 mM) was set as the blank, and deionised water with an equal volume of activated MMP-13 was set as the none treatment group.

After 12-hour or 24-hour incubation, MMP-13 activity was quantified via fluorometric assay (Fluorometric Green, ab112146, Abcam).(225) 50 µL of each sample was pipetted into a new 96-well-plate, followed by 50 µL of MMP Green Substrate working solution. MMP 13-activity was recorded in fluorescence after 1-hour reaction in the dark at 37 °C using a microplate reader (Thermo Scientific Varioskan® Flash, Ex/Em=490/525 nm).

5.2.8 MMPs regulation study with patient collected synovial fluid

Synovial fluid (SF) samples were collected from late-stage osteoarthritic patients at Chapel Allerton Hospital (Leeds, UK) under ethical approval granted by the

National Research Ethics Committee (ethical approval number: 07/Q1205/27). SF samples were stored at -80 ˚C until use.

A fluorometric assay kit (Fluorometric Green, ab112146) was used to measure the total proteolytic activity in both SF and hydrogel-incubated SF samples. SF samples were diluted with the MMP assay buffer (×4), and the final Fe^{3+}-GSH crosslinked gel dose was increased (×4). 50 µL of diluted SF were mixed with 40 µL of Fe^{3+}-GSH crosslinked gel, and 10 µL of deionised water was supplemented in each well to achieve a final concentration of 100 µL/mL [Fe^{3+}-GSH crosslinked gel/solution]. The fluorometric assay was conducted after 24-hour incubation following the same assay protocol reported for MMP-13 activity measurement.

5.2.9 Statistical analysis

All the samples were tested with at least 3 replicates (n≥3) and presented as Mean±SD. Statistical significance level was calculated through one-way ANOVA with a p value at 0.05. Final statistical results were presented as *p ≤ 0.05, **p ≤ 0.01, ***p ≤ 0.001, ****p ≤ 0.0001.

5.3 Results and discussion

Attempts to create hydrogels from HA (2 wt.%) and varying amounts of the Fe^{3+}-GSH complex (10 mg/mL) were conducted, and the optimal hydrogel was formed from 300 µL Fe^{3+}-GSH complex (10 mg/mL) and 1 mL HA solution (2 wt.%). A significant decrease in viscosity was observed with increasing shear rate from 0.01 Hz (14,400 Pa·s) to 4 Hz (37 Pa·s), whereas the viscosity remained constant at shear rates between 4 Hz and 100 Hz (Figure 5.2a). Compared with the other materials created, the high viscosity at low shear rate from 0.01 Hz to 4 Hz proved its stability as self-healing hydrogel and suggested a balanced coordination at a Fe^{3+}-GSH crosslinker concentration of 300 µL per mL of HA solution.

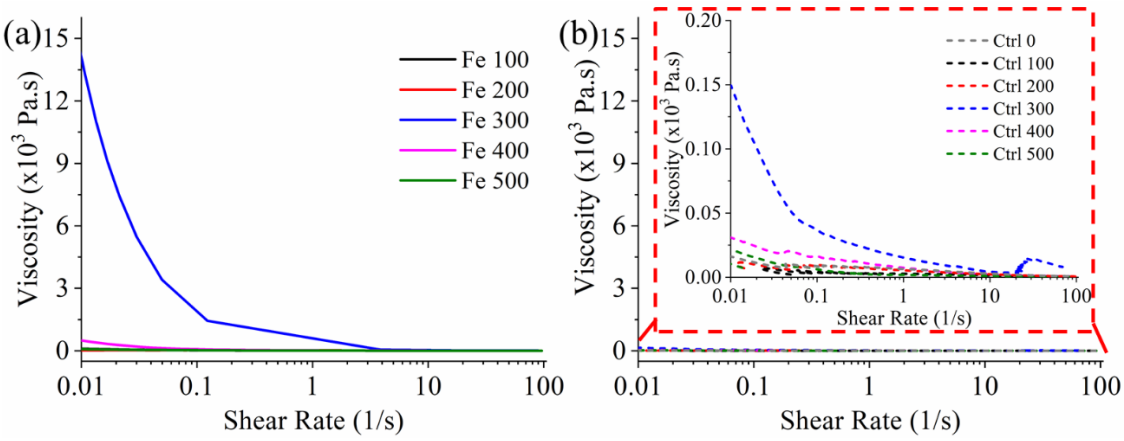

Figure 5.2 Shear rate-Viscosity flow curve of aqueous solutions supplemented with varied Fe^{3+}-GSH complex/HA ratio (a), varied concentration of HA (control group) (b). The highest viscosity to 14,400 Pa·s was recorded in Fe 300 sample at 0.01 Hz, indicated by a solid blue line (a).

On the other hand, in the HA solution control groups, replacement of the Fe^{3+}-GSH complex with the HCl solution resulted in significantly lower viscosity, whereby no significant viscosity variation was observed across the control groups (Figure 5.2b). This remarkable difference from Fe 300 proved a successful formation of HA gel via Fe^{3+} metal binding. Consequently, this hydrogel (Fe 300) was chosen for further investigation.

The clear presence of a doublet attributable to paramagnetic Fe^{3+} can be observed, despite the low signal/noise ratio due to the low abundance of Fe^{3+}-GSH content in the gel. The iron oxidation state in the optimal hydrogel (Fe 300) was ferric (Fe^{3+}) occupying octahedral coordination,(198) (226) as determined by ^{57}Fe Mössbauer spectroscopy, which also confirmed the chelation of Fe^{3+} to HA (Figure 5.3). Furthermore, this only one doublet from Mössbauer spectrum suggested a uniform binding of Fe^{3+}-GSH complex to HA, which gave possibility that the proposed Fe-S binding in initial complex (Chapter 4) was released when it was dissolved in HCl, but the stronger Fe-O binding was remained. And

additional Fe-O might form with HA molecules, replacing initial Fe-S sites in the complex.

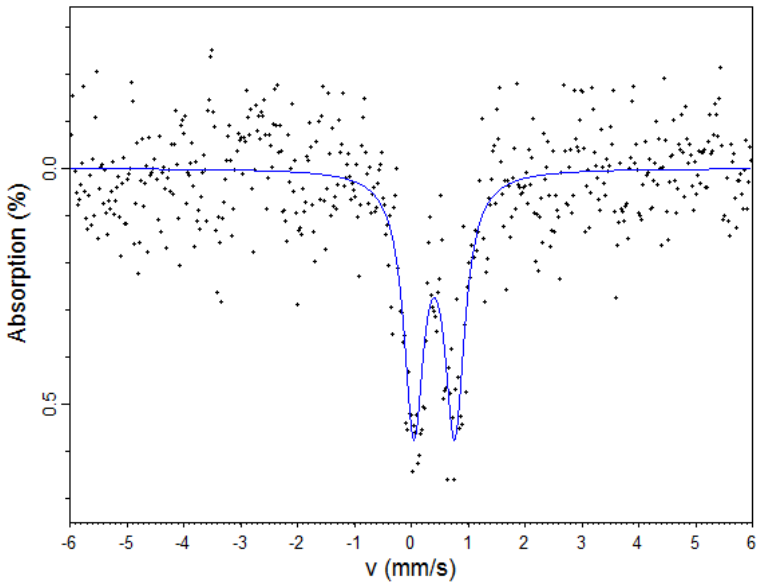

Figure 5.3 Fitted ^{57}Fe Mössbauer spectrum of dry Fe^{3+}-GSH gel network at 293 K, relative to thin α-Fe foil. Fitted centre shift (δ) = 0.41 ± 0.02 mm·s^{-1} and quadrupole splitting (Δ) = 0.72 ± 0.02 mm·s^{-1} with HWHM linewidth = 0.21 ± 0.02 mm·s^{-1}.

A much higher G' value (120 Pa) was recorded for the Fe 300 gel that contained the Fe^{3+}-GSH crosslinker, compared to the HCl-HA control (10 Pa), again indicating that Fe^{3+}-coordination to HA enables gel formation. Constant storage moduli (G'= 120 Pa) and loss moduli (G''= 70 Pa) of the self-healing gel were successfully measured in frequency sweep mode, confirming a predominantly elastic behaviour in the range of 1-40 rad·s^{-1}, whilst the material elasticity was found to decrease at the increased angular frequency (Figure 5.4a). Although the storage moduli is reduced compared to the chemically crosslinked HA hydrogel, which was prepared in Chapter 2 and holding a G' value around 300 Pa (Figure 2.7), the elastic range was much greater than the chemically crosslinked hydrogel (1-10 rad·s^{-1}).This behaviour illustrates the homogeneous nature of the gel.

Conversely, the HCl-HA control sample presented an obvious decrease in moduli from high to low frequency (Figure 5.4b), which was expected as a nature of uncrosslinked polymer solution.

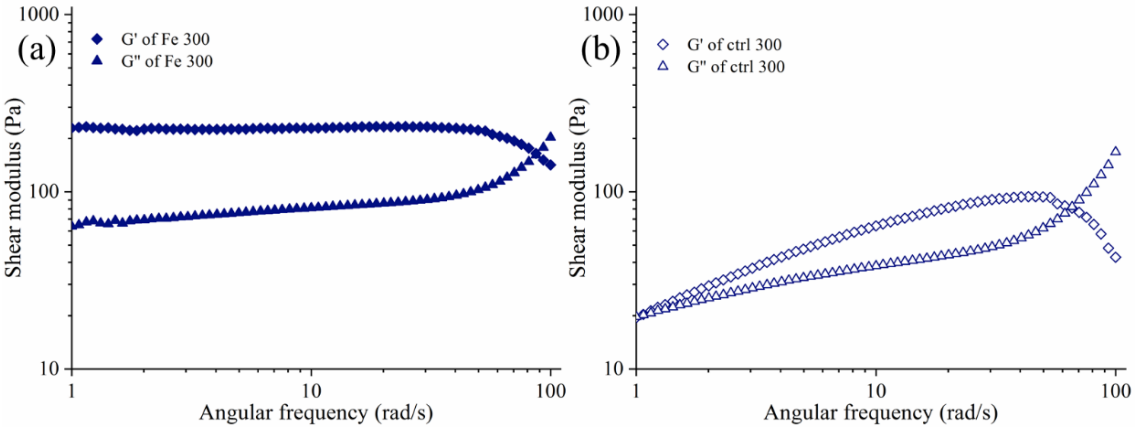

Figure 5.4 Shear modulus of Fe^{3+}-GSH hydrogel (a) and ctrl 300 samples (b) recorded during the frequency sweep.

Figure 5.5a reveals the dependency of dynamic shear modulus under shear strain (0.01-500%) for the Fe^{3+}-GSH crosslinked gel. A predominantly elastic gel response was observed up to 300% shear strain, whereby both the storage and loss moduli remained constant when up to 80% shear strain was applied with 5 rad/s (0.8 Hz) frequency. These results demonstrate mechanical compliance of the hydrogel with the ranges of shear strain (up to 1%) and frequency (0.5-2.0 Hz) observed *in vivo* in both connective and fatty tissues.(227) In line with previous results, the storage modulus of the Fe^{3+}-GSH coordinated gel (105 Pa) was found to be greater than that of the hyaluronic acid control (70 Pa, Figure 5.5b), demonstrating increased mechanical competence and also the formation of hydrogel material, rather than viscous polymer solution.

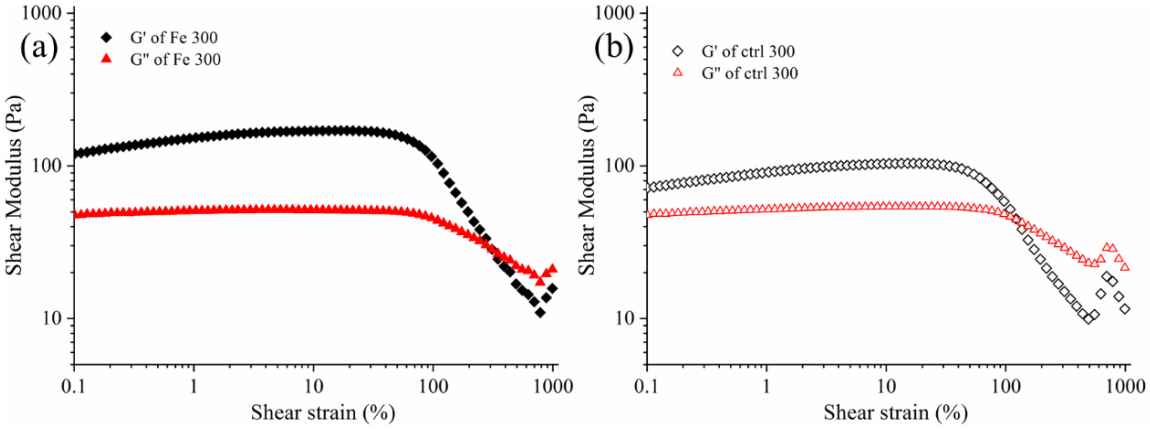

Figure 5.5 Shear modulus of Fe^{3+}-GSH gel (a), HCl control group (b), measured via strain sweep.

During this dynamic viscosity measurement from low shear strain (0.01%) to high strain (500%), Fe^{3+}-GSH crosslinked gels presented a stable reversible complex viscosity in the range of 37-42 Pa·s and 12-16 Pa·s, respectively (Figure 5.6 blue). After 10 cycling tests, the reversible property remained without obvious fatigued phenomenon, confirming this Fe^{3+}-GSH crosslinked gels to be self-healing materials.

The profound degradability of Fe^{3+}-GSH crosslinked hydrogel in aqueous solution was confirmed by the decreased viscosity to 0.1-10 Pa·s after being incubated at 37 °C for 5 days (Figure 5.6 grey). This self-degradable property provided this gel promising biomedical potential as injection in avoiding *in vivo* inflammation. Although the mechanism of degradation was not fully studied, both hydrolysis of HA chains and Fe^{3+}-decomplexation could affect the degradation

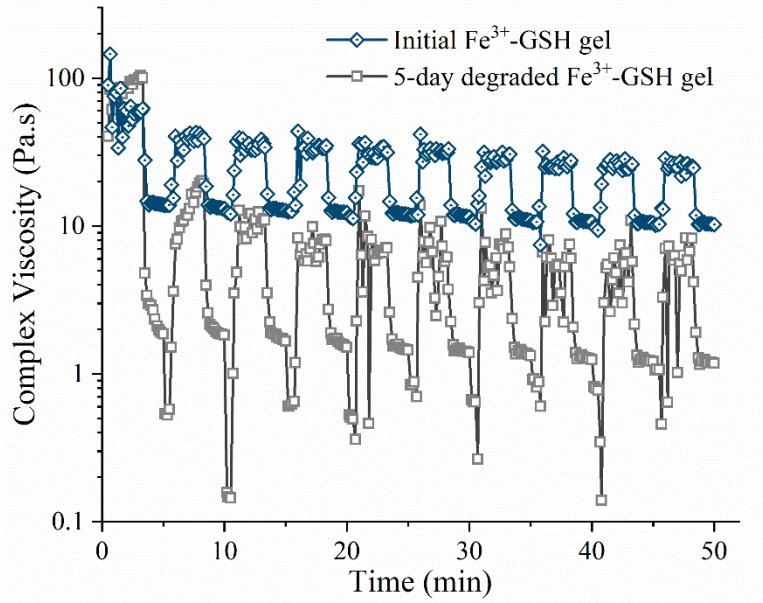

Figure 5.6 Dynamic time-dependent viscosity measurement of initial (blue) and Fe^{3+}-GSH gel after 5-day self-degradation (grey) at 37 °C. Measurements were started with low shear strain (0.01%) for 200 s, followed by another 100 s at high shear strain (500%) at 37 °C.

The formation from HA solution to Fe^{3+}-GSH crosslinked self-healing hydrogel was presented in (a) and (b) of Figure 5.7. Figure 5.7c reveals the elongation and injectability of this self-healing hydrogel, the material can be absorbed (step 1) by a syringe and then be injected through the syringe tip (step 2), before undergoing extensive elongation (step 3). The sticky property of this self-healing hydrogel could also be observed in step 3; in line with previous viscosity analysis, the adhesive properties of HA were enhanced by Fe^{3+}-GSH induction. This feature is key to enable confined application and adhesion of the gel to cartilage, aiming to stabilise the joint cavity and to reduce bone-to-bone friction, which is essential to preserve the cartilage interface.(228)

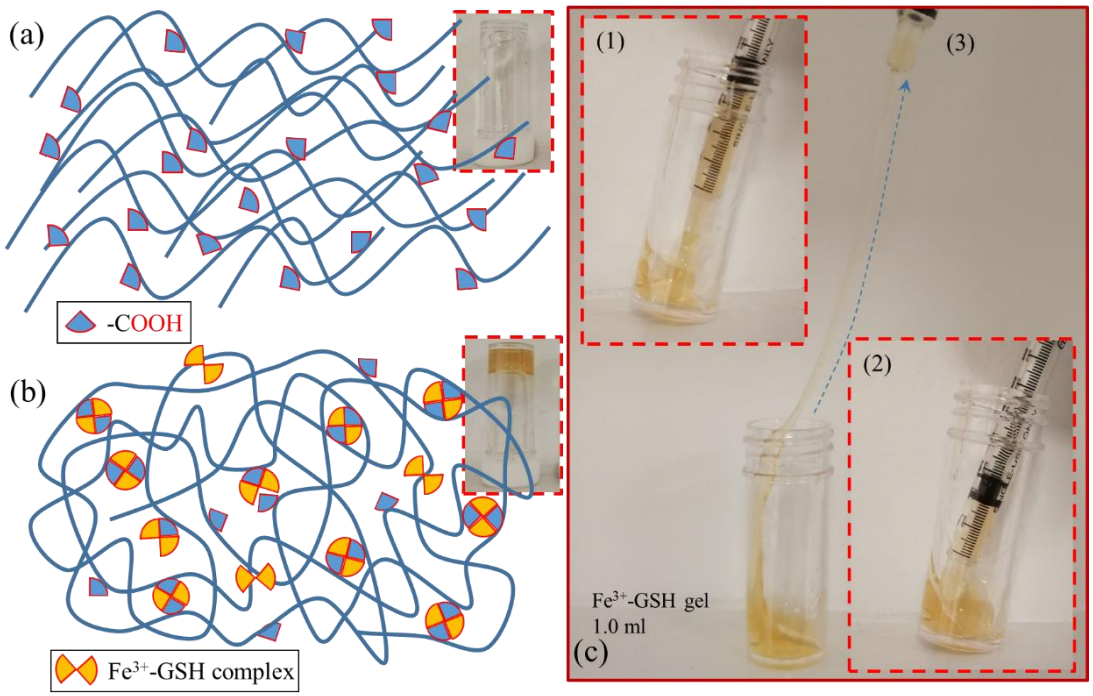

Figure 5.7 Illustration of Fe^{3+}-GSH hydrogel formation. (a): Molecular configuration and physical appearance of the HA solution; (b): Proposed coordination structure within, and physical appearance of, the Fe^{3+}-GSH hydrogel. (c): Macroscopic properties of Fe^{3+}-GSH gel, being loaded up (step 1), injected (step 2) and stretched (step 3).

The dose of Fe^{3+}-GSH crosslinked HA gel that is non-cytotoxic to ATDC 5 chondrocytes was then determined via an *in vitro* cell viability assay (Figure 5.8). As expected, the hydrogel reveals a dose dependent cytotoxicity. At day 1, the lower dose (e.g. 5 and 10 µL) of Fe^{3+}-GSH crosslinked HA gel did not show significant cytotoxicity compared with that of the TCPs control group ($p > 0.05$). However, the high dose groups (e.g. > 20 µL) significantly reduced the viability of ATCD-5 cells compared to the control group ($p \leq 0.01$, 0.001, 0.001, 0.05 respectively). At day 5, only the 5 µL group was not cytotoxic ($p > 0.05$) but all the other higher dose groups were significantly cytotoxic to the cells compared with that of the control group ($p \leq 0.05$, 0.001, 0.0001, respectively). Clearly, no significant difference in cell viability was observed following 1-day cell culture in

either TCPs or lower doses of Fe^{3+}-GSH crosslinked hydrogel (with both 5 µL and 10 µL dose).

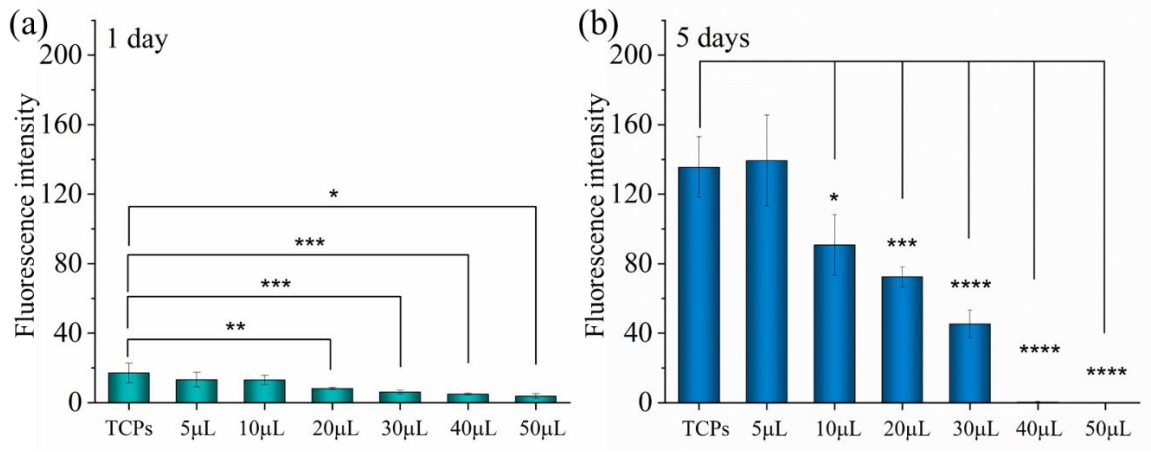

Figure 5.8 ATDC 5 cells viability when growing with Fe^{3+}-GSH gel after 1 day (a) and 5 days (b). Data was presented as Mean±SD, statistical analysis was carried out between each two groups and labelled as *p≤ 0.05, **p≤ 0.01, ***p≤ 0.001, ****p≤0.0001, otherwise means no significant difference at p=0.05 level.

Furthermore, the increase in metabolic activity recorded from day 1 to day 5 in ATDC 5 cells cultured with 5 30 µL hydrogel (Table 5.2) was similar to that measured in cells treated with the TCPs control group (7.9 times). This observation indicates that decreased doses (e.g. $\leqslant$ 30 µL) of Fe^{3+}-GSH hydrogel did not affect the cell proliferation (e.g, cell doubling) in this time window, in contrast to the case where higher doses (e.g. $\geqslant$ 40 µL) were applied. Given that the initial cell seeding density (5,000 cells per well) was maintained across all hydrogel groups (5-50 µl), the reduced cellular metabolic activity observed with increased gel volume (> 30 µl) is likely attributed to the relatively small number of cells cultured with increased sample dosages. This observation may suggest that the gels under 30 µL dose were temporarily toxic after 1-day, however, the proliferation of the remaining ATDC 5 cells was not affected, an explanation which

is supported by the optical microscope images of cells cultured for 1 (Figure 5.9) and 5 days (Figure 5.10). In contrast, no proliferation was observed in both 40 and 50 µL groups over 5 days.

Combining toxicity data with initial cell seeding density (5,000 cell/well) enables a correlation between cytotoxicity and gel volume to be made; 5,000 cells are tolerant to a maximum gel volume of 0-30 µL.

Table 5.2 ATDC 5 cell viability increase from 1 day to 5 days in selected sample groups.

Sample ID	Average cell viability increase (Times)
0 µL (TCPs)	7.9
5 µL	10.5
10 µL	7.0
20 µL	8.8
30 µL	7.4
40 µL	0.1
50 µL	0

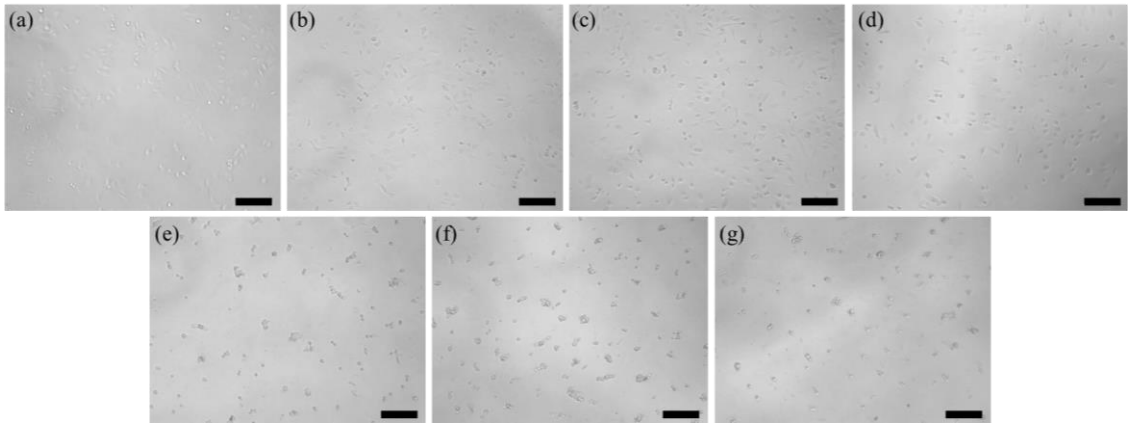

Figure 5.9 Optical images of ATDC 5 cells after 1-day culture with Fe^{3+}-GSH gel, (a) 0 µL (TCPs), (b) 5 µL, (c)10 µL, (d) 20 µL, (e) 30 µL, (f) 40 µL and (g) 50 µL per well. Scale bar, 100 µm.

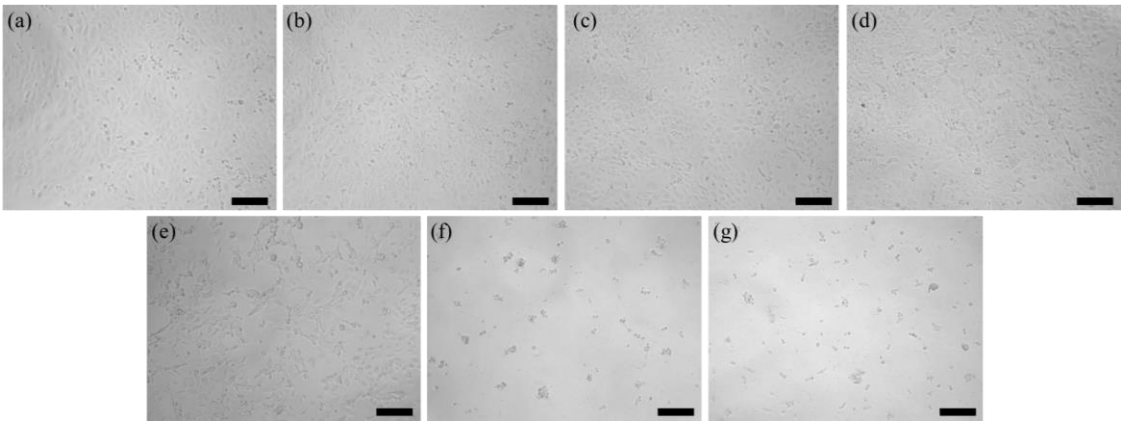

Figure 5.10 Optical images of ATDC 5 cells after 5-day culture with Fe^{3+}-GSH gel, (a) 0 µL (TCPs), (b) 5 µL, (c)10 µL, (d) 20 µL, (e) 30 µL, (f) 40 µL and (g) 50 µL per well. Scale bar, 100 µm.

The capability of the Fe^{3+}-GSH crosslinked hydrogels to inhibit proteolytic activity was then assessed, whereby MMP-13 was selected as a well-known upregulated protease in late-stage OA. By selecting MMP-13-supplemented aqueous solutions as a defined *in vitro* environment, incubation of Fe^{3+}-GSH hydrogel resulted in a reduction of MMP-13 activity after 12 hours (95.7±3.4%). A significant reduction in MMP-13 activity (92.9±1.4%) was recorded after 24 hours, compared to the positive control group ($p<0.001$) (Figure 5.11). On the other hand, no significant activity difference was observed between MMP-13-supplemented solutions and the same solutions following incubation with either soluble, complex-free GSH (103.1±7.6%) (215) or native HA at both time points (98.5±5.0%). In OSTENIL® PLUS, no reduction in MMP-13 activity was seen after 12 hours, but a significant reduction ($p<0.05$) in activity was observed after 24 hours (96.1±1.7%), with respect to the pristine MMP-13 solution. A comparison between the Fe^{3+}-GSH crosslinked gel and OSTENIL® PLUS reveals that increased MMP-13 inhibition occurred in the presence of the Fe^{3+}-GSH crosslinked hydrogel after 12 hours ($p<0.01$), which was maintained after 24 hours ($p<0.05$). These results provide indirect evidence that the hydrogel-induced

MMP-13 inhibition was achieved via chelation of respective iron sites with free sulfhydryl groups of active MMPs, rather than by complexation of the free zinc sites of active MMPs (225) with either the hydrogel's or GSH's sulfhydryl groups, on the one hand, or HA's carboxylic groups on the other hand. These observations support the key role played by the Fe^{3+}-GSH complex in both hydrogel crosslinking and MMP inhibition.

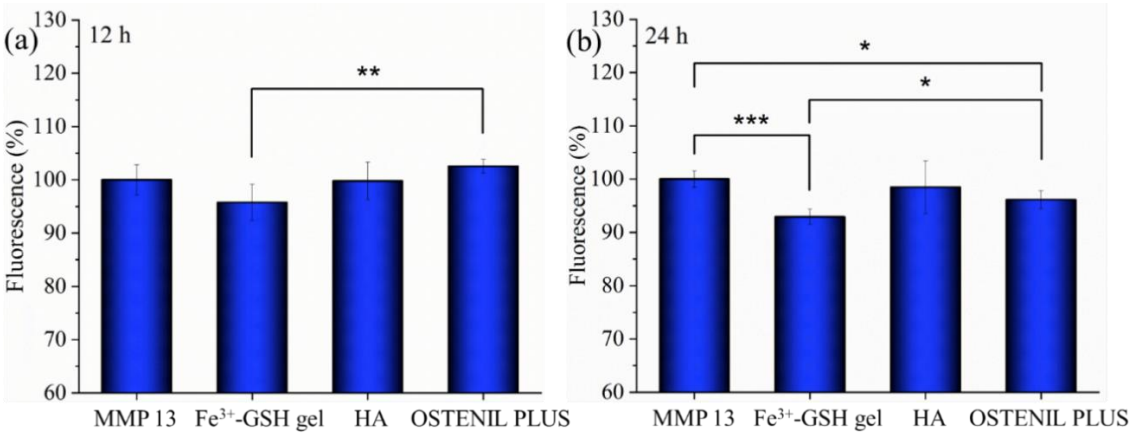

Figure 5.11 Variation of MMP-13 activity in MMP-13–supplemented solutions after 12-hour (a) and 24-hour (b) incubation with either the Fe^{3+}-GSH crosslinked hydrogel, an HA solution or the OSTENIL® PLUS commercial injection. Data was presented as Mean ± SD, statistical analysis was carried out between each two groups and labelled as *p≤ 0.05, **p≤ 0.01, ***p≤ 0.001, otherwise means no significant difference at p=0.05 level.

A sample of synovial fluid (S162) collected from patients with late-stage OA was used to investigate the MMP-regulating capability of the Fe^{3+}-GSH crosslinked gel in near-physiologic conditions, and to further corroborate the previous findings obtained for hydrogel-mediated MMP-13 inhibition in a defined *in vitro* environment. As the overall proteolytic activity was measured since various MMPs, including MMP-1, -2, -3, -7, -8, -9 and -13, were confirmed to have significantly increased activity in advanced OA.(203) Figure 5.12 reveals that

lower overall MMP activity and, smaller standard deviations, were observed for the Fe^{3+}-GSH crosslinked gel (81.0±7.5%) compared to the native SF group (100.0±17.6%), with a p-value of 0.0942. Although OSTENIL® PLUS presented a lower average value of activity reduction (92.3±27.3%) compared to native SF (p=0.6528), a larger standard deviation was recorded for this group versus both SF and the Fe^{3+}-GSH crosslinked gel. The results obtained with the clinical SF sample, therefore, confirm the competitive MMP inhibition functionality of the Fe^{3+}-GSH crosslinked hydrogel with respect to the OSTENIL® PLUS commercial control.

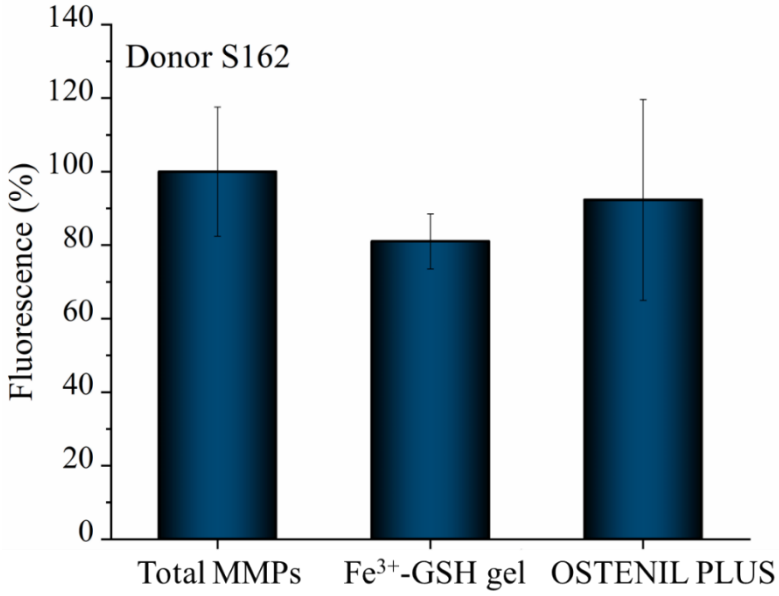

Figure 5.12 Variation of MMP activity recorded in a patient collected SF sample after 24-hour incubation with either the Fe^{3+}-GSH crosslinked hydrogel or the OSTENIL® PLUS commercial injection (n=4). The SF sample was collected from a patient (donor S162) with late-stage OA.

5.4 Conclusion

A Fe^{3+}-GSH crosslinked injectable hydrogel was prepared in this chapter that possessed self-healing and MMP inhibition functionalities. The coordination mechanism to yield the hydrogel was confirmed by shear frequency sweep tests,

which revealed a storage modulus more than ten times higher than the loss modulus. ^{57}Fe Mössbauer spectroscopy revealed that Fe was present in the hydrogel as octahedrally-coordinated Fe^{3+}. The hydrogel could hold up to 300% shear strain and presented a stable complex viscosity (37-42 → 12-16 Pa·s) after 10 cycling tests from low to high strain. *In vitro*, the gel proved to be well tolerated by ATDC 5 chondrocytes and able to support cell proliferation during a five day-culture. Furthermore, the gel demonstrated the inhibition of MMP activity after 24 hour-incubation in both an MMP-13–supplemented aqueous solution and a patient collected sample of synovial fluid, in light of the metal-coordinating reaction between thiol-complexed iron(III) and free sulfhydryl groups of active MMPs is exploited to induce MMP inhibition. These results therefore demonstrate that the hydrogel's biomechanical competence was successfully integrated with drug-free MMP regulation capability. The simple material design, together with the hydrogel's injectability and biochemical and self-healing functionalities support further development of this system for drug-free OA therapies.

Chapter 6

Summary and Future work

This project explored the influence of different crosslinking methods in the creation of hyaluronic acid-based hydrogels, aiming to create materials for the diagnosis or treatment of various diseases. Stiff, elastic, and self-healing hydrogels were reported dependent on the method of crosslinking used, which have potential to be applied to meet to a range of applications, and to act as scaffolds for the creation of a variety of new tissue types. .

Chapter 2 developed a chemical hydrogel that contained disulfide bonds (S-S) within the covalent crosslinks. Such a material is glutathione-responsive due to the dynamic redox reaction between S-S and -SH, which enabled a clear change material dimensions to be visualised when the material was incubated in simulated wound fluid with variable GSH concentrations. Consequently, this novel material may be used for clinical diagnosis to manage wounds by tracing the change of GSH levels.

In Chapter 3, progress in the application of acellular biomineralisation was made based on the previous cystamine crosslinked HA hydrogel reported in Chapter 2. Hydrogen phosphate interaction with crosslinked HA hydrogels was investigated, with the presence of hydrogen bonds forming secondary crosslinking network confirmed via DFT calculations and FTIR analysis. Hydroxyapatite crystal growth was realised in the entire HPO_4^{2-} and cystamine dual crosslinked HA hydrogel network. Mild and facile conditions may provide the possibility for *in vivo* mineralisation since the non-cytotoxic HPO_4^{2-} treatment was proved, particularly for prolonged gradient bone tissue regeneration.

Chapters 2 and 3 focused on chemical crosslinking methods to realise stable and stimuli-responsive hydrogels. The dynamic response to thiol-related molecules and obvious hydrogen phosphate interaction in cystamine crosslinked hydrogels in Chapters 2 and 3 revealed interesting phenomenon of HA-based materials that a cystamine crosslinked HA hydrogel can be designed and optimised via HPO_4^{2-} interaction with potential extended diseases applications, from chronic wound management to bone therapy.

Particularly, to further understand the interaction between HPO_4^{2-} groups and cystamine crosslinked HA molecules, systematic computational work in both interaction energy calculation and molecular dynamic simulation involving more factors such as the length of HA chain, pH influence, solvent and temperature effect, could help develop the mechanistic study.

The successful observation of gradient mineralisation in Chapter 3 achieved acellular controllable hydroxyapatite growing within a cystamine crosslinked hyaluronic acid network, which made it possible to realise controllable bone regeneration *in vivo*. However, it is unclear whether the existence of biomolecules such as amino acids and proteins could affect the process of biomineralisation *in vivo*. As clinical application is the final goal of this project, a study into the stability and reproducibility of the hydrogels in a physiologically-relevant environment must be determined as the next step. For example, adding the biomolecules stated above at appropriate concentrations to the c-SBF solution in which mineralisation happened. The metabolism of cells and response to bioactive substances, such as alkaline phosphatase, will be particularly important to determining hydrogel stability. Providing that biomineralisation occurs as expected under such conditions, a systematic combining of biological experiments and mechanical studies on mineralised hydrogels should be carried

out, including the proliferation, migration and differentiation of osteogenic cells, alkaline phosphatase expression during the mineralisation process and how bone density alters during this process.

Chapters 4 and 5 focused on physical crosslinking methods to achieve a flexible and self-healing network for joint tissue treatment, particularly cartilage injection for osteoarthritis therapy. As MMPs are highly expressed in OA diseases, a material that can facilitate a reduction in the activity of MMPs in OA was sought. In Chapter 4, a novel Iron(III)-glutathione (Fe^{3+}-GSH) complex was designed and reported, which was also the first time that such a complex being fabricated successfully in a straightforward manner while retaining an oxidative valence of Fe^{3+}. This Fe^{3+}-GSH complex revealed promising biomedical value, including significantly enhanced cell proliferation after 7 days and significant MMP-13 activity reduction *in vitro* after 24 hours and 48 hours in accordance with statistical analysis. The confirmed water-stable properties from initial 255±4 nm to 257±2 nm after 24 hours also suggested potential for *in vivo* use. The single crystal structure should be an important point to look at as future work for a better understanding in both chelation chemistry and MMP inhibition.

In Chapter 5, the Fe^{3+}-GSH complex that was fabricated in chapter 4 was applied as a novel crosslinker to yield physical and stretchable hydrogel network formed due to Fe^{3+} coordination to the carboxyl groups of HA. The biosafe dosage of the hydrogel was found by 5-day cell experiments that 5,000 ATDC 5 cells are tolerant to 0-30 µL gel. A statistically significant reduction in MMP-13 activity was observed under the biosafe dosage in hydrogel test group compared to both the MMP-13 control group in the absence of any additive, and the commercially available product OSTENIL® PLUS. When the gel was applied to clinical synovial

fluid sample collected from late-stage OA patient a reduced trend in MMP-13 activity was observed after 24 hours.

As the data obtained from clinical patient SF samples presented promising results, particularly in comparison with a commercial HA injection, further MMP inhibition tests with more clinical samples should be carried out for better statistical analysis. Furthermore, MMP expression by native cells in SF extracted from late-stage OA patients should be evaluated for a deeper understanding of the hydrogel inhibiting function on MMPs. Finally, animal tests in osteoarthritis models should be set up to study the function of the hydrogels in inflammation inhibition and cartilage repair. For example, inject this hydrogel into decayed cartilages of selected animals, the cartilage regeneration can be observed through μCT and histological staining. In the meantime, relative MMPs expression levels around treated tissues can be traced and recorded via Real-time Polymerase Chain Reaction (RT-PCR) during this experiment.

Although this project aimed to develop and succeeded in reporting a range of HA-based hydrogels, there remains a great deal of work worthy of further investigation. For example, it would be highly useful if chemical and physical crosslinked hydrogels could be combined to create a dual or multilayer material to realise bone repair and reduce inflammation simultaneously.

With biotechnology development, many difficulties have been conquered one by one. The advent of 3D printing technology may enable heart, lung, bone and many other organs to be created are no more problems for tissue replacement. However, in the meantime the development of dynamic naturally occurring substances to help regenerate tissue natively remains extremely valuable. Nowadays, 3D printing of natural biopolymer-based hydrogels is revealing its

potential in tissue engineering, which could also be something worth investigation as future work.

List of References

1. Wichterle, O. and Lím, D. 1960a. Hydrophilic Gels for Biological Use. *Nature*. **185**(4706), pp.117–118.
2. Gong, J.P. 2006. Friction and lubrication of hydrogels—its richness and complexity. *Soft Matter*. **2**(7), pp.544–552.
3. Highley, C.B., Prestwich, G.D. and Burdick, J.A. 2016. Recent advances in hyaluronic acid hydrogels for biomedical applications. *Current Opinion in Biotechnology*. **40**, pp.35–40.
4. Carvalho, S.M., Mansur, A.A.P., Capanema, N.S. V, Carvalho, I.C., Chagas, P., de Oliveira, L.C.A. and Mansur, H.S. 2018. Synthesis and in vitro assessment of anticancer hydrogels composed by carboxymethylcellulose-doxorubicin as potential transdermal delivery systems for treatment of skin cancer. *Journal of Molecular Liquids*. **266**, pp.425–440.
5. Wang, K. and Han, Z. 2017. Injectable hydrogels for ophthalmic applications. *Journal of Controlled Release*. **268**, pp.212–224.
6. Wang, L.L., Chung, J.J., Li, E.C., Uman, S., Atluri, P. and Burdick, J.A. 2018. Injectable and protease-degradable hydrogel for siRNA sequestration and triggered delivery to the heart. *Journal of Controlled Release*. **285**, pp.152–161.
7. Koehler, J., Brandl, F.P. and Goepferich, A.M. 2018. Hydrogel wound dressings for bioactive treatment of acute and chronic wounds. *European Polymer Journal*. **100**, pp.1–11.
8. Salama, A. 2018. Preparation of CMC-g-P(SPMA) super adsorbent hydrogels: Exploring their capacity for MB removal from waste water. *International Journal of Biological Macromolecules*. **106**, pp.940–946.

9. Qi, X., Wu, L., Su, T., Zhang, J. and Dong, W. 2018. Polysaccharide-based cationic hydrogels for dye adsorption. *Colloids and Surfaces B: Biointerfaces*. **170**, pp.364–372.

10. Dacrory, S., Abou-Yousef, H., Abouzeid, R.E., Kamel, S., Abdel-aziz, M.S. and El-badry, M. 2018. Antimicrobial cellulosic hydrogel from olive oil industrial residue. *International Journal of Biological Macromolecules*. **117**, pp.179–188.

11. Nakhjiri, M.T., Marandi, G.B. and Kurdtabar, M. 2018. Poly(AA-co-VPA) hydrogel cross-linked with N-maleyl chitosan as dye adsorbent: Isotherms, kinetics and thermodynamic investigation. *International Journal of Biological Macromolecules*. **117**, pp.152–166.

12. Stanciu, M.C. and Nichifor, M. 2018. Influence of dextran hydrogel characteristics on adsorption capacity for anionic dyes. *Carbohydrate Polymers*. **199**, pp.75–83.

13. Pathak, V.M. and Kumar, N. 2017. Dataset on the superabsorbent hydrogel synthesis with SiO2 nanoparticle and role in water restoration capability of agriculture soil. *Data in Brief*. **13**, pp.291–294.

14. Thombare, N., Mishra, S., Siddiqui, M.Z., Jha, U., Singh, D. and Mahajan, G.R. 2018. Design and development of guar gum based novel, superabsorbent and moisture retaining hydrogels for agricultural applications. *Carbohydrate Polymers*. **185**, pp.169–178.

15. Yan, S., Wang, Q., Tariq, Z., You, R., Li, X., Li, M. and Zhang, Q. 2018. Facile preparation of bioactive silk fibroin/hyaluronic acid hydrogels. *International Journal of Biological Macromolecules*. **118**, pp.775–782.

16. Kamoun, E.A., Abu-Saied, M.A., Doma, A.S., Menzel, H. and Chen, X. 2018. Influence of degree of substitution and folic acid coinitiator on

pullulan-HEMA hydrogel properties crosslinked under visible-light initiating system. *International Journal of Biological Macromolecules*. **116**, pp.1175–1185.

17. Dixit, A., Bag, D.S. and Kalra, S.J.S. 2017. Synthesis of strong and stretchable double network (DN) hydrogels of PVA-borax and P(AM-co-HEMA) and study of their swelling kinetics and mechanical properties. *Polymer*. **119**, pp.263–273.
18. Liu, D.E., Dursch, T.J., Taylor, N.O., Chan, S.Y., Bregante, D.T. and Radke, C.J. 2016. Diffusion of water-soluble sorptive drugs in HEMA/MAA hydrogels. *Journal of Controlled Release*. **239**, pp.242–248.
19. Chen, H., Xing, X., Tan, H., Jia, Y., Zhou, T., Chen, Y., Ling, Z. and Hu, X. 2017. Covalently antibacterial alginate-chitosan hydrogel dressing integrated gelatin microspheres containing tetracycline hydrochloride for wound healing. *Materials Science and Engineering: C*. **70**, pp.287–295.
20. Shariatinia, Z. and Jalali, A.M. 2018. Chitosan-based hydrogels: Preparation, properties and applications. *International Journal of Biological Macromolecules*. **115**, pp.194–220.
21. Fan, M., Ma, Y., Zhang, Z., Mao, J., Tan, H. and Hu, X. 2015. Biodegradable hyaluronic acid hydrogels to control release of dexamethasone through aqueous Diels–Alder chemistry for adipose tissue engineering. *Materials Science and Engineering: C*. **56**, pp.311–317.
22. Chung, T.-W., Chou, T.-H. and Wu, K.-Y. 2016. Gelatin/PLGA hydrogel films and their delivery of hydrophobic drugs. *Journal of the Taiwan Institute of Chemical Engineers*. **60**, pp.8–14.

23. Ermeydan, M.A. 2018. Modification of spruce wood by UV-crosslinked PEG hydrogels inside wood cell walls. *Reactive and Functional Polymers*. **131**, pp.100–106.

24. Kossover, O., Cohen, N., Lewis, J.A., Berkovitch, Y., Peled, E. and Seliktar, D. 2019. Growth Factor Delivery for the Repair of a Critical Size Tibia Defect Using an Acellular, Biodegradable Polyethylene Glycol-Albumin Hydrogel Implant. *ACS Biomaterials Science and Engineering*.

25. Lu, C., Wang, Y., Yang, S., Wang, C., Sun, X., Lu, J., Yin, H., Jiang, W., Meng, H., Rao, F., Wang, X. and Peng, J. 2018. Bioactive Self-Assembling Peptide Hydrogels Functionalized with Brain-Derived Neurotrophic Factor and Nerve Growth Factor Mimicking Peptides Synergistically Promote Peripheral Nerve Regeneration. *ACS Biomaterials Science and Engineering*. **4**(8), pp.2994–3005.

26. Zhao, N., Suzuki, A., Zhang, X., Shi, P., Abune, L., Coyne, J., Jia, H., Xiong, N., Zhang, G. and Wang, Y. 2019. Dual Aptamer-Functionalized in Situ Injectable Fibrin Hydrogel for Promotion of Angiogenesis via Codelivery of Vascular Endothelial Growth Factor and Platelet-Derived Growth Factor-BB. *ACS Applied Materials and Interfaces*. **11**(20), pp.18123–18132.

27. Hu, X., Wang, Y., Zhang, L., Xu, M., Zhang, J. and Dong, W. 2018. Design of a pH-sensitive magnetic composite hydrogel based on salecan graft copolymer and Fe3O4@SiO2 nanoparticles as drug carrier. *International Journal of Biological Macromolecules*. **107**, pp.1811–1820.

28. Hassan, M.M. 2018. Enhanced antimicrobial activity and reduced water absorption of chitosan films graft copolymerized with poly(acryloyloxy)ethyltrimethylammonium chloride. *International Journal of Biological Macromolecules*. **118**, pp.1685–1695.

29. Bao, X., Yu, L., Simon, G.P., Shen, S., Xie, F., Liu, H., Chen, L. and Zhong, L. 2018. Rheokinetics of graft copolymerization of acrylamide in concentrated starch and rheological behaviors and microstructures of reaction products. *Carbohydrate Polymers*. **192**, pp.1–9.

30. Zhang, W., Yang, Z., Kaufman, Y. and Bernstein, R. 2018. Surface and anti-fouling properties of a polyampholyte hydrogel grafted onto a polyethersulfone membrane. *Journal of Colloid and Interface Science*. **517**, pp.155–165.

31. Niu, J., Wang, J., Dai, X., Shao, Z. and Huang, X. 2018. Dual physically crosslinked healable polyacrylamide/cellulose nanofibers nanocomposite hydrogels with excellent mechanical properties. *Carbohydrate Polymers*. **193**, pp.73–81.

32. Yuan, N., Xu, L., Xu, B., Zhao, J. and Rong, J. 2018. Chitosan derivative-based self-healable hydrogels with enhanced mechanical properties by high-density dynamic ionic interactions. *Carbohydrate Polymers*. **193**, pp.259–267.

33. Feng, X., Yi, J., Zhang, W., Niu, Y. and Xu, L. 2019. A redox poly(ionic liquid) hydrogel: Facile method of synthesis and electrochemical sensing. *Journal of Applied Polymer Science*. **136**(42), pp.1–10.

34. Ye, X., Li, X., Shen, Y., Chang, G., Yang, J. and Gu, Z. 2017. Self-healing pH-sensitive cytosine- and guanosine-modified hyaluronic acid hydrogels via hydrogen bonding. *Polymer*. **108**, pp.348–360.

35. Chen, K., Chen, G., Wei, S., Yang, X., Zhang, D. and Xu, L. 2018. Preparation and property of high strength and low friction PVA-HA/PAA composite hydrogel using annealing treatment. *Materials Science and Engineering: C*. **91**, pp.579–588.

36. Owusu-Nkwantabisah, S., Gillmor, J., Bennett, G., Slater, G., Szakasits, M., Rajeswaran, M. and Antalek, B. 2018. Thermal stiffening of hydrophobic association hydrogels. *Polymer*. **145**, pp.374–381.

37. Deng, Y., Hussain, I., Kang, M., Li, K., Yao, F., Liu, S. and Fu, G. 2018. Self-recoverable and mechanical-reinforced hydrogel based on hydrophobic interaction with self-healable and conductive properties. *Chemical Engineering Journal*. **353**, pp.900–910.

38. An, R., Zhang, X., Han, L., Wang, X., Zhang, Y., Shi, L. and Ran, R. 2020. Healing, flexible, high thermal sensitive dual-network ionic conductive hydrogels for 3D linear temperature sensor. *Materials Science and Engineering C*. **107**(September 2019), p.110310.

39. Shi, Q., Liu, H., Tang, D., Li, Y., Li, X.J. and Xu, F. 2019. Bioactuators based on stimulus-responsive hydrogels and their emerging biomedical applications. *NPG Asia Materials*. **11**(1).

40. Piluso, S., Vukićević, R., Nöchel, U., Braune, S., Lendlein, A. and Neffe, A.T. 2018. Sequential alkyne-azide cycloadditions for functionalized gelatin hydrogel formation. *European Polymer Journal*. **100**, pp.77–85.

41. Fu, S., Dong, H., Deng, X., Zhuo, R. and Zhong, Z. 2017. Injectable hyaluronic acid/poly(ethylene glycol) hydrogels crosslinked via strain-promoted azide-alkyne cycloaddition click reaction. *Carbohydrate Polymers*. **169**, pp.332–340.

42. Le, X.T., Rioux, L.-E. and Turgeon, S.L. 2017. Formation and functional properties of protein–polysaccharide electrostatic hydrogels in comparison to protein or polysaccharide hydrogels. *Advances in Colloid and Interface Science*. **239**, pp.127–135.

43. Wang, S., Xu, Z., Wang, T., Liu, X., Lin, Y., Shen, Y.-Z., Lin, C. and Wang, L. 2018. Dramatically shrinking of hydrogels controlled by pillar[5]arene-based synergetic effect of host-guest recognition and electrostatic effect. *Journal of Photochemistry and Photobiology A: Chemistry*. **355**, pp.60–66.

44. Liu, H., Rong, L., Wang, B., Xie, R., Sui, X., Xu, H., Zhang, L., Zhong, Y. and Mao, Z. 2017. Facile fabrication of redox/pH dual stimuli responsive cellulose hydrogel. *Carbohydrate Polymers*. **176**, pp.299–306.

45. Gao, Y. and Dong, C.-M. 2018. Quadruple thermo-photo-redox-responsive random copolypeptide nanogel and hydrogel. *Chinese Chemical Letters*. **29**(6), pp.927–930.

46. Krisch, E., Gyarmati, B., Barczikai, D., Lapeyre, V., Szilágyi, B.Á., Ravaine, V. and Szilágyi, A. 2018. Poly(aspartic acid) hydrogels showing reversible volume change upon redox stimulus. *European Polymer Journal*. **105**, pp.459–468.

47. An, H., Xu, K., Chang, L., Wang, Y., Qin, J. and Li, W. 2018. Thermo-responsive self-healable hydrogels with extremely mild base degradability and bio-compatibility. *Polymer*. **147**, pp.38–47.

48. Wang, X., Chang, L., Hu, J., Lang, X., Fu, X., An, H., Wang, Y., Wang, H. and Qin, J. 2017. Self-healable hydrogels with crosslinking induced thermo-responsiveness and regulated properties from water soluble polymer. *Polymer*. **131**, pp.202–208.

49. Gao, C., Ren, J., Zhao, C., Kong, W., Dai, Q., Chen, Q., Liu, C. and Sun, R. 2016. Xylan-based temperature/pH sensitive hydrogels for drug controlled release. *Carbohydrate Polymers*. **151**, pp.189–197.

50. Zhu, L. and Bratlie, K.M. 2018. pH sensitive methacrylated chitosan hydrogels with tunable physical and chemical properties. *Biochemical Engineering Journal*. **132**, pp.38–46.

51. Chen, S.-C., Wu, Y.-C., Mi, F.-L., Lin, Y.-H., Yu, L.-C. and Sung, H.-W. 2004. A novel pH-sensitive hydrogel composed of N,O-carboxymethyl chitosan and alginate cross-linked by genipin for protein drug delivery. *Journal of Controlled Release*. **96**(2), pp.285–300.

52. Gong, J., Schuurmans, C.C.L., Genderen, A.M. van, Cao, X., Li, W., Cheng, F., He, J.J., López, A., Huerta, V., Manríquez, J., Li, R., Li, H., Delavaux, C., Sebastian, S., Capendale, P.E., Wang, H., Xie, J., Yu, M., Masereeuw, R., Vermonden, T. and Zhang, Y.S. 2020. Complexation-induced resolution enhancement of 3D-printed hydrogel constructs. *Nature Communications*. **11**(1), pp.1–14.

53. Gao, S., Ooka, R. and Oh, W. 2019. Formulation of human body heat transfer coefficient under various ambient temperature, air speed and direction based on experiments and CFD. *Building and Environment*. **160**(May), p.106168.

54. Shirkavand, A. and Nazif, H.R. 2019. Numerical study on the effects of blood perfusion and body metabolism on the temperature profile of human forearm in hyperthermia conditions. *Journal of Thermal Biology*. **84**(July), pp.339–350.

55. Chen, J.-P. and Cheng, T.-H. 2009. Preparation and evaluation of thermo-reversible copolymer hydrogels containing chitosan and hyaluronic acid as injectable cell carriers. *Polymer*. **50**(1), pp.107–116.

56. Montero-Rama, M.P., Liras, M., García, O. and Quijada-Garrido, I. 2015. Thermo- and pH-sensitive hydrogels functionalized with thiol groups. *European Polymer Journal*. **63**, pp.37–44.

57. Rosales, A.M., Rodell, C.B., Chen, M.H., Morrow, M.G., Anseth, K.S. and Burdick, J.A. 2018. Reversible Control of Network Properties in Azobenzene-Containing Hyaluronic Acid-Based Hydrogels. *Bioconjugate Chemistry*. **29**(4), pp.905–913.

58. Huang, K., Wu, H., Jiang, F., Shen, G. and Wang, L. 2018. On the near-infrared light-responsive and mechanical properties of PNIPAM-based nanocomposite hydrogels. *Polymer Degradation and Stability*. **156**, pp.228–233.

59. Deng, G., Li, F., Yu, H., Liu, F., Liu, C., Sun, W., Jiang, H. and Chen, Y. 2012. Dynamic Hydrogels with an Environmental Adaptive Self-Healing Ability and Dual Responsive Sol–Gel Transitions. *ACS Macro Letters*. **1**(2), pp.275–279.

60. Wang, L., Zhou, W., Wang, Q., Xu, C., Tang, Q. and Yang, H. 2018. An injectable, dual responsive, and self-healing hydrogel based on oxidized sodium alginate and hydrazide-modified poly (ethyleneglycol). *Molecules*. **23**(3).

61. Tan, H., Ramirez, C.M., Miljkovic, N., Li, H., Rubin, J.P. and Marra, K.G. 2009. Thermosensitive injectable hyaluronic acid hydrogel for adipose tissue engineering. *Biomaterials*. **30**(36), pp.6844–6853.

62. Zhu, S., Wang, J., Yan, H., Wang, Y., Zhao, Y., Feng, B., Duan, K. and Weng, J. 2017. An injectable supramolecular self-healing bio-hydrogel with high stretchability, extensibility and ductility, and a high swelling ratio. *Journal of Materials Chemistry B*. **5**(34), pp.7021–7034.

63. Dong, Y., Qin, Y., Dubaa, M., Killion, J., Gao, Y., Zhao, T., Zhou, D., Duscher, D., Geever, L., Gurtner, G.C. and Wang, W. 2015. A rapid crosslinking injectable hydrogel for stem cell delivery, from multifunctional hyperbranched polymers via RAFT homopolymerization of PEGDA. *Polymer Chemistry*. **6**(34), pp.6182–6192.

64. Ma, Y., Xin, L., Tan, H., Fan, M., Li, J., Jia, Y., Ling, Z., Chen, Y. and Hu, X. 2017. Chitosan membrane dressings toughened by glycerol to load antibacterial drugs for wound healing. *Materials Science and Engineering: C*. **81**, pp.522–531.

65. Liu, M., Zeng, X., Ma, C., Yi, H., Ali, Z., Mou, X., Li, S., Deng, Y. and He, N. 2017. Injectable hydrogels for cartilage and bone tissue engineering. *Bone Research*. **5**(1), p.17014.

66. Xu, Q., A, S., Gao, Y., Guo, L., Creagh-Flynn, J., Zhou, D., Greiser, U., Dong, Y., Wang, F., Tai, H., Liu, W., Wang, Wei and Wang, Wenxin 2018. A hybrid injectable hydrogel from hyperbranched PEG macromer as a stem cell delivery and retention platform for diabetic wound healing. *Acta Biomaterialia*. **75**, pp.63–74.

67. Khimji, I., Kelly, E.Y., Helwa, Y., Hoang, M. and Liu, J. 2013. Visual optical biosensors based on DNA-functionalized polyacrylamide hydrogels. *Methods*. **64**(3), pp.292–298.

68. Fusco, G., Chronopoulou, L., Galantini, L., Zerillo, A., Rasik, Z.M., Antiochia, R., Favero, G., D'Annibale, A., Palocci, C. and Mazzei, F. 2018. Evaluation of novel Fmoc-tripeptide based hydrogels as immobilization supports for electrochemical biosensors. *Microchemical Journal*. **137**, pp.105–110.

69. Li, G., Xiao, F., Liao, S., Chen, Q., Zhou, J., Wu, Z. and Yu, R. 2018. Label-free 2D colloidal photonic crystal hydrogel biosensor for urea and urease inhibitor. *Sensors and Actuators B: Chemical*. **277**, pp.591–597.

70. Agarwala, S., Lee, J.M., Ng, W.L., Layani, M., Yeong, W.Y. and Magdassi, S. 2018. A novel 3D bioprinted flexible and biocompatible hydrogel bioelectronic platform. *Biosensors and Bioelectronics*. **102**, pp.365–371.

71. Ding, H., Xin, Z., Yang, Y., Luo, Y., Xia, K., Wang, B., Sun, Y., Wang, J., Zhang, Y., Wu, H., Fan, S., Zhang, L. and Liu, K. 2020. Ultrasensitive, Low-Voltage Operational, and Asymmetric Ionic Sensing Hydrogel for Multipurpose Applications. *Advanced Functional Materials*. **30**(12), pp.1–10.

72. Hamedi, H., Moradi, S., Hudson, Samuel M and Tonelli, A.E. 2018. Chitosan based hydrogels and their applications for drug delivery in wound dressings: A review. *Carbohydrate Polymers*. **199**, pp.445–460.

73. Yegappan, R., Selvaprithiviraj, V., Amirthalingam, S. and Jayakumar, R. 2018. Carrageenan based hydrogels for drug delivery, tissue engineering and wound healing. *Carbohydrate Polymers*. **198**, pp.385–400.

74. Kupper, S., Kłosowska-Chomiczewska, I. and Szumała, P. 2017. Collagen and hyaluronic acid hydrogel in water-in-oil microemulsion delivery systems. *Carbohydrate Polymers*. **175**, pp.347–354.

75. Karimi, A.R., Rostaminejad, B., Rahimi, L., Khodadadi, A., Khanmohammadi, H. and Shahriari, A. 2018. Chitosan hydrogels cross-linked with tris(2-(2-formylphenoxy)ethyl)amine: Swelling and drug delivery. *International Journal of Biological Macromolecules*. **118**, pp.1863–1870.

76. Supramaniam, J., Adnan, R., Mohd Kaus, N.H. and Bushra, R. 2018. Magnetic nanocellulose alginate hydrogel beads as potential drug delivery system. *International Journal of Biological Macromolecules*. **118**, pp.640–648.

77. Gong, J., Katsuyama, Y., Kurokawa, T. and Osada, Y. 2003. Double-Network Hydrogels with extremely High Mechanical Strength. *Advanced Materials*. **15**, pp.1155–1158.

78. Ding, Y., Xu, X., Sharma, S., Floren, M., Stenmark, K., Bryant, S.J., Neu, C.P. and Tan, W. 2018. Biomimetic soft fibrous hydrogels for contractile and pharmacologically responsive smooth muscle. *Acta Biomaterialia*. **74**, pp.121–130.

79. Oryan, A., Jalili, M., Kamali, A. and Nikahval, B. 2018. The concurrent use of probiotic microorganism and collagen hydrogel/scaffold enhances burn wound healing: An in vivo evaluation. *Burns*. **44**(7), pp.1775–1786.

80. Yarimitsu, S., Sasaki, S., Murakami, T. and Suzuki, A. 2016. Evaluation of lubrication properties of hydrogel artificial cartilage materials for joint prosthesis. *Biosurface and Biotribology*. **2**(1), pp.40–47.

81. Walimbe, T., Panitch, A. and Sivasankar, P.M. 2017. A Review of Hyaluronic Acid and Hyaluronic Acid-based Hydrogels for Vocal Fold Tissue Engineering. *Journal of Voice*. **31**(4), pp.416–423.

82. Montalbano, G., Toumpaniari, S., Popov, A., Duan, P., Chen, J., Dalgarno, K., Scott, W.E. and Ferreira, A.M. 2018. Synthesis of bioinspired collagen/alginate/fibrin based hydrogels for soft tissue engineering. *Materials Science and Engineering: C*. **91**, pp.236–246.

83. Yang, J., Liu, Y., He, L., Wang, Q., Wang, L., Yuan, T., Xiao, Y., Fan, Y. and Zhang, X. 2018. Icariin conjugated hyaluronic acid/collagen hydrogel for osteochondral interface restoration. *Acta Biomaterialia*. **74**, pp.156–167.

84. Silva, C.R., Babo, P.S., Gulino, M., Costa, L., Oliveira, J.M., Silva-Correia, J., Domingues, R.M.A., Reis, R.L. and Gomes, M.E. 2018. Injectable and tunable hyaluronic acid hydrogels releasing chemotactic and angiogenic growth factors for endodontic regeneration. *Acta Biomaterialia*. **77**, pp.155–171.

85. Chen, F., Ni, Y., Liu, B., Zhou, T., Yu, C., Su, Y., Zhu, X., Yu, X. and Zhou, Y. 2017. Self-crosslinking and injectable hyaluronic acid/RGD-functionalized pectin hydrogel for cartilage tissue engineering. *Carbohydrate Polymers*. **166**, pp.31–44.

86. Kim, S.-H., Lee, S.-H., Lee, J.-E., Park, S.J., Kim, K., Kim, I.S., Lee, Y.-S., Hwang, N.S. and Kim, B.-G. 2018. Tissue adhesive, rapid forming, and sprayable ECM hydrogel via recombinant tyrosinase crosslinking. *Biomaterials*. **178**, pp.401–412.

87. Chen, C.-H., Chen, S.-H., Mao, S.-H., Tsai, M.-J., Chou, P.-Y., Liao, C.-H. and Chen, J.-P. 2017. Injectable thermosensitive hydrogel containing hyaluronic acid and chitosan as a barrier for prevention of postoperative peritoneal adhesion. *Carbohydrate Polymers*. **173**, pp.721–731.

88. Zhang, E., Li, J., Zhou, Y., Che, P., Ren, B., Qin, Z., Ma, L., Cui, J., Sun, H. and Yao, F. 2017. Biodegradable and injectable thermoreversible xyloglucan based hydrogel for prevention of postoperative adhesion. *Acta Biomaterialia*. **55**, pp.420–433.

89. Shalumon, K.T., Sheu, C., Chen, C.-H., Chen, S.-H., Jose, G., Kuo, C.-Y. and Chen, J.-P. 2018. Multi-functional electrospun antibacterial core-shell

nanofibrous membranes for prolonged prevention of post-surgical tendon adhesion and inflammation. *Acta Biomaterialia*. **72**, pp.121–136.

90. Xu, W., Qian, J., Zhang, Y., Suo, A., Cui, N., Wang, J., Yao, Y. and Wang, H. 2016. A double-network poly(Nε-acryloyl l-lysine)/hyaluronic acid hydrogel as a mimic of the breast tumor microenvironment. *Acta Biomaterialia*. **33**, pp.131–141.

91. Gwon, K., Kim, E. and Tae, G. 2017. Heparin-hyaluronic acid hydrogel in support of cellular activities of 3D encapsulated adipose derived stem cells. *Acta Biomaterialia*. **49**, pp.284–295.

92. Zhu, D., Wang, H., Trinh, P., Heilshorn, S.C. and Yang, F. 2017. Elastin-like protein-hyaluronic acid (ELP-HA) hydrogels with decoupled mechanical and biochemical cues for cartilage regeneration. *Biomaterials*. **127**, pp.132–140.

93. Feng, Q., Lin, S., Zhang, K., Dong, C., Wu, T., Huang, H., Yan, X., Zhang, L., Li, G. and Bian, L. 2017. Sulfated hyaluronic acid hydrogels with retarded degradation and enhanced growth factor retention promote hMSC chondrogenesis and articular cartilage integrity with reduced hypertrophy. *Acta Biomaterialia*. **53**, pp.329–342.

94. Balazs, E.A. 2004. Chapter 20 - Viscoelastic Properties of Hyaluronan and Its Therapeutic Use* *In*: H. G. Garg and C. A. B. T.-C. and B. of H. Hales, eds. *Chemistry and Biology of Hyaluronan* [Online]. Oxford: Elsevier Science Ltd, pp.415–455. Available from: http://www.sciencedirect.com/science/article/pii/B9780080443829500510.

95. Kuo, J.W. 2006. *Practical Aspects of Hyaluronan Based Medical Products* [Online] 1st Edition. Boca Raton: CRC Press. Available from: https://doi.org/10.1201/9781420037647.

96. Zhang, C., Dong, Q., Liang, K., Zhou, D., Yang, H., Liu, X., Xu, W., Zhou, Y. and Xiao, P. 2018. Photopolymerizable thiol-acrylate maleiated hyaluronic acid/thiol-terminated poly(ethylene glycol) hydrogels as potential in-situ formable scaffolds. *International Journal of Biological Macromolecules*. **119**, pp.270–277.

97. Lee, H.-Y., Hwang, C.-H., Kim, H.-E. and Jeong, S.-H. 2018. Enhancement of bio-stability and mechanical properties of hyaluronic acid hydrogels by tannic acid treatment. *Carbohydrate Polymers*. **186**, pp.290–298.

98. Gilarska, A., Lewandowska-Łańcucka, J., Horak, W. and Nowakowska, M. 2018.Deng, H., Dong, A., Song, J. and Chen, X. 2019. Injectable thermosensitive hydrogel systems based on functional PEG/PCL block polymer for local drug delivery. *Journal of Controlled Release*. **297**, pp.60–70.

99. Hamedi, H., Moradi, S., Hudson, Samuel M. and Tonelli, A.E. 2018. Chitosan based hydrogels and their applications for drug delivery in wound dressings: A review. *Carbohydrate Polymers*. **199**(March), pp.445–460.

100. Rivera-Delgado, E., Djuhadi, A., Danda, C., Kenyon, J., Maia, J., Caplan, A.I. and von Recum, H.A. 2018. Injectable liquid polymers extend the delivery of corticosteroids for the treatment of osteoarthritis. *Journal of Controlled Release*. **284**(May), pp.112–121.

101. Boardman, S.J., Lad, R., Green, D.C. and Thornton, P.D. 2017. Chitosan hydrogels for targeted dye and protein adsorption. *Journal of Applied Polymer Science*. **134**(21), pp.1–10.

102. Nicolson, P.C. and Vogt, J. 2001. Soft contact lens polymers: An evolution. *Biomaterials*. **22**(24), pp.3273–3283.

103. Moreddu, R., Vigolo, D. and Yetisen, A.K. 2019. Contact Lens Technology: From Fundamentals to Applications. *Advanced Healthcare Materials*. **8**(15), pp.1–24.

104. Wu, Y., Wang, H., Gao, F., Xu, Z., Dai, F. and Liu, W. 2018. An Injectable Supramolecular Polymer Nanocomposite Hydrogel for Prevention of Breast Cancer Recurrence with Theranostic and Mammoplastic Functions. *Advanced Functional Materials*. **28**(21), pp.1–12.

105. Jiang, X.J., Wang, T., Li, X.Y., Wu, D.Q., Zheng, Z. Bin, Zhang, J.F., Chen, J.L., Peng, B., Jiang, H., Huang, C. and Zhang, X.Z. 2009. Injection of a novel synthetic hydrogel preserves left ventricle function after myocardial infarction. *Journal of Biomedical Materials Research - Part A*. **90**(2), pp.472–477.

106. Zou, Y., Zhang, L., Yang, L., Zhu, F., Ding, M., Lin, F., Wang, Z. and Li, Y. 2018. “Click” chemistry in polymeric scaffolds: Bioactive materials for tissue engineering. *Journal of Controlled Release*. **273**(December 2017), pp.160–179.

107. Eslahi, N., Abdorahim, M. and Simchi, A. 2016. Smart Polymeric Hydrogels for Cartilage Tissue Engineering: A Review on the Chemistry and Biological Functions. *Biomacromolecules*. **17**(11), pp.3441–3463.

108. Holmes, R., Yang, X. Bin, Dunne, A., Florea, L., Wood, D. and Tronci, G. 2017. Thiol-ene photo-click collagen-PEG hydrogels: Impact of water-soluble photoinitiators on cell viability, gelation kinetics and rheological properties. *Polymers*. **9**(6).

109. Fu, J., Wiraja, C., Muhammad, H.B., Xu, C. and Wang, D.A. 2017. Improvement of endothelial progenitor outgrowth cell (EPOC)-mediated

vascularization in gelatin-based hydrogels through pore size manipulation. *Acta Biomaterialia*. **58**, pp.225–237.

110. Sadat Ebrahimi, M.M. and Schönherr, H. 2014. Enzyme-sensing chitosan hydrogels. *Langmuir*. **30**(26), pp.7842–7850.

111. Wang, F., Gao, W., Thamphiwatana, S., Luk, B.T., Angsantikul, P., Zhang, Q., Hu, C.M.J., Fang, R.H., Copp, J.A., Pornpattananangkul, D., Lu, W. and Zhang, L. 2015. Hydrogel retaining toxin-absorbing nanosponges for local treatment of methicillin-resistant Staphylococcus aureus infection. *Advanced Materials*. **27**(22), pp.3437–3443.

112. Jiang, X., Zhao, C., Fan, X., Xu, W., Zhang, R., Xu, H. and Wu, G. 2019. A DNA-modified hydrogel for simultaneous purification, concentration and detection of targeted cfDNA in human serum. *RSC Advances*. **9**(6), pp.3407–3415.

113. Patel, A., Lee, H.O., Jawerth, L., Maharana, S., Jahnel, M., Hein, M.Y., Stoynov, S., Mahamid, J., Saha, S., Franzmann, T.M., Pozniakovski, A., Poser, I., Maghelli, N., Royer, L.A., Weigert, M., Myers, E.W., Grill, S., Drechsel, D., Hyman, A.A. and Alberti, S. 2015. A Liquid-to-Solid Phase Transition of the ALS Protein FUS Accelerated by Disease Mutation. *Cell*. **162**(5), pp.1066–1077.

114. Zheng, Y., Wang, X., Ji, S., Tian, S., Wu, H., Luo, P., Fang, H., Wang, L., Wu, G., Xiao, S. and Xia, Z. 2016. Mepenzolate bromide promotes diabetic wound healing by modulating inflammation and oxidative stress. *American Journal of Translational Research*. **8**(6), pp.2738–2747.

115. Hasmann, A., Wehrschuetz-Sigl, E., Marold, A., Wiesbauer, H., Schoeftner, R., Gewessler, U., Kandelbauer, A., Schiffer, D., Schneider, K.P., Binder, B., Schintler, M. and Guebitz, G.M. 2013. Analysis of myeloperoxidase

activity in wound fluids as a marker of infection. *Annals of Clinical Biochemistry*. **50**(3), pp.245–254.

116. Hasmann, A., Gewessler, U., Hulla, E., Schneider, K.P., Binder, B., Francesko, A., Tzanov, T., Schintler, M., Van der Palen, J., Guebitz, G.M. and Wehrschuetz-Sigl, E. 2011. Sensor materials for the detection of human neutrophil elastase and cathepsin G activity in wound fluid. *Experimental Dermatology*. **20**(6), pp.508–513.

117. Rayahin, J.E., Buhrman, J.S., Zhang, Y., Koh, T.J. and Gemeinhart, R.A. 2015. High and Low Molecular Weight Hyaluronic Acid Differentially Influence Macrophage Activation. *ACS Biomaterials Science and Engineering*. **1**(7), pp.481–493.

118. Volpi, N., Schiller, J. and Soltes, R.S. and L. 2009. Role, Metabolism, Chemical Modifications and Applications of Hyaluronan. *Current Medicinal Chemistry*. **16**(14), pp.1718–1745.

119. Jung, Y. seok, Park, W., Park, H., Lee, D.K. and Na, K. 2017. Thermo-sensitive injectable hydrogel based on the physical mixing of hyaluronic acid and Pluronic F-127 for sustained NSAID delivery. *Carbohydrate Polymers*. **156**, pp.403–408.

120. Ouasti, S., Donno, R., Cellesi, F., Sherratt, M.J., Terenghi, G. and Tirelli, N. 2011. Network connectivity, mechanical properties and cell adhesion for hyaluronic acid/PEG hydrogels. *Biomaterials*. **32**(27), pp.6456–6470.

121. Patterson, J., Siew, R., Herring, S.W., Lin, A.S.P., Guldberg, R. and Stayton, P.S. 2010. Hyaluronic acid hydrogels with controlled degradation properties for oriented bone regeneration. *Biomaterials*. **31**(26), pp.6772–6781.

122. Kim, I.L., Mauck, R.L. and Burdick, J.A. 2011. Hydrogel design for cartilage tissue engineering: A case study with hyaluronic acid. *Biomaterials*. **32**(34), pp.8771–8782.

123. Cui, F.Z., Tian, W.M., Hou, S.P., Xu, Q.Y. and Lee, I.S. 2006. Hyaluronic acid hydrogel immobilized with RGD peptides for brain tissue engineering. *Journal of Materials Science: Materials in Medicine*. **17**(12), pp.1393–1401.

124. Dahlmann, J., Krause, A., Möller, L., Kensah, G., Möwes, M., Diekmann, A., Martin, U., Kirschning, A., Gruh, I. and Dräger, G. 2013. Fully defined in situ cross-linkable alginate and hyaluronic acid hydrogels for myocardial tissue engineering. *Biomaterials*. **34**(4), pp.940–951.

125. Hsiao, M.Y., Lin, A.C., Liao, W.H., Wang, T.G., Hsu, C.H., Chen, W.S. and Lin, F.H. 2019. Drug-loaded hyaluronic acid hydrogel as a sustained-release regimen with dual effects in early intervention of tendinopathy. *Scientific Reports*. **9**(1), pp.1–9.

126. Ying, H., Zhou, J., Wang, M., Su, D., Ma, Q., Lv, G. and Chen, J. 2019. In situ formed collagen-hyaluronic acid hydrogel as biomimetic dressing for promoting spontaneous wound healing. *Materials Science and Engineering C*. **101**(March), pp.487–498.

127. Zhu, J., Li, F., Wang, X., Yu, J. and Wu, D. 2018. Hyaluronic Acid and Polyethylene Glycol Hybrid Hydrogel Encapsulating Nanogel with Hemostasis and Sustainable Antibacterial Property for Wound Healing. *ACS Applied Materials and Interfaces*. **10**(16), pp.13304–13316.

128. Cai, Z., Zhang, H., Wei, Y., Wu, M. and Fu, A. 2019. Shear-thinning hyaluronan-based fluid hydrogels to modulate viscoelastic properties of osteoarthritis synovial fluids. *Biomaterials Science*. **7**(8), pp.3143–3157.

129. Yuan, Z., Zakhaleva, J., Ren, H., Liu, J., Chen, W. and Pan, Y. 2009. Noninvasive and High-Resolution Optical Monitoring of Healing of Diabetic Dermal Excisional Wounds Implanted with Biodegradable In Situ Gelable Hydrogels. *Tissue Engineering Part C: Methods*. **16**(2), pp.237–247.

130. Deponte, M. 2013. Glutathione catalysis and the reaction mechanisms of glutathione-dependent enzymes. *Biochimica et Biophysica Acta - General Subjects*. **1830**(5), pp.3217–3266.

131. McAvan, B.S., Khuphe, M. and Thornton, P.D. 2017. Polymer hydrogels for glutathione-mediated protein release. *European Polymer Journal*. **87**, pp.468–477.

132. Wu, C., Belenda, C., Leroux, J.-C. and Gauthier, M.A. 2011. Interplay of Chemical Microenvironment and Redox Environment on Thiol–Disulfide Exchange Kinetics. *Chemistry – A European Journal*. **17**(36), pp.10064–10070.

133. MUDGE, B.P., HARRIS, C., GILMONT, R.R., ADAMSON, B.S. and REES, R.S. 2002. Role of glutathione redox dysfunction in diabetic wounds. *Wound Repair and Regeneration*. **10**(1), pp.52–58.

134. Tronci, G., Yin, J., Holmes, R.A., Liang, H., Russell, S.J. and Wood, D.J. 2016. Protease-sensitive atelocollagen hydrogels promote healing in a diabetic wound model. *Journal of Materials Chemistry B*. **4**(45), pp.7249–7258.

135. Liang, H., Russell, S.J., Wood, D.J. and Tronci, G. 2018. Monomer-Induced Customization of UV-Cured Atelocollagen Hydrogel Networks. *Frontiers in Chemistry*. **6**, p.626.

136. Percival, S.L., Slone, W., Linton, S., Okel, T., Corum, L. and Thomas, J.G. 2011. Use of flow cytometry to compare the antimicrobial efficacy of silver-

containing wound dressings against planktonic Staphylococcus aureus and Pseudomonas aeruginosa. *Wound Repair and Regeneration*. **19**(3), pp.436–441.

137. Xie, J.Y., Li, C.Y., Li, Y.F., Fei, J., Xu, F., Ou-Yang, J. and Liu, J. 2016. Near-Infrared Fluorescent Probe with High Quantum Yield and Its Application in the Selective Detection of Glutathione in Living Cells and Tissues. *Analytical Chemistry*. **88**(19), pp.9746–9752.

138. Dernek, B., Duymus, T.M., Koseoglu, P.K., Aydin, T., Kesiktas, F.N., Aksoy, C. and Mutlu, S. 2016. Efficacy of single-dose hyaluronic acid products with two different structures in patients with early-stage knee osteoarthritis. *Journal of Physical Therapy Science*. **28**(11), pp.3036–3040.

139. Dernek, B., Kesiktas, F.N., Duymus, T.M., Diracoglu, D. and Aksoy, C. 2017. Therapeutic efficacy of three hyaluronic acid formulations in young and middle-aged patients with early-stage meniscal injuries. *Journal of Physical Therapy Science*. **29**(7), pp.1148–1153.

140. Chen, H., Cheng, R., Zhao, X., Zhang, Y., Tam, A., Yan, Y., Shen, H., Zhang, Y.S., Qi, J., Feng, Y., Liu, L., Pan, G., Cui, W. and Deng, L. 2019. An injectable self-healing coordinative hydrogel with antibacterial and angiogenic properties for diabetic skin wound repair. *NPG Asia Materials*. **11**(1).

141. Stapleton, L.M., Steele, A.N., Wang, H., Lopez Hernandez, H., Yu, A.C., Paulsen, M.J., Smith, A.A.A., Roth, G.A., Thakore, A.D., Lucian, H.J., Totherow, K.P., Baker, S.W., Tada, Y., Farry, J.M., Eskandari, A., Hironaka, C.E., Jaatinen, K.J., Williams, K.M., Bergamasco, H., Marschel, C., Chadwick, B., Grady, F., Ma, M., Appel, E.A. and Woo, Y.J. 2019. Use of a supramolecular polymeric hydrogel as an effective post-operative

pericardial adhesion barrier. *Nature Biomedical Engineering*. **3**(8), pp.611–620.

142. Bukhari, S.N.A., Roswandi, N.L., Waqas, M., Habib, H., Hussain, F., Khan, S., Sohail, M., Ramli, N.A., Thu, H.E. and Hussain, Z. 2018. Hyaluronic acid, a promising skin rejuvenating biomedicine: A review of recent updates and pre-clinical and clinical investigations on cosmetic and nutricosmetic effects. *International Journal of Biological Macromolecules*. **120**, pp.1682–1695.

143. Yoshida, N., Naito, Y., Kugai, M., Inoue, K., Uchiyama, K., Takagi, T., Ishikawa, T., Handa, O., Konishi, H., Wakabayashi, N., Yagi, N., Kokura, S., Morimoto, Y., Kanemasa, K., Yanagisawa, A. and Yoshikawa, T. 2011. Efficacy of hyaluronic acid in endoscopic mucosal resection of colorectal tumors. *Journal of Gastroenterology and Hepatology (Australia)*. **26**(2), pp.286–291.

144. Zhao, C., Hashimoto, T., Kirk, R.L., Thoreson, A.R., Jay, G.D., Moran, S.L., An, K.N. and Amadio, P.C. 2013. Resurfacing with chemically modified hyaluronic acid and lubricin for flexor tendon reconstruction. *Journal of Orthopaedic Research*. **31**(6), pp.969–975.

145. Taguchi, M., Zhao, C., Sun, Y.L., Jay, G.D., An, K.N. and Amadio, P.C. 2009. The Effect of Surface Treatment Using Hyaluronic Acid and Lubricin on the Gliding Resistance of Human Extrasynovial Tendons In Vitro. *Journal of Hand Surgery*. **34**(7), pp.1276–1281.

146. Jeong, S.H., Koh, Y.H., Kim, S.W., Park, J.U., Kim, H.E. and Song, J. 2016. Strong and Biostable Hyaluronic Acid-Calcium Phosphate Nanocomposite Hydrogel via in Situ Precipitation Process. *Biomacromolecules*. **17**(3), pp.841–851.

147. Faruq, O., Kim, B., Padalhin, A.R., Lee, G.H. and Lee, B.T. 2017a. A hybrid composite system of biphasic calcium phosphate granules loaded with hyaluronic acid-gelatin hydrogel for bone regeneration. *Journal of Biomaterials Applications*. **32**(4), pp.433–445.

148. Daly, A.C., Riley, L., Segura, T. and Burdick, J.A. 2020. Hydrogel microparticles for biomedical applications. *Nature Reviews Materials*. **5**(1), pp.20–43.

149. Rosales, A.M. and Anseth, K.S. 2016. The design of reversible hydrogels to capture extracellular matrix dynamics. *Nature Reviews Materials*. **1**(2), pp.1–15.

150. He, Q., Huang, Y. and Wang, S. 2018. Hofmeister Effect-Assisted One Step Fabrication of Ductile and Strong Gelatin Hydrogels. *Advanced Functional Materials*. **28**(5).

151. He, Q., Huang, D., Yang, J., Huang, Y. and Wang, S. 2019. Dual Cross-Link Networks to Preserve Physical Interactions Induced by Soaking Methods: Developing a Strong and Biocompatible Protein-Based Hydrogel. *ACS Applied Bio Materials*. **2**(8), pp.3352–3361.

152. Long, F.A. and McDevit, W.F. 1952. Activity coefficients of nonelectrolyte solutes in aqueous salt solutions. *Chemical Reviews*. **51**(1), pp.119–169.

153. Corridoni, T., Mancinelli, R., Ricci, M.A., Bruni, F. and Amaldi, F.E. 2011. Viscosity of Aqueous Solutions and Local Microscopic Structure. *The Journal of Physical Chemistry B*. **115**(48), pp.14008–14013.

154. Zangi, R. 2010. Can Salting-In Salting-Out Ions be Classified as Chaotropes Kosmotropes.pdf. *The Journal of Physical Chemistry B*. **114**(1), pp.643–650.

155. Casanova-morales, N., Alavi, Z., Wilson, C.A.M. and Zocchi, G. 2018. Identifying Chaotropic and Kosmotropic Agents by Nanorheology. *The Journal of Physical Chemistry B*. **122**(14), pp.3754–3759.

156. BARRETT, T.W. 1981. Solution Properties of Hyaluronic Acid. *ACS Symposium Series; American Chemical Society: Washington, DC*., pp.229–250.

157. Borgogna, M., Skjåk-Bræk, G., Paoletti, S. and Donati, I. 2013. On the initial binding of alginate by calcium ions. the tilted egg-box hypothesis. *Journal of Physical Chemistry B*. **117**(24), pp.7277–7282.

158. Fang, Y., Al-Assaf, S., Phillips, G.O., Nishinari, K., Funami, T., Williams, P.A. and Li, A. 2007. Multiple steps and critical behaviors of the binding of calcium to alginate. *Journal of Physical Chemistry B*. **111**(10), pp.2456–2462.

159. Potiwiput, S., Tan, H., Yuan, G., Li, S., Zhou, T., Li, J., Jia, Y., Xiong, D., Hu, X., Ling, Z. and Chen, Y. 2019. Dual-crosslinked Alginate/Carboxymethyl Chitosan Hydrogel Containing in situ Synthesized Calcium Phosphate Particles for Drug Delivery Application. *Materials Chemistry and Physics*., p.122354.

160. Kauzmann, W. and Simpson, R.B. 1953. The Kinetics of Protein Denaturation. III. The Optical Rotations of Serum Albumin, β-Lactoglobulin and Pepsin in Urea Solutions. *Journal of the American Chemical Society*. **75**(21), pp.5154–5157.

161. Jeong, S.H., Sun, J.Y. and Kim, H.E. 2017. Dual-Crosslinking of Hyaluronic Acid–Calcium Phosphate Nanocomposite Hydrogels for Enhanced Mechanical Properties and Biological Performance. *Macromolecular Materials and Engineering*. **302**(10), pp.1–6.

162. Brenner, E.K., Schiffman, J.D., Toth, L.J., Szewczyk, J.C. and Schauer, C.L. 2013. Phosphate salts facilitate the electrospinning of hyaluronic acid fiber mats. *Journal of Materials Science*. **48**(22), pp.7805–7811.

163. Kauzmann, W. 1959. SOME FACTORS IN THE INTERPRETATION OF PROTEIN DENATURATION ’. *Advances in Protein Chemistry*. **14**(C), pp.1–63.

164. Herzog, M., Li, L., Galla, H.J. and Winter, R. 2019. Effect of hyaluronic acid on phospholipid model membranes. *Colloids and Surfaces B: Biointerfaces*. **173**(September 2018), pp.327–334.

165. Zhu, L., Luo, D. and Liu, Y. 2020. Effect of the nano/microscale structure of biomaterial scaffolds on bone regeneration. *International Journal of Oral Science*. **12**(1), pp.1–15.

166. Li, Z., Su, Y., Xie, B., Wang, H., Wen, T., He, C., Shen, H., Wu, D. and Wang, D. 2013. A tough hydrogel-hydroxyapatite bone-like composite fabricated in situ by the electrophoresis approach. *Journal of Materials Chemistry B*. **1**(12), pp.1755–1764.

167. Dorvee, J.R., Boskey, A.L. and Estroff, L.A. 2012. Rediscovering hydrogel-based double-diffusion systems for studying biomineralization. *CrystEngComm*. **14**(18), pp.5681–5700.

168. Elsharkawy, S. and Mata, A. 2018. Hierarchical Biomineralization: from Nature’s Designs to Synthetic Materials for Regenerative Medicine and Dentistry. *Advanced Healthcare Materials*.

169. Gao, Z., Golland, B., Tronci, G. and Thornton, P.D. 2019. A redox-responsive hyaluronic acid-based hydrogel for chronic wound management. *Journal of Materials Chemistry B*. **7**(47), pp.7494–7501.

170. Oyane, A., Kim, H.-M., Furuya, T., Kokubo, T., Miyazaki, T. and Nakamura, T. 2003. Preparation and assessment of revised simulated body fluids. *Journal of Biomedical Materials Research Part A*. **65A**(2), pp.188–195.

171. Frisch, M.J., Trucks, G.W., Schlegel, H.B., Scuseria, G.E., Robb, M.A., Cheeseman, J.R., Scalmani, G., Barone, V., Petersson, G.A., Nakatsuji, H., Li, X., Caricato, M., Marenich, A. V., Bloino, J., Janesko, B.G., Gomperts, R., Mennucci, B., Hratchian, H.P., Ortiz, J. V., Izmaylov, A.F., Sonnenberg, J.L., Williams-Young, D., Ding, F., Lipparini, F., Egidi, F., Goings, J., Peng, B., Petrone, A., Henderson, T., Ranasinghe, D., Zakrzewski, V.G., Gao, J., Rega, N., Zheng, G., Liang, W., Hada, M., Ehara, M., Toyota, K., Fukuda, R., Hasegawa, J., Ishida, M., Nakajima, T., Honda, Y., Kitao, O., Nakai, H., Vreven, T., Throssell, K., Montgomery, J.A., Jr., Peralta, J.E., Ogliaro, F., Bearpark, M.J., Heyd, J.J., Brothers, E.N., Kudin, K.N., Staroverov, V.N., Keith, T.A., Kobayashi, R., Normand, J., Raghavachari, K., Rendell, A.P., Burant, J.C., Iyengar, S.S., Tomasi, J., Cossi, M., Millam, J.M., Klene, M., Adamo, C., Cammi, R., Ochterski, J.W., Martin, R.L., Morokuma, K., Farkas, O., Foresman, J.B. and Fox, D.J. 2016. Gaussian 16, Revision A.03, Gaussian, Inc., Wallingford CT.

172. Tessier, H. and Rose, D. 1958. Calcium Ion Concentration in Milk. *Journal of Dairy Science*. **41**(3), pp.351–359.

173. Jensen, E. V 1959. This biological chain reaction explains. *Science*. **130**(3385), pp.1319–1323.

174. Brundavanam, R.K., Poinern, G.E.J. and Fawcett, D. 2013. Modelling the Crystal Structure of a 30 nm Sized Particle based Hydroxyapatite Powder Synthesised under the Influence of Ultrasound Irradiation from X-ray

powder Diffraction Data. *American Journal of M aterials Science*. **2013**(4), pp.84–90.

175. Xia, T., Liu, W. and Yang, L. 2017. A review of gradient stiffness hydrogels used in tissue engineering and regenerative medicine. *Journal of Biomedical Materials Research - Part A*. **105**(6), pp.1799–1812.

176. Dharmaraja, A.T. 2017. Role of Reactive Oxygen Species (ROS) in Therapeutics and Drug Resistance in Cancer and Bacteria. *Journal of Medicinal Chemistry*. **60**(8), pp.3221–3240.

177. Sagar, S., Kallo, I.J., Kaul, N., Ganguly, N.K. and Sharma, B.K. 1992. Oxygen free radicals in essential hypertension. *Molecular and Cellular Biochemistry*. **111**(1–2), pp.103–108.

178. Beeh, K.M., Beier, J., Haas, I.C., Kornmann, O., Micke, P. and Buhl, R. 2002. Glutathione deficiency of the lower respiratory tract in patients with idiopathic pulmonary fibrosis. *European Respiratory Journal*. **19**(6), pp.1119–1123.

179. Herzenberg, Leonore A., De Rosa, S.C., Dubs, J.G., Roederer, M., Anderson, M.T., Ela, S.W., Deresinski, S.C. and Herzenberg, Leonard A. 1997. Glutathione deficiency is associated with impaired survival in HIV disease. *Proceedings of the National Academy of Sciences of the United States of America*. **94**(5), pp.1967–1972.

180. Pacht, E.R., Timerman, A.P., Lykens, M.G. and Merola, J. 1991. Deficiency of Alveolar Fluid Glutathione in Patients with Sepsis and the Adult Respiratory Distress Syndrome. *Chest*. **100**(5), pp.1397–1403.

181. Wendel, A. and Cikryt, P. 1980. The level and half-life of glutathione in human plasma. *FEBS Letters*. **120**(2), pp.209–211.

182. Yruela, I. 2013. Transition metals in plant photosynthesis. *Metallomics*. **5**(9), pp.1090–1109.

183. Waldron, K.J., Rutherford, J.C., Ford, D. and Robinson, N.J. 2009. Metalloproteins and metal sensing. *Nature*. **460**(7257), pp.823–830.

184. Betanzos-Lara, S., Chmel, N.P., Zimmerman, M.T., Barrón-Sosa, L.R., Garino, C., Salassa, L., Rodger, A., Brumaghim, J.L., Gracia-Mora, I. and Barba-Behrens, N. 2015. Redox-active and DNA-binding coordination complexes of clotrimazole. *Dalton Transactions*. **44**(8), pp.3673–3685.

185. Miao, Y., Xie, F., Cen, J., Zhou, F., Tao, X., Luo, J., Han, G., Kong, X., Yang, X., Sun, J. and Ling, J. 2018. Fe3+@polyDOPA- b-polysarcosine, a T1-Weighted MRI Contrast Agent via Controlled NTA Polymerization. *ACS Macro Letters*. **7**(6), pp.693–698.

186. Wang, H., Jordan, V.C., Ramsay, I.A., Sojoodi, M., Fuchs, B.C., Tanabe, K.K., Caravan, P. and Gale, E.M. 2019. Molecular Magnetic Resonance Imaging Using a Redox-Active Iron Complex. *Journal of the American Chemical Society*. **141**(14), pp.5916–5925.

187. Bramanti, E., D'Ulivo, A., Lampugnani, L., Raspi, G. and Zamboni, R. 1999. Cold vapour atomic fluorescence studies on the behaviour of mercury (II) and mercury (II)-thiol complexes. An alternative route for characterization of -SH binding groups. *Journal of Analytical Atomic Spectrometry*. **14**(2), pp.179–185.

188. Ma, Y.F., Wang, L.J., Zhou, Y.L. and Zhang, X.X. 2019. A facilely synthesized glutathione-functionalized silver nanoparticle-grafted covalent organic framework for rapid and highly efficient enrichment of N-linked glycopeptides. *Nanoscale*. **11**(12), pp.5526–5534.

189. Fang, A., Chen, H., Li, H., Liu, M., Zhang, Y. and Yao, S. 2017. Glutathione regulation-based dual-functional upconversion sensing-platform for acetylcholinesterase activity and cadmium ions. *Biosensors and Bioelectronics*. **87**, pp.545–551.

190. Gelinsky, M., Vogler, R. and Vahrenkamp, H. 2003. Zinc complexation of glutathione and glutathione-derived peptides. *Inorganica Chimica Acta*. **344**, pp.230–238.

191. Chu, W., Zhang, Y., Li, D., Barrow, C.J., Wang, H. and Yang, W. 2015. A biomimetic sensor for the detection of lead in water. *Biosensors and Bioelectronics*. **67**, pp.621–624.

192. Qi, W., Li, J., Chain, C.Y., Pasquevich, G.A., Pasquevich, A.F. and Cowan, J.A. 2012. Glutathione Complexed Fe–S Centers. *Journal of the American Chemical Society*. **134**(26), pp.10745–10748.

193. Qi, W., Li, J., Chain, C.Y., Pasquevich, G.A., Pasquevich, A.F. and Cowan, J.A. 2013. Glutathione-complexed iron-sulfur clusters. Reaction intermediates and evidence for a template effect promoting assembly and stability. *Chemical Communications*. **49**(57), pp.6313–6315.

194. Hamed, M.Y., Silver, J. and Wilsonx, M.T. 1983. Studies of the reactions of ferric iron with glutathione and some related thiols. *Inorganica Chimica Acta*. **78**(C), pp.1–11.

195. Hider, R.C. and Kong, X.L. 2011. Glutathione: A key component of the cytoplasmic labile iron pool. *BioMetals*. **24**(6), pp.1179–1187.

196. Gervason, S., Larkem, D., Mansour, A. Ben, Botzanowski, T., Müller, C.S., Pecqueur, L., Le Pavec, G., Delaunay-Moisan, A., Brun, O., Agramunt, J., Grandas, A., Fontecave, M., Schünemann, V., Cianférani, S., Sizun, C., Tolédano, M.B. and D'Autréaux, B. 2019. Physiologically relevant

reconstitution of iron-sulfur cluster biosynthesis uncovers persulfide-processing functions of ferredoxin-2 and frataxin. *Nature Communications*. **10**(1), pp.1–12.

197. Bonfio, C., Valer, L., Scintilla, S., Shah, S., Evans, D.J., Jin, L., Szostak, J.W., Sasselov, D.D., Sutherland, J.D. and Mansy, S.S. 2017. UV-light-driven prebiotic synthesis of iron-sulfur clusters. *Nature Chemistry*. **9**(12), pp.1229–1234.

198. Dyar, M.D., Agresti, D.G., Schaefer, M.W., Grant, C.A. and Sklute, E.C. 2006. Mössbauer Spectroscopy of Earth and Planetary Materials. *Annual Review of Earth and Planetary Sciences*. **34**(1), pp.83–125.

199. Liliana, Q. and Lina, R.-A. 2013. Studying Metal Ion-Protein Interactions:Electronic Absorption, Circular Dichroism, and Electron Paramagnetic Resonance In: Williams M., Daviter T. (eds) *Protein-Ligand Interactions. Methods in Molecular Biology (Methods and Protocols)*. Vol **1008**. Humana Press, Totowa, NJ, pp.267–297.

200. Mekaru, H., Yoshigoe, A., Nakamura, M., Doura, T. and Tamanoi, F. 2019. Biodegradability of Disulfide-Organosilica Nanoparticles Evaluated by Soft X-ray Photoelectron Spectroscopy: Cancer Therapy Implications. *ACS Applied Nano Materials*. **2**(1), pp.479–488.

201. Wang, X., Xiang, Q., Liu, B., Wang, L., Luo, T., Chen, D. and Shen, G. 2013. TiO2 modified FeS Nanostructures with Enhanced Electrochemical Performance for Lithium-Ion Batteries. *Scientific Reports*. **3**, p.2007.

202. Grosvenor, A.P., Kobe, B.A., Biesinger, M.C. and McIntyre, N.S. 2004. Investigation of multiplet splitting of Fe 2p XPS spectra and bonding in iron compounds. *Surface and Interface Analysis*. **36**(12), pp.1564–1574.

203. Yoshihara, Y., Nakamura, H., Obata, K., Yamada, H., Hayakawa, T.,

Fujikawa, K. and Okada, Y. 2000. Matrix metalloproteinases and tissue inhibitors of metalloproteinases in synovial fluids from patients with rheumatoid arthritis or osteoarthritis. *Annals of the Rheumatic Diseases*. **59**(6), 455 LP – 461.

204. Burrage, P.S., Mix, K.S. and Brinckerhoff, C.E. 2006. Matrix metalloproteinases: Role in arthritis. *Frontiers in Bioscience*. **11**(1 P.447-888), pp.529–543.

205. Li, H., Wang, D., Yuan, Y. and Min, J. 2017. New insights on the MMP-13 regulatory network in the pathogenesis of early osteoarthritis. *Arthritis Research & Therapy*. **19**(1), p.248.

206. Kim, K.S., Choi, H.M., Lee, Y.A., Choi, I.A., Lee, S.H., Hong, S.J., Yang, H.I. and Yoo, M.C. 2011. Expression levels and association of gelatinases MMP-2 and MMP-9 and collagenases MMP-1 and MMP-13 with VEGF in synovial fluid of patients with arthritis. *Rheumatology International*. **31**(4), pp.543–547.

207. Heard, B.J., Martin, L., Rattner, J.B., Frank, C.B., Hart, D.A. and Krawetz, R. 2012. Matrix metalloproteinase protein expression profiles cannot distinguish between normal and early osteoarthritic synovial fluid. *BMC Musculoskeletal Disorders*. **13**(1), p.1.

208. Wang, M., Sampson, E.R., Jin, H., Li, J., Ke, Q.H., Im, H.J. and Chen, D. 2013. MMP13 is a critical target gene during the progression of osteoarthritis. *Arthritis Research and Therapy*. **15**(1), pp.1–11.

209. Stevens, M.M. and George, J.H. 2005. Exploring and engineering the cell surface interface. *Science*. **310**(5751), pp.1135–1138.

210. Blache, U., Stevens, M.M. and Gentleman, E. 2020. Harnessing the secreted extracellular matrix to engineer tissues. *Nature Biomedical*

Engineering., pp.1–7.

211. Liu, M., Zeng, X., Ma, C., Yi, H., Ali, Z., Mou, X., Li, S., Deng, Y. and He, N. 2017. Injectable hydrogels for cartilage and bone tissue engineering. *Bone Research*. **5**(November 2016).

212. Clark, A.Y., Martin, K.E., García, J.R., Johnson, C.T., Theriault, H.S., Han, W.M., Zhou, D.W., Botchwey, E.A. and García, A.J. 2020. Integrin-specific hydrogels modulate transplanted human bone marrow-derived mesenchymal stem cell survival, engraftment, and reparative activities. *Nature Communications*. **11**(1), pp.1–14.

213. Slepecky, R.A. 1967. Human Synovial Fluid : Detection of a New Component. *Science*. **155**(3764), pp.839–842.

214. Kotevoglu, N., Iyibozkurt, P.C., Hiz, O., Toktas, H. and Kuran, B. 2006. A prospective randomised controlled clinical trial comparing the efficacy of different molecular weight hyaluronan solutions in the treatment of knee osteoarthritis. *Rheumatology International*. **26**(4), pp.325–330.

215. Gao, Z., Carames-mendez, P., Xia, D., Pask, C.M., Mcgowan, P.C., Bingham, P.A., Scrimshire, A., Tronci, G. and Thornton, P.D. 2020. The facile and additive-free synthesis of a cell-friendly iron(III)–glutathione complex. *Dalton Transactions*. **49**, pp. 10574-10579.

216. Huang, W., Wang, Y., Chen, Y., Zhao, Y., Zhang, Q., Zheng, X., Chen, L. and Zhang, L. 2016. Strong and Rapidly Self-Healing Hydrogels: Potential Hemostatic Materials. *Advanced Healthcare Materials*. **5**(21), pp.2813–2822.

217. Hu, X., Gao, Z., Tan, H., Wang, H., Mao, X. and Pang, J. 2019. An Injectable Hyaluronic Acid-Based Composite Hydrogel by DA Click Chemistry With pH Sensitive Nanoparticle for Biomedical Application.

Frontiers in Chemistry. **7**(July), pp.1–11.

218. Spicer, C.D. 2020. Hydrogel scaffolds for tissue engineering: The importance of polymer choice. *Polymer Chemistry*. **11**(2), pp.184–219.

219. Zhang, Y., Yu, J., Ren, K., Zuo, J., Ding, J. and Chen, X. 2019. Thermosensitive Hydrogels as Scaffolds for Cartilage Tissue Engineering. *Biomacromolecules*. **20**(4), pp.1478–1492.

220. Liu, L., Xiang, Y., Wang, Z., Yang, X., Yu, X., Lu, Y., Deng, L. and Cui, W. 2019. Adhesive liposomes loaded onto an injectable, self-healing and antibacterial hydrogel for promoting bone reconstruction. *NPG Asia Materials*. **11**(1).

221. Shi, Y., Wang, M., Ma, C., Wang, Y., Li, X. and Yu, G. 2015. A Conductive Self-Healing Hybrid Gel Enabled by Metal-Ligand Supramolecule and Nanostructured Conductive Polymer. *Nano Letters*. **15**(9), pp.6276–6281.

222. Loynachan, C.N., Soleimany, A.P., Dudani, J.S., Lin, Y., Najer, A., Bekdemir, A., Chen, Q., Bhatia, S.N. and Stevens, M.M. 2019. Renal clearable catalytic gold nanoclusters for in vivo disease monitoring. *Nature Nanotechnology*. **14**(9), pp.883–890.

223. Paquet, C., De Haan, H.W., Leek, D.M., Lin, H.Y., Xiang, B., Tian, G., Kell, A. and Simard, B. 2011. Clusters of superparamagnetic iron oxide nanoparticles encapsulated in a hydrogel: A particle architecture generating a synergistic enhancement of the T2 relaxation. *ACS Nano*. **5**(4), pp.3104–3112.

224. Yu, W., Zhu, Y., Li, H. and He, Y. 2019. An injectable quercetin-loaded hydrogel with cartilage-protection and immunomodulatory properties for articular cartilage repair. *ACS Applied Bio Materials*.

225. Liang, H., Russell, S.J., Wood, D.J. and Tronci, G. 2018. A hydroxamic

acid-methacrylated collagen conjugate for the modulation of inflammation-related MMP upregulation. *Journal of Materials Chemistry B*. **6**(22), pp.3703–3715.

226. Khalil, M.I., Al-Zahem, A.M. and Al-Qunaibit, M.H. 2013. Synthesis, characterization, mössbauer parameters, and antitumor activity of Fe(III) curcumin complex. *Bioinorganic Chemistry and Applications*. **2013**, pp.1–5.

227. Yoo, L., Gupta, V., Lee, C., Kavehpore, P. and Demer, J.L. 2011. Viscoelastic properties of bovine orbital connective tissue and fat: Constitutive models. *Biomechanics and Modeling in Mechanobiology*. **10**(6), pp.901–914.

228. Abubacker, S., McPeak, A., Dorosz, S.G., Egberts, P. and Schmidt, T.A. 2018. Effect of counterface on cartilage boundary lubricating ability by proteoglycan 4 and hyaluronan: Cartilage-glass versus cartilage–cartilage. *Journal of Orthopaedic Research*. **36**(11), pp.2923–2931.

Appendix A

Training Lists

A.1 2018-2019

Events	Date
HR Induction & Compulsory HS Information (0.5 hours)	Tue 02 Oct 2018
Increasing Visibility PGRs (2 hours)	Mon 15 Oct 2018
Foundations in Teaching (7 hours)	Fri 09 Nov 2018
Molecular Functions Based on Intermolecular Interactions (1 hours)	Thu 24 Jan 2019
Rheometer training (4 hours)	Mon 25 Feb 2019
Compounds and catalysts that mimic the roles metals play in Biology (1 hours)	Wed 17 Apr 2019
Royce Institute Biomedical Materials Event (3 hours)	Wed 24 Apr 2019
Laser confocal scanning microscopy (LCSM) training (48 hours)	Tue 07 May 2019
Scanning electron microscope Training (4 hours)	Wed 08 May 2019
Supercritical water reactor design (1 hours)	Wed 22 May 2019
Tissue Culture Training (336 hours)	Mon 03 Jun 2019
PGR conference (8 hours)	Thu 06 Jun 2019
School of Dentistry - Research Day (7 hours)	Thu 11 Jul 2019
Immune evasion strategies of porcine reproductive and respiratory syndrome virus (1 hours)	Wed 17 Jul 2019

Supramolecular processing of proteins for hierarchical mineralization. (1 hours)	Wed 16 Oct 2019

A.2 2019-2020

Events	**Date**
Virtual meeting: the Macro group UK's Young Researchers Meeting (YRM 2020) (10 hours)	Mon 29 Jun 2020
SWD1a: Introduction to Python Programming Online (Part 4 of 4) (3 hours)	Wed 10 Jun 2020
HPC1-HPC Carpentry (Online) (6.5 hours)	Mon 08 Jun 2020
SWD1a: Introduction to Python Programming Online (Part 3 of 4) (3 hours)	Wed 03 Jun 2020
SWD1a: Introduction to Python Programming Online (Part 2 of 4) (3 hours)	Wed 27 May 2020
SWD1a: Introduction to Python Programming online (Part 1 of 4) (3 hours)	Wed 20 May 2020
Systems Chemistry Virtual Symposium (20 hours)	Mon 18 May 2020
Word for Thesis Part 1D (Online) (1 hours)	Thu 07 May2020
Word for Thesis Part 1C (Online) (1 hours)	Tue 05 May 2020
Word for Thesis Part 1B (Online) (1 hours)	Fri 01 May 2020
Word for Thesis Part 1A (Online) (1.5 hours)	Wed 29 Apr 2020

Theoretical Physics Group Seminar: Better Tools to Model Proteins Complexed with Ligands (1.5 hours)	Wed 29 Apr 2020
HPC0-Introduction to Linux (Online) (3.5 hours)	Wed 22 Apr 2020
Theoretical Physics Group Seminar: Better Tools to Model Proteins Complexed with Ligands (1.5 hours)	Wed 29 Apr 2020
Word for Thesis Part 1A (Online) (1.5 hours)	Wed 29 Apr 2020
Word for Thesis Part 1B (Online course) (1 hours)	Fri 01 May 2020
Word for Thesis Part 1C (Online) (1 hours)	Tue 05 May 2020
Word for Thesis Part 1D (Online) (1 hours)	Thu 07 May 2020

Appendix B

Related publications during PhD projects

A.1 From Chapter 2

Gao, Z., Golland, B., Tronci, G. and Thornton, P.D. 2019. A redox-responsive hyaluronic acid-based hydrogel for chronic wound management. *Journal of Materials Chemistry B*. **7**(47), pp.7494–7501.

A.2 From Chapter 3

Gao, Z., Hassouneh, L., Yang, X., Pang J., Thornton, P.D. and Tronci, G. 2020. Hydrogen phosphate-mediated acellular biomineralisation within a dual crosslinked hyaluronic acid hydrogel. *European Polymer Journal*. (Accepted)

A.3 From Chapter 4

Gao, Z., Carames-mendez, P., Xia, D., Pask, C.M., Mcgowan, P.C., Bingham, P.A., Scrimshire, A., Tronci, G. and Thornton, P.D. 2020. The facile and additive-free synthesis of a cell-friendly iron(III)–glutathione complex. *Dalton Transactions*. **49**. pp. 10574-10579.

A.4 From Chapter 5

Gao, Z., Yang, X., Jones, E., Bingham, P.A., Scrimshire, A., Thornton, P.D. and Tronci, G. 2020. An injectable, self-healing and MMP-inhibiting hyaluronic acid gel via iron coordination. *International Journal of Biological Macromolecules*. **165**, pp.2022–2029.

Index

Information of calibration curves used in this project:

(1) TNBS calibration equation of cystamine:

$y=0.0666x-0.0184$, $R^2=0.9933$, y=absorbance, x= cystamine concentration, mM.

(2) TNBS calibration equation of ethylenediamine: $y=0.0658x-0.0246$, $R^2=0.9743$, y=absorbance, x=ethylenediamine concentration (mM).

(3) RITC-dextran calibration equation:

$y=0.0011x-0.004$, $R^2=0.9995$, y=absorbance, x= RITC-dextran concentration ($\mu g \cdot ml^{-1}$)